JET-R(94)08

Large Minority Ion Orbit Effects in ICRF Heating Experiments on JET

E Righi

JET Joint Undertaking, Abingdon, Oxon, OX14 3EA.

A thesis submitted in partial fulfilment of the requirements for the degree of Doctor of Philosophy and DIC

Abstract

In the present thesis the role of large orbits of high energy minority ions during Ion Cyclotron Resonance Heating (ICRF) experiments on a two-component plasma in the Joint European Torus (JET) is considered. The model presented here includes guiding centre orbits in the calculation of the minority ion distribution function and of the radial profiles of the collisional power with electrons and background ions. The results substantially differ from previous models in the estimate of the number of high energy particles and in the electron power deposition profile, which deviates considerably from the usual Gaussian shape.

The orbit model thus introduced is then applied to a number of problems. Firstly, it is shown how to calculate correctly the fusion yield in ICRF heated (^{3}He)D plasmas, and the results are compared with high fusion yield experiments carried out on JET and extrapolated to (^{3}He)D experiments on ITER. Then the problem of the saturation of the central electron temperature at high values of the RF power per particle is addressed. It is firstly shown that the orbit-induced modification of the electron power deposition profile has important consequences for the evaluation of the transport coefficients in the plasma centre. Then the temperature saturation is shown to be caused by a combination of orbit effects and degradation of plasma confinement with increasing electron temperature.

Tomographic reconstructions of γ-ray emission due to nuclear reactions of ^{3}He with ^{9}Be impurities present in the plasma show clear evidence of trapped ion orbits. These γ-ray emission profiles are simulated for both on-axis and off-axis ICRF heated (^{3}He)D plasmas by taking into account orbits of minority ions with energies above the threshold for nuclear reactions to occur and a distribution which is function of both parallel and perpendicular velocity and pitch-angle.

Acknowledgements

I have a debt of gratitude with many people, who taught me, or supported me, or simply encouraged me while working at JET.

Firstly, I thank my parents who, against their feelings, did not object too strongly on my going to England to work for my doctorate.

My JET supervisor, Dr. D.F.H. Start, led me - sometimes by hand - into the intricacies of ICRF heating and JET burocracy (sometimes worse than physics) and encouraged me in every way he could: he is more a friend than a supervisor, by now.

I thank also Prof. Malcolm G. Haines for his invaluable teachings and for having provided me with a College (a real English College!) where to present my thesis.

The RF Division, headed first by Dr. J. Jacquinot and then by Dr. C. Gormezano, provided me with an ideal environment where to "grow up", giving me responsabilities and duties that I did not think at first I could successfully carry out (I never blew up the ICRH plant, though).

The last, but not least, acknowledgement goes to my husband Chris Steele, with whom I had many late evening discussions on the technicalities of the RF plant, and to whom goes the credit for supporting my morale especially in the final stages of preparation of the thesis.

Table of Contents

Abstract 1
Acknowledgements 2
Table of Contents 3
List of Illustrations 6
List of Tables 9

1.0 Introduction 10

2.0 Ion cyclotron resonance heating in tokamaks 13
2.1 Introduction 13
2.2 Wave propagation at the ion cyclotron range of frequencies 16
2.2.1 Wave physics 16
2.2.2 ICRF Heating 20
2.2.2.1 Cyclotron damping 23
2.2.2.2 Mode conversion 30
2.2.2.3 Transit time damping 33
2.3 Fast wave current drive and sawtooth control experiments 34
2.4 The JET ICRH system 37
2.4.1 The RF generators 38
2.4.2 The RF transmission line system 39
2.4.3 The JET ICRF antennae 41
2.4.4 The pumped divertor phase upgrading 44
2.5 References 47

3.0 Modelling ICRF data on JET 50
3.1 Introduction 50
3.2 Electron temperature and density measurements 51
3.2.1 Measurement of T_e using ECE 51
3.2.2 LIDAR Thomson scattering 53

3.2.3 Laser measurement of n_e 55
3.3 The fast ion energy content 56
3.4 Direct electron heating 58
3.5 Neutral particle analysis 59
3.6 References 62

4.0 The orbit model 63
4.1 Fast wave heating of a two-component plasma 63
4.1.1 The Fokker-Planck equation 64
4.1.2 The steady-state $f(u)$ solution 67
4.1.3 The steady-state $f(u_\perp)$ solution 69
4.2 The orbit model 72
4.2.1 Guiding centre orbits 73
4.2.2 The minority ion-electron collision frequency 74
4.2.3 The collision operators 76
4.2.4 The distribution function 77
4.2.5 Collisional power transfer 79
4.2.6 The fast ion energy content 84
4.3 Summary and conclusions 86
4.4 References 86

5.0 Orbit effects on the (^{3}He)D fusion yield 87
5.1 Preparation of the experiment and results 87
5.2 Measurement of the ^{3}He-D reaction rate 91
5.3 Local reactivity and total fusion power 92
5.3.1 Zero orbit reactivity 94
5.3.2 Reactivity calculations including fast ion orbits 100
5.3.3 Comparison with the experiment 106
5.4 Applications to ITER 109
5.5 Summary and conclusions 112
5.6 References 112

6.0 Orbit effects and heat transport 114
6.1 Heat transport in JET plasmas 114
6.1.1 The heat diffusivity coefficient 117
6.2 Local transport with on/off-axis ICRF heating 119
6.3 The electron temperature saturation 123

6.3.1 Transport analysis 125
6.3.2 The T_{e0} saturation explained 129
6.4 Summary and conclusions 134
6.5 References 135

7.0 Interaction of ^{3}He ions with plasma impurities during ICRF heating 137
7.1 Introduction 137
7.2 Production of γ photons during ^{3}He-^{9}Be reactions 138
7.3 Simulation of γ-ray emission 146
7.4 Summary and conclusions 154
7.5 References 156

8.0 Summary and conclusions 158

Appendix A Legenda 161

Appendix B Scaling law for optimum fusion yield 163

Appendix C The role of the pitch-angle in the calculation of the heating profiles 165

List of Illustrations

Figure 2.1 Cartesian frame of reference 17
Figure 2.2 Toroidal eigenmodes of the fast wave 20
Figure 2.3 Electron and ion heating ratios 21
Figure 2.4 Summary of the different ways in which the fast wave can be a absorbed 22
Figure 2.5 a) Cross-section of a tokamak plasma
b) Intuitive physical picture of cyclotron harmonic acceleration 24
Figure 2.6 Geometry of the two-ion hybrid resonance/cut-off pair 25
Figure 2.7 Polarization of the fast wave electric field 25
Figure 2.8 RF coupled power for one generator of the JET ICRH plant 27
Figure 2.9 γ radiation measurements show the existence of high energy minority ions 28
Figure 2.10 An example of high electron temperature regime in JET 30
Figure 2.11 Effect of directed fast wave on sawtooth stability 35
Figure 2.12 Sawtooth behaviour at $\phi=\pi/2$ and different RF power levels 35
Figure 2.13 Block diagram of the JET ICRH transmission line system 40
Figure 2.14 Central conductor of the A_1 antenna 42
Figure 2.15 Position of the eight A_1 antennae in the vacuum vessel 42
Figure 2.16 Parallel wavevector spectra 44
Figure 2.17 The new A_2 antenna 46
Figure 2.18 Position of the new A_2 antennae in the vacuum vessel 46

Figure 3.1 Electron temperature profiles 52
Figure 3.2 Electron density profiles 55
Figure 3.3 Fast ion energy 57
Figure 3.4 Measurement of direct electron heating 58
Figure 3.5 Direct electron heating profile 59
Figure 3.6 Neutral particle analyser 60
Figure 3.7 Details of the time-of-flight detector 61

Figure 4.1 Stix distribution functions 69
Figure 4.2 Guiding centre orbits 75
Figure 4.3 Minority distribution function 78
Figure 4.4 Power deposition profiles 81
Figure 4.5 Fast ion energy 83
Figure 4.6 Sensitivity test 84

Figure 5.1 Magnetic configuration of the high fusion yield experiment 89
Figure 5.2 γ spectrum measured during high power ^{3}He minority heating 90
Figure 5.3 Experimental arrangement of the γ detectors in JET 92
Figure 5.4 Plot of the ^{3}He-D reaction rate 93
Figure 5.5 Comparison between the isotropic and anisotropic distribution functions 96
Figure 5.6 Fusion yield calculated with isotropic and anisotropic distributions 98
Figure 5.7 Comparison between zero-orbit and orbit fusion yields 99
Figure 5.8 Comparison between orbit and zero-orbit anisotropic distributions 100
Figure 5.9 Local reactivity 101
Figure 5.10 Effects of geometry on the local reactivity 103
Figure 5.11 Orbit and zero-orbit anisotropic distributions at $\eta = 0.03$ 104
Figure 5.12 Fusion rate for simulation B at η=0.11,0.03 105
Figure 5.13 Experimental and numerical fusion yield 106
Figure 5.14 Time evolution of the main plasma parameters for discharges 23399 and 23438 107
Figure 5.15 Comparison between the results of the simulations and the experiment 109
Figure 5.15 Summary of fusion yield simulations for ITER 111

Figure 6.1 JET transport experiments 115
Figure 6.2 Heat flux vs. $-n\nabla T_e$ for the JET transport experiments 116
Figure 6.3 Experimental curves for on/off-axis ICRF discharges 24665 and 25651 120
Figure 6.4 Zero-orbit effective heat diffusivity 121
Figure 6.5 Effective heat diffusivity for the on-axis discharge 24665 122
Figure 6.6 The T_{e0} saturation 124
Figure 6.7 A sample of the data of Fig.6.6 124

Figure 6.8 Fast ion energy 125
Figure 6.9 Effective heat diffusivity profiles 126
Figure 6.10 Effective heat diffusivity profiles for the discharges of group d 126
Figure 6.11 Average heat diffusivity 127
Figure 6.12 T_{e0} calculated with a T_e-independent heat diffusivity 130
Figure 6.13 Orbit and zero-orbit (Stix) T_{e0} 130
Figure 6.14 Linear increase of χ_{eff} with T_e and max$|\nabla T_e|$ 131
Figure 6.15 Extrapolation of T_{e0} to high RF power per particle 133

Figure 7.1 ^{11}B excitation curves at 90° 139
Figure 7.2 Time evolution of the main plasma parameters 141
Figure 7.3 False colour tomographies of γ emission
a) JPN 23453 on-axis ICRF 143
b) JPN 23450 off-axis ICRF 144
Figure 7.4 3D tomographic inversion of γ emissivity for JPN 23450 145
Figure 7.5 "Total" differential cross-section for ^{11}B 146
Figure 7.6 Minority ion distribution function in $(v_{\|},v_{\perp})$ space 147
Figure 7.7 Weight functions for the values of the pitch-angle θ on the distribution ridge 149
Figure 7.8 False colour image of the simulation of γ emissivity for
a) JPN 23453 151
b) JPN 23450 152
Figure 7.9 3D numerical reconstruction of γ emissivity for JPN 23450 153
Figure 7.10 Comparison between calculated and measured γ intensity at the radius correspondent to the peak emissivity 154

Figure C.1 Electron heating profiles calculated with and without pitch-angle dependence 165

List of Tables

Table 2.1 Nominal characteristics of the JET ICRH plant 37
Table 2.2 JET RF generator design specification 1990 39

Table 5.1 Parameters for (^{3}He)D simulations 98
Table 5.2 Plasma parameters and numerical results 108
Table 5.3 ITER EDA and CDA - Main parameters 110
Table 5.4 Parameters for ITER scenarios 110
Table 5.5 Results of simulations 111

Table 6.1 Plasma parameters 121

Table 7.1 Main properties of ^{11}B excited states 140
Table 7.2 Main plasma parameters 145

1.0 Introduction and Thesis Outline

In recent years Ion Cyclotron Resonance Frequency (ICRF) heating has been established as one of the most successfull and reliable ways of auxiliary heating in tokamak plasmas. On the Joint European Torus (JET) tokamak alone powers in excess of 22 MW have been coupled to a deuterium plasma with hydrogen minority in single null X-point configuration [1.1].

Such high coupled power implies that resonant minority ions can have tail temperatures of order of a few MeV and, consequently, that orbit radii can be a significant fraction of the radius of the discharge. Under these circumstances spatial corrections for orbits of particles trapped in the toroidal magnetic field B_ϕ become significant when the orbit width is comparable with the width Δ_{RF} of the RF power profile, that is when the Stix tail temperature T_t [1.2] reaches a critical value, given by, [1.3],

$$T_{crit} \cong (\Delta_{RF} Z B_\phi / q)^2 e\varepsilon / 2M \ ,$$

where Ze and M are the charge and mass of the minority ion, respectively, while q is the safety factor and ε the inverse aspect ratio.

In the present thesis finite size of minority ion orbits is included in the calculation of quantities relevant to ICRF heating. In the first two Chapters ICRF heating in tokamaks and data acquisition and analysis on JET are reviewed (Chapter 2 and Chapter 3, respectively), while a list of commonly used symbols is reported in Appendix A for reference. In Chapter 4 the orbit model is presented. The first part of Chapter 4 is devoted to a brief review of a model introduced by Stix [1.2] to calculate in the zero-orbit width limit the power transferred to electrons and background ions through collisions with the minority ions (Section 4.1). The second part of the Chapter is devoted to the orbit model itself, as developed by the author (Section 4.2). Here the chanches in collisionality encountered by the resonat ions while travelling along its orbit are taken into account by averaging the minority ion-electron colision frequency

over one closed orbit, the collision and RF diffusion operators are re-deduced and a solution of the steady-state pitch-angle averaged Fokker-Planck equation is obtained. The result is applied to calculate the collisional power transfer to electrons and background ions and the perpendicular energy of the (fast) minority ions.

The remaining Chapters contain important applications of the orbit model. Thus in Chapter 5 the fusion yield produced in high power (^{3}He)D ICRF heating discharges is calculated, and the results are compared with the experiment. In this instance at the energies correspondent to the peak of the reaction rate (~800 keV) pitch-angle scattering is important and, in order to include this contribution in the calculation, it is necessary to use a distribution different from that introduced in Chapter 4 and dependent on both energy and an effective pitch-angle. Such distribution function is however made orbit-dependent following the same procedure outlined in Chapter 4. In Appendix B the scaling of the optimum fusion yield with the experimental parameters is reported. In Appendix C instead it is shown that, as far as the electron and ion power deposition profiles are concerned, the two distributions give the same results.

Chapter 6 is devoted to the solution of an intriguing problem, namely why during high power on-axis ICRF heating experiments the central electron temperature saturates at high values of the RF coupled power per particle. After a brief introduction to heat transport experiments carried out on JET, it is shown that orbit effects contribute to modify substantially the values that the effective heat diffusivity assumes in the plasma centre, and that the temperature saturation is caused by a combination of orbit effects and degradation of confinement due to the increase of the electron temperature itself (through auxiliary heating).

The last application of finite orbit effects during ICRF heating on JET considered in this thesis is presented in Chapter 7. Contour plots of γ emission on the poloidal plane, expressed as false colour images, bear the unmistakable shape of trapped orbits of minority ions during on-axis and off-axis heating in a (^{3}He)D plasma. The measured γ photons used to produce the tomographies come from nuclear reactions of resonant ^{3}He ions with ^{9}Be impurities present in the plasma. It is here shown that such tomographies can be reproduced by considering the distribution in minor radius, velocity and pitch-angle of the minority ions (derived from the numerical solution of the bounce-averaged Fokker-Planck equation [1.4]) and information on the γ production from ^{3}He-^{9}Be nuclear reactions.

Lastly, in Chapter 8 conclusions are drawn.

1.1 References

1. J. Jacquinot et *al.*, Proc. 18th EPS Conference on Controlled Fusion and Plasma Physics, Berlin (Germany), 1991.

2. T.H. Stix, Nucl. Fusion **15** (1975), 737.

3. G.A. Cottrell and D.F.H. Start, Nucl. Fusion **31** (1991), 61.

4. M.R. O'Brien, M. Cox and D.F.H. Start, Nucl. Fusion **26** (1986), 1625.

2.0 Ion Cyclotron Resonance Heating in Tokamaks

In the present Chapter the interaction of the fast wave with the plasma is considered, from both the physical and the technological points of view. Thus in the Introduction the main schemes of plasma heating using RF waves are outlined. The physics of the fast wave-plasma interaction is then discussed, and Ion Cyclotron Resonance Heating (ICRH) is introduced. Special emphasis is given to minority ICRH, the relevant RF heating mechanism on JET (Section 2.2). Section 2.3 is devoted to a brief introduction to fast wave current drive and sawtooth control experiments in JET. Section 2.4, lastly, summarizes the main technological features of the JET ICRH plant.

2.1 Introduction

In tokamaks a plasma current I_p in the toroidal direction is produced by varying the magnetic flux linking the torus. An additional magnetic field in the poloidal direction is consequently created, which is about ten times smaller than the main toroidal field B_ϕ produced by a set of external coils surrounding the vacuum vessel. The resulting magnetic lines are helical and lie on nested magnetic flux surfaces. In general a given magnetic surface is ergodically covered by the magnetic field line. However flux surfaces exist on which the field lines form a closed loop after a finite number of toroidal circuits. MHD instabilities, driven by current and pressure gradients, have peaked eigenvalues at these so called *rational* flux surfaces [2.01]. As a consequence a limit exists to the values that the poloidal magnetic field and hence the plasma current can assume. In fact in order to avoid the most dangerous instabilities the safety factor $q(r) = rB_\phi(r) / R_0 B_\theta(r)$ at the plasma boundary must satisfy the following condition [2.01,2.02],

$$q(a_0) = \frac{a_0 B_\phi(a_0)}{R_0 B_\theta(a_0)} > 2.5. \qquad (2.1)$$

As a consequence Eq.(2.1) sets an upper limit to the ohmic power that can be dissipated to heat the plasma. Secondly, since the plasma resistivity decreases with electron temperature like $T_e^{-3/2}$, ohmic heating becomes less and less effective as the temperature increases. Thus if the plasma temperature must be raised to thermonuclear values other forms of heating are needed.

Two main types of auxiliary heating are used, namely Neutral Beam Injection (NBI) and Radio Frequency (RF) heating. The former uses beams of high energy neutral atoms which, once injected in the plasma, are rapidly ionized and share their energy through collisions. However there are difficulties in heating the plasma centre using NBI, since the absorption of the beam energy in the edge plasma region is in general considerable. For instance, to reach the centre of ITER the beam energy required will be greater than 1MeV (for comparison, the beam energy during present-day NBI heated experiments on JET can reach 140-180 keV).

RF heating, on the other hand, can be very effective because under proper conditions the launched wave can propagate as far as the plasma centre and be absorbed there.

Four main RF heating schemes can be defined, according to the frequency range of the wave;

1. the *Alfven wave* scheme [2.02,2.03], at a frequency of a few MHz, involves the generation of the compressional (fast) Alfven wave with an antenna located at the plasma edge, the current of which is parallel to the magnetic field. The fast wave will eventually mode convert into the shear (slow) Alfven wave at a magnetic surface known as the *Alfven resonance surface* [2.02]. Here both waves have locally the same wavelength and propagate parallel to the magnetic field. With this scheme, electrons near the Alfven resonance are heated through Electron Landau Damping (ELD) of the slow wave.

2. The *Ion Cyclotron Resonance Frequency (ICRF)* scheme [2.02,2.03] makes use of the fast wave at a frequency near the ion cyclotron frequency at a few tens of MHz. The wave is usually excited from the low magnetic field side of the tokamak near the plasma edge, with the antenna current perpendicular to the magnetic field. With this antenna configuration three heating schemes can be used, depending on the physical properties of the plasma-wave interaction;

- cyclotron damping, which includes second harmonic heating of a one ion species plasma and minority heating of a two ion species plasma;
- mode conversion heating;
- a combination of Transit Time Magnetic Pumping (TTMP) and ELD.

The first scheme exploits themal effects on the damping of the fast wave at the second harmonic of the cylotron frequency of the background ions, and damping of the fast wave at the cold ion-ion hybrid resonance layer of a two-component plasma. Electrons are heated instead of ions when mode conversion, TTMP and ELD occur. Usually all the processes listed above are present during ICRF heating experiments, with different relative importance depending on the plasma parameters.

3. The *Lower Hybrid Resonance Frequency (LHRF)* scheme [2.03] involves waves at a frequency comparable with the lower hybrid frequency at the plasma centre (a few GHz). The cold plasma resonance however does not play any significant role in the absorption, and damping relies mainly on ELD. In the regime where this occurs a long tail on the parallel velocity distribution function is produced which can carry a substantial current. This is the reason why LHRF is in general used for current drive experiments rather than for heating.

4. The *Electron Cyclotron Resonance Frequency (ECRF)* scheme [2.03], lastly, uses electron cyclotron waves at frequencies in the range 30-150 GHz. Its use as a heating system in large tokamaks has been hindranced by the technological difficulty of manifacturing high power sources at the necessary frequencies. It is only recently that gyratrons, which extract energy from a beam of relativistic electrons in a strong magnetic field, have become fairly reliable sources of high RF power. Another possible source now available is the Free Electron Laser (FEL), which produces electromagnetic waves with frequencies above 100 GHz.

2.2 Wave propagation at the Ion Cyclotron Range of Frequencies

In the first part of this Section the properties of wave propagation in the Ion Cyclotron Range of frequencies are considered. The dielectric tensor and the dispersion relation for an electromagnetic wave propagating at an angle in a plasma in thermal equilibrium are introduced. The fast wave characteristics far from the resonance are then briefly described using the cold plasma approximation. When the wave frequency ω is close to a harmonic of the ion cyclotron frequency thermal corrections are instead taken into account.

In the second part plasma heating through the fast wave is introduced, and the main heating mechanisms (minority cyclotron damping, mode conversion and TTMP) are discussed.

Since only ion motion is relevant in what follows, relativistic corrections are not taken into account. For the symbols and conventions used, the reader is referred to the Legenda (Appendix A).

2.2.1 Wave Physics

Consider a cartesian frame of reference with the z axis parallel to the direction of the external magnetic field **B** as in Fig.2.1: if the wavevector is chosen in the *(x,z)* plane, the plasma dispersion relation reads [2.03,2.04,2.05],

$$\begin{vmatrix} \varepsilon_{11} - n_{\parallel}^2 & \varepsilon_{12} & n_{\parallel} n_{\perp} \\ \varepsilon_{21} & \varepsilon_{22} - (n_{\parallel}^2 + n_{\perp}^2) & 0 \\ n_{\perp} n_{\parallel} & 0 & \varepsilon_{33} - n_{\perp}^2 \end{vmatrix} = 0. \qquad (2.2)$$

If the plasma is in thermal equilibrium, or if at least the distribution functions of the individual species are Maxwellian, the elements of the dielectric tensor ε_{ij} have the following expression [2.03,2.04,2.05],

$$\varepsilon_{ij} = \delta_{ij} + \sum_{\alpha} \frac{\omega_{p\alpha}^2}{\omega} \left(\frac{m_{\alpha}}{2 k_B T_{\alpha}} \right)^{1/2} \frac{e^{-\lambda_{\alpha}}}{k_{\parallel}} \sum_{n=+\infty}^{-\infty} T_{ij} \ , \qquad (2.3)$$

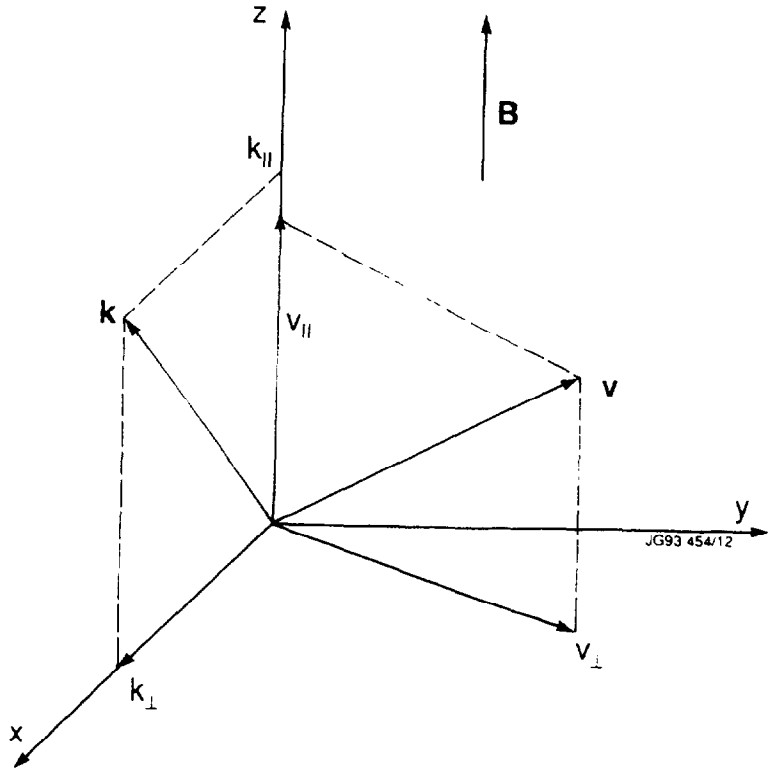

Figure 2.1 Cartesian frame of reference, with the external magnetic field **B** defining the direction of the z axis. The parallel and perpendicular components of velocity and wavenumber are also indicated.

where $\delta_{ij} = 1$ if $i=j$ and zero otherwise, while,

$$T_{ij} = \begin{pmatrix} n^2 I_n Z_n / \lambda_\alpha & in(I_n' - I_n)Z_n & nI_n Z_n' / (2\lambda_\alpha)^{1/2} \\ in(I_n' - I_n)Z_n & (n^2 I_n / \lambda_\alpha + 2\lambda_\alpha I_n - 2\lambda_\alpha I_n')Z_n & \lambda_\alpha^{1/2}(I_n' - I_n)Z_n' / \sqrt{2} \\ nI_n Z_n' / (2\lambda_\alpha)^{1/2} & \lambda_\alpha^{1/2}(I_n' - I_n)Z_n' / \sqrt{2} & I_n Z_n \end{pmatrix} . \quad (2.4)$$

In Eq.(2.4) the modified Bessel function I_n and its derivative have argument $\lambda_\alpha = k_B T_\alpha k_\perp^2 / (m_\alpha \Omega_\alpha^2)$, while Z_n is the plasma dispersion function with argument,

$$\varsigma_n = (\omega - n\Omega_\alpha)\left(\frac{m_\alpha}{2k_B T_\alpha k_\parallel}\right).$$

Far from the harmonics of the ion cyclotron frequency the cold plasma approximation holds, and the dielectric tensor can be considerably simplified [2.03,2.04,2.05],

$$\varepsilon_{xx} = \varepsilon_{yy} = 1 - \sum_{\alpha} \frac{\omega_{p\alpha}^2}{\omega^2 - \Omega_{\alpha}^2} = \varepsilon_{\perp} ,$$

$$\varepsilon_{zz} = 1 - \sum_{\alpha} \frac{\omega_{p\alpha}^2}{\omega^2} = \varepsilon_{\parallel} ,$$

$$\varepsilon_{xy} = -\varepsilon_{yx} = -\sum_{\alpha} \frac{\omega_{p\alpha}^2 \Omega_{\alpha}}{\omega(\omega^2 \Omega_{\alpha}^2)} .$$

The plasma dispersion relation then reads [2.03],

$$a n_{\perp}^4 - b n_{\perp}^2 + c = 0 , \tag{2.5}$$

where,

$$a = \varepsilon_{\perp}, \quad b = (\varepsilon_{\perp} + \varepsilon_{\parallel})(\varepsilon_{\perp} - n_{\parallel}^2) - \varepsilon_{xy}^2, \quad c = \left[(\varepsilon_{\perp} - n_{\parallel}^2)^2 - \varepsilon_{xy}^2\right] .$$

The resonances are readily found taking the limit $\varepsilon_{\perp} \to 0$: in the cold plasma approximation, they are the well known upper and lower hybrid resonances. The upper hybrid frequency is above the range of frequencies considered here, while in the tokamak geometry the lower hybrid frequency is near the ion cyclotron frequency only at the plasma edge, so that it cannot be used to heat the centre.

Making the assumption that the electrons can effectively short out any electric field in the direction parallel to the magnetic field, so that the wave electric field component E_z in that direction is zero (this can be achieved for instance by using a Faraday screen, see Section 2.4), Eq.(2.5) simplifies and the following solution is obtained [2.03],

$$n_{\perp}^2 \cong [(\varepsilon_{\perp} - n_{\parallel}^2)^2 - \varepsilon_{xy}^2] / (\varepsilon_{\perp} - n_{\parallel}^2) , \tag{2.6}$$

corresponding to the fast (or compressional) Alfven wave. The propagation of this wave involves compression of the plasma transverse to the magnetic field. For the parameters appropriate to ICRH the Alfven resonance $n_{\parallel}^2 = \varepsilon_{\perp}$ is of no concern, since it is not in the plasma centre [2.03]. The dispersion relation given by Eq.(2.6) has a density cut-off correspondent to $n_{\parallel}^2 \cong \varepsilon_{\perp} + \varepsilon_{xy}$, which sets a lower limit to the values

that the plasma density can assume. The most important consequence of this is that the fast wave is evanescent near the antenna, which therefore must be within centimeters from the density cut-off in order to obtain efficient coupling [2.06]. The second solution of the dispersion relation [2.03],

$$n_{\perp}^2 \cong \varepsilon_{\parallel}(\varepsilon_{\perp} - n_{\parallel}^2)/\varepsilon_{\perp} \cong -\omega_{pe}^2/\omega^2 , \qquad (2.7)$$

is the slow (or shear) Alfven wave, highly evanescent in the high density regions. The slow wave is strongly absorbed at the ion cyclotron frequency, where it becomes the ion cyclotron wave. Also, it propagates with group velocity equal to the Alfven velocity $v_A = B/\sqrt{\mu_0 \rho}$, where $\rho = m_i n_i + m_e n_e$ is the plasma density, *parallel* to the magnetic field lines. Hence the slow wave cannot propagate through the magnetic field lines and in a tokamak plasma it is confined on the surface, thus heating only the plasma edge.

In the cold plasma approximation if only one plasma species is present there are no more resonances in the ion cyclotron range of frequencies apart from the upper and lower hybrid ones. At the ion cyclotron frequency in fact the left-handed circularly polarized component E_+ of the wave electric field, which interacts strongly with the ions, is vanishingly small [2.02,2.03,2.07]. Thus in a cold plasma the wave field at $\omega \cong \Omega_i$ is right-handed circularly polarized, and it rotates in the same direction as the electrons [2.03,2.07]. This means that any attempt to set up a wave field rotating together with the ions is immediately stopped by the system reaction [2.03]. Absorption occurs at a harmonic of the ion cyclotron frequency and is exclusively a warm plasma effect.

When $\omega \cong l\Omega_i$ thermal corrections need to be included in the dielectric tensor elements, and interesting conclusions may be drawn. By expanding Eq.(2.3) in power series of λ_α in fact it can be shown that when l=1 lower order corrections cancel out, so that the termal effects are only of order of λ_i^2. As a consequence, absorption at the fundamental is weak and it is not an effective means to heat the plasma. On the contrary when l=2 thermal corrections are of order λ_i , and the wave is consequently absorbed [2.03].

Finally, it is interesting to note that plasma conditions may be such that no resonance is inside the plasma. As a consequence the fast wave is weakly damped, and is reflected many times by the walls of the vacuum vessel, which acts as a resonant cavity [2.07,2.08]. If the wave phase shift in the plasma is sufficiently large to allow

for contructive interference, then *toroidal eigenmodes* [2.08] are created. This is achieved when the following condition [2.09] is satisfied,

$$na_0^2 > \frac{\pi B^2}{4\pi m_i \omega_{RF}^2}, \tag{2.8}$$

where n is the toroidal eigennumber and ω_{RF} is the RF (angular) frequency applied. Experimental evidence for the existence of eigenmodes is shown in Fig.2.2.

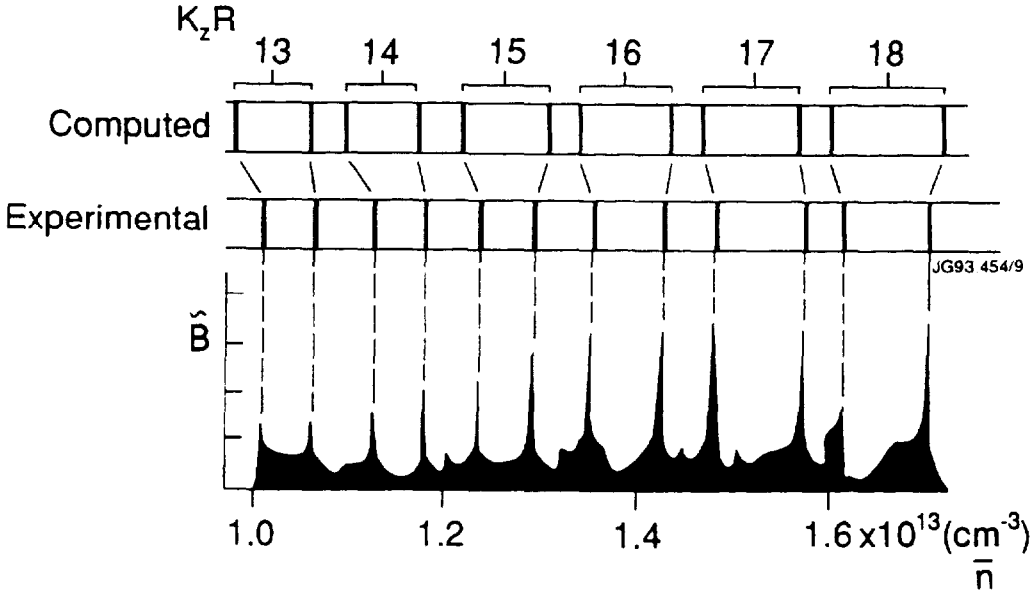

Figure 2.2 Toroidal eigenmodes of the fast wave measured in the tokamak TFR are compared with the theoretical values for the m=1 mode [2.08].

2.2.2 ICRF Heating

ICRF heating involves propagation and damping of the fast wave. For a typical JET hydrogen plasma with ion density $n_i \cong 3\times10^{19}$ m^{-3} the fast wave propagates with Alfven speed equal to v_A=c/26 and a wavelength of λ=25 cm. It is interesting to notice that this wave is refracted by density gradients, so that when tokamak geometry is considered, it is focussed along the radial direction and towards the central region of the plasma [2.03].

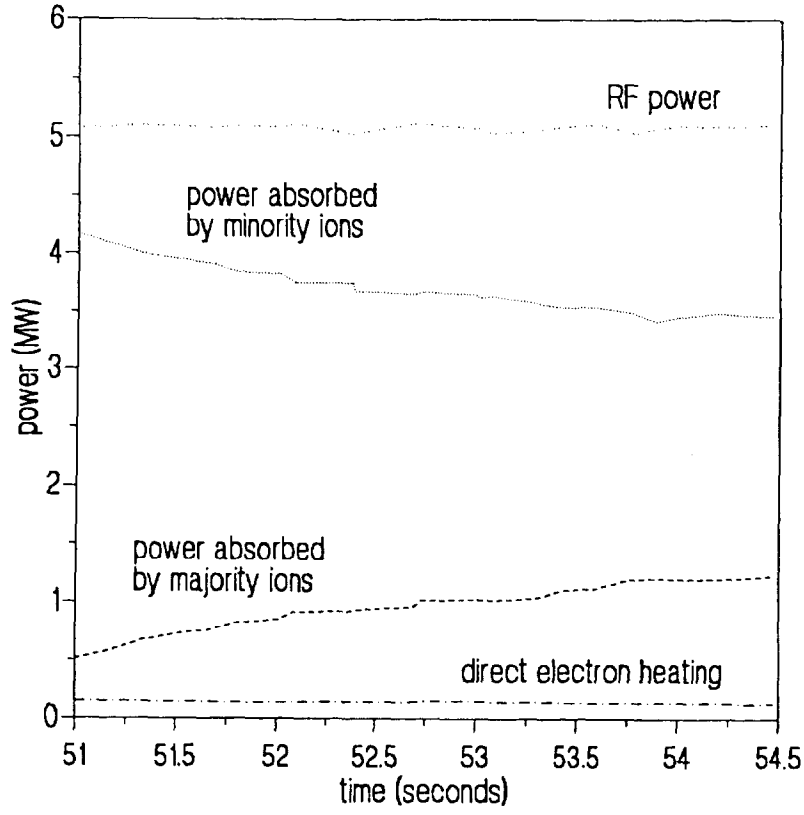

Figure 2.3 **Electron and ion heating rates.** The fast wave is usually absorbed through minority damping (dotted curve), second harmonic damping (dashed curve) and direct electron heating (sum of mode conversion, TTMP and ELD, dot-dashed curve). The time traces shown in the picture have been calculated using the Fokker-Planck code PION-T [2.10] for a JET discharge.

In ICRF heating scenarios there are essentially three ways in which the fast wave can be absorbed, depending on the plasma parameters: cyclotron damping (second harmonic damping and minority damping), mode conversion and a combination of Landau damping and transit time damping, the latter leading to Transit Time Magnetic Pumping (TTMP). Usually in an RF heating experiment these mechanisms are all more or less present. An example of this is shown in Fig.2.3, where the time traces for direct electron heating (sum of mode conversion, TTMP and ELD) and cyclotron heating (minority damping and second harmonic damping) are reported for a JET pulse [2.10]. The power transferred to electrons and ions by collision with the minority ions is also shown.

Cyclotron heating essentially relies on damping of the fast wave at a frequency near the ion cyclotron frequency. However the absorption mechanism is different depending whether in the plasma there are one or two ion species. In the former case it has been shown from a mathematical point of view (see Section 2.2.1) that damping is

possible only at the second harmonic of Ω_i (second harmonic damping). Minority cyclotron damping is instead a mechanism effective when in the plasma two ion species are present, one of which is a few percent of the other (see later), and involves collisional power transfer from the resonant minority ions to electron and background ions. Electron heating through minority ICRF is the main heating process on JET, although it has been recently shown [2.11] that it is possible to obtain substantial heating of the background ions by raising sufficiently both the minority concentration and the electron density. However a limit to the minority ion density relative to the majority ion density exists above which mode conversion of the fast wave into the electrostatic Bernstein mode is no longer negligible. When this occurs, the power is absorbed by ELD and damping of the Bernstein wave which propagates, both along and across the magnetic field, towards the cyclotron layer of one of the ion species [2.03].

On the other hand transit time damping is a mechanism which occurs when the fast wave interacts with the electrons via a force proportional to the parallel gradient of the parallel magnetic field, and it can be considered the magnetic analogue of Landau damping [2.04].

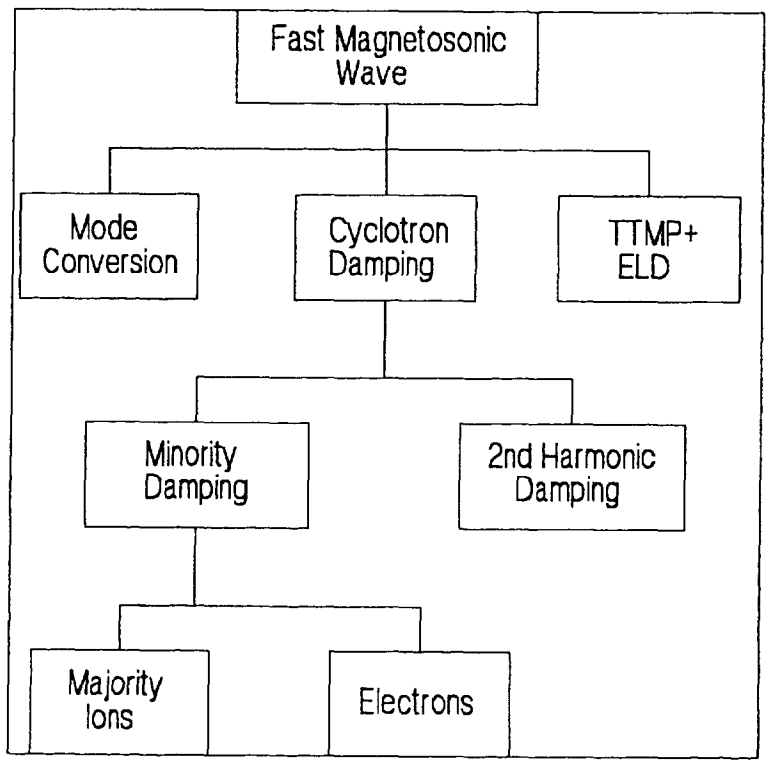

Figure 2.4 Summary of the different ways in which the fast wave can be absorbed.

The ICRF heating processes discussed which make use of the damping of the fast wave are summarized in Fig.2.4. In the following three sub-sections cyclotron damping, mode conversion and transit time damping are qualitatively analyzed.

2.2.2.1 Cyclotron Damping

In this Section the absorption processes near the ion cyclotron frequency or one of its harmonics are discussed from a physical point of view. Particular importance is given to the physical mechanisms which modify the absorption layer and the polarization of the fast wave. Thus in the first part cyclotron damping at the second harmonic in a one species plasma is introduced, and its disadvantages are briefly discussed. In the second part a second (minority) ion species and the ion-ion hybrid frequency are introduced, with all the consequences to absorption that follow.

Second Harmonic Damping

In Section 2.2.1 the fast wave damping at $\omega \cong 2\Omega_i$ has been shown to be a warm plasma effect. The same process can be described more intuitively by considering the wave polarization [2.07]. The fast wave has in fact a predominantly right-handed polarization [2.03,2.04,2.07]. In a warm plasma however the left-handed polarized component E_+, although small, is not negligible and causes wave damping [2.03]. In this case the resonant layer thickness is given approximately by $\Delta R \propto 2R_0 v_{thi} k_\parallel / \omega$ [2.07]. Now take for definitiveness a deuterium atom and consider the fast wave at a frequency equal to the second harmonic of the deuterium cyclotron frequency Ω_D. Each time that the D^+ ion crosses the resonance in its motion along the magnetic field lines it receives a kick in its perpendicular energy. It can be shown [2.12] that between passages the ion loses phase coherence between its motion and the wave electric field due to collisions, so that the quasi-linear theory [2.13] holds.

On the other hand, since the wave field varies twice as fast as the cyclotron period, the D^+ ion will experience acceleration during the first half of its Larmor cycle, deceleration during its second half, as shown in Fig.2.5. If the wave field is homogeneous, there is no net energy gain. However in an inhomogeneous wave field (i.e. $k_\perp \neq 0$) the acceleration and deceleration processes are in general unequal. Taking a statistical average over the particles random-phased with respect to the wave field, a net energy gain results. Thus damping depends on the ion Larmor radius and on the gradient of E_+, the latter being in general not so high as to provide a very strong

absorption [2.07]. It is thus clear that in present-day tokamaks second harmonic damping is a weak heating mechanism, unless strong E_+ gradients can be provided.

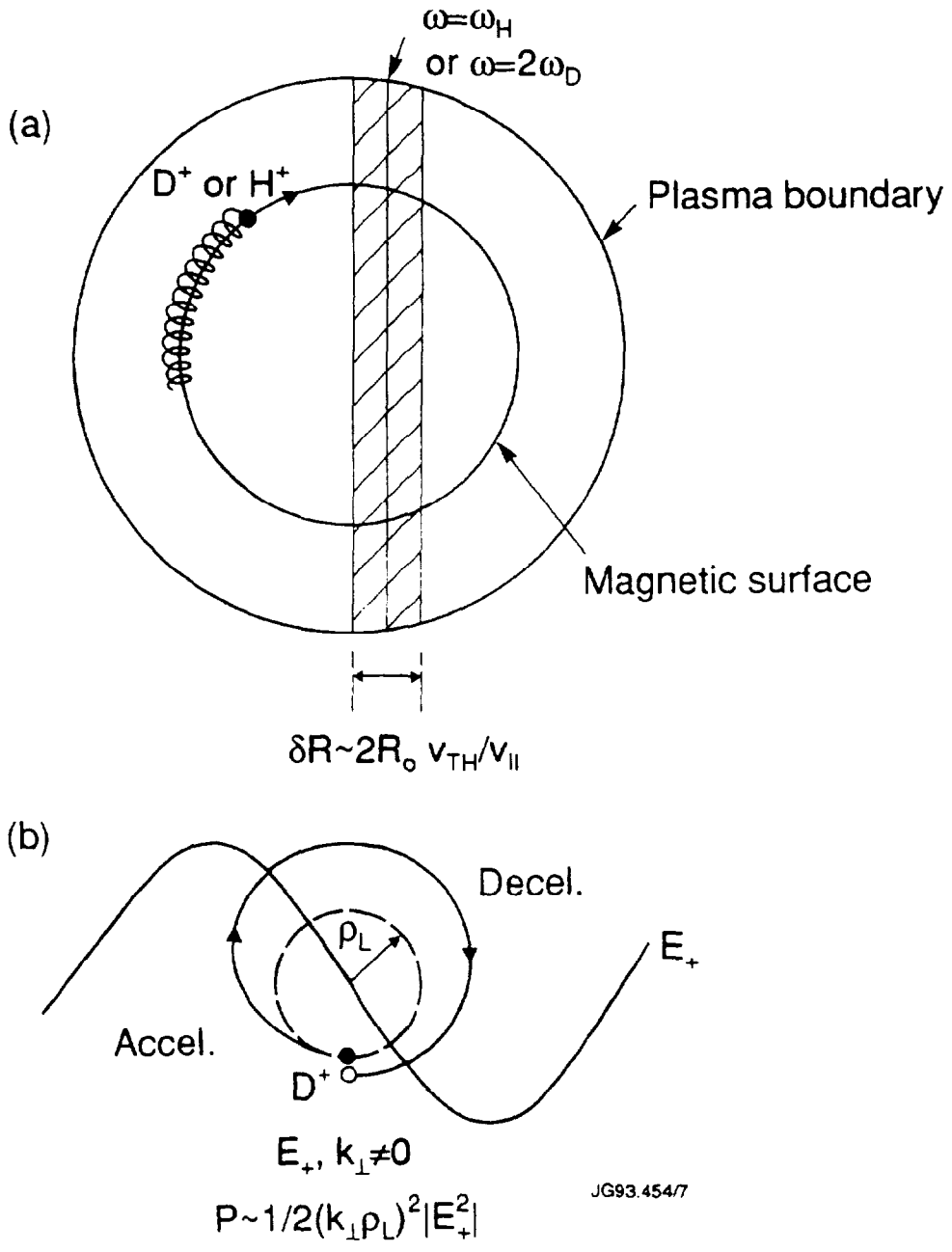

Figure 2.5 **(a) Cross-section of a tokamak plasma.** The resonant surface is roughly cylindrical with constant major radius. The absorption layer has finite thickness due to thermal effects. **(b) Intuitive physical picture of cyclotron harmonic acceleration.** In the case of the D^+ ion the wave varies twice as fast as the ion Larmor motion, so that it is accelerated and then decelerated once during one Larmor period. The ion gains energy when the wave electric field is inhomogeneous [2.07].

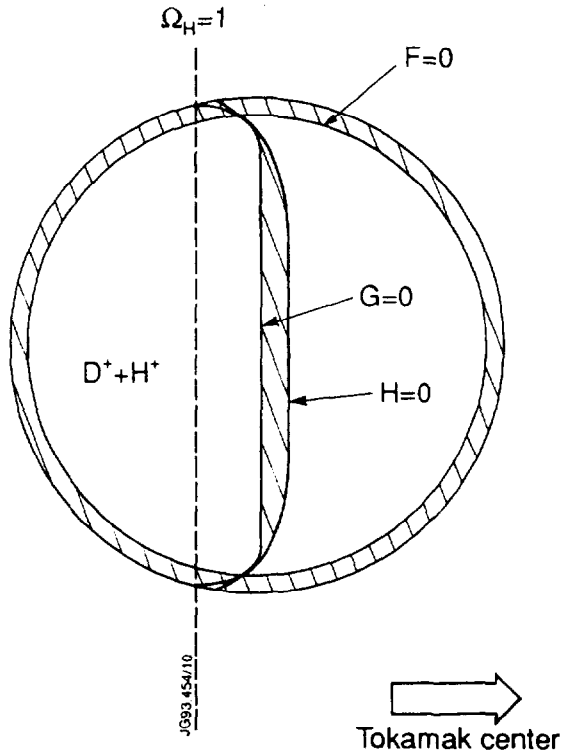

Figure 2.6 **Geometry of the ion-ion hybrid resonance/cut-off pair** in the case of a (H)D plasma with H concentration equal to 10% of the D density. The tokamak centre is on right of the picture, so that the RF antennae are on the left (low field side). The evanescent regions near the central cut-off and at the plasma edge are indicated by the shaded areas [2.07].

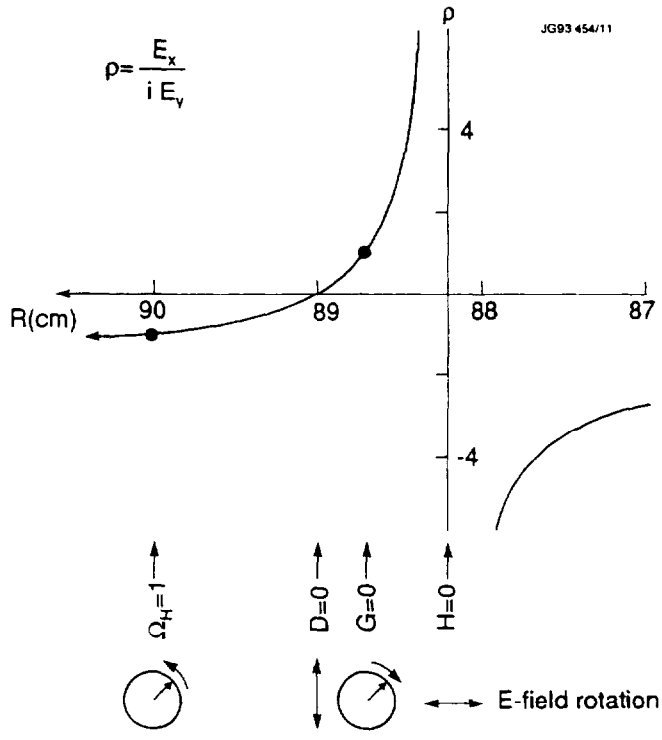

Figure 2.7 **Polarization of the fast wave electric field** $\rho=E_x/iE_y$ near the ion-ion hybrid resonance. Rotation of the electric field at the critical points is also indicated [2.07].

Minority Cyclotron Damping

When a two ion species is considered, one of which is only a few percent of the other, another cold plasma resonance appears, namely the *ion-ion hybrid resonance*, with frequency between the two ion cyclotron frequencies (see Fig.2.6). The ion-ion hybrid resonance is used to good effect to obtain strong damping at the fundamental of the minority species. The main effect of its presence is to increase the E_+ component close to the cyclotron resonance of the minority. A picture of the ratio $\rho = E_x / iE_y$ when the ion-ion hybrid resonance is present is shown schematically in Fig.2.7. In the case of H minority this results in a good enhancement of E_+, while for the ^{3}He case the values that E_+ can assume are smaller (resulting in weaker damping). A broader absorption layer can also be obtained when $k_\parallel \neq 0$, because Doppler broadening shifts the resonance from (say) Ω_{II} to $\Omega_{II} + k_\parallel v_\parallel$.

The intuitive physical picture used above to explain second harmonic damping can be adapted to show why minority damping can be so effective. For definitiveness take a hydrogen ion H^+ in the same wave field as before at $\omega \cong 2\Omega_D$: the wave frequency is also equal to the fundamental of hydrogen cyclotron frequency Ω_H, so that a proton, unlike the D^+ ion, keeps accelerating in the familiar spiraling motion [2.07]. If there are too many protons the wave electric field tends to be shielded out and the damping is consequently weak. However, if there are only a few percent of protons in a D plasma they interact very effectively with the wave and the resulting damping can be much stronger than second harmonic D damping. Thus in the case of a (H)D plasma we have both second harmonic heating of the background ions (through thermal effects) and fundamental heating of the minority, the latter being in general much more effective than the former.

First discovered by Buchsbaum [2.14], in a tokamak plasma the ion-ion hybrid resonance falls in the class of wave propagation problems in inhomogeneous plasmas where the cut-off and the resonance layers are closely located [2.07] and are described by the so-called Budden's equation [2.15]. An example of such a resonance/cut-off pair can be seen in Fig.2.6, where the wave is evanescent in the region between them [2.07]. This means that if the antenna is located at the low magnetic field side (at the left hand-side of the picture), as it is usually the case, the fast wave encounters the minority ion cyclotron resonance first, where it is partially absorbed, and then the cut-off. For a (H)D plasma the evanescent region is in general very thin, so that the wave can tunnel through it and reach the ion-ion hybrid resonance layer. Here the fast wave

is mode converted into a Bernstein wave, the energy of which will be absorbed by ELD.

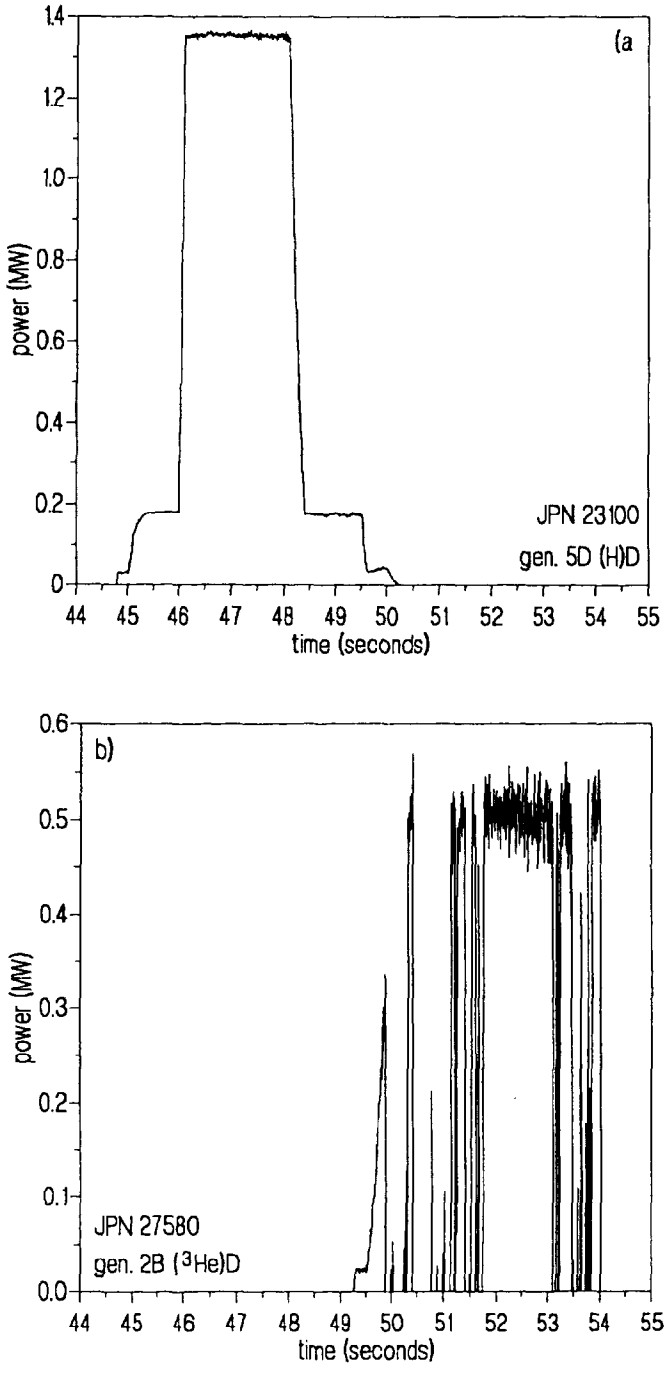

Figure 2.8 RF coupled power for one generator of the JET ICRH plant during a discharge with H minority (Fig.2.8a) and a particularly bad one with ^{3}He minority (Fig.2.8b), in which the trips are due to the very poor coupling of the fast wave to the plasma.

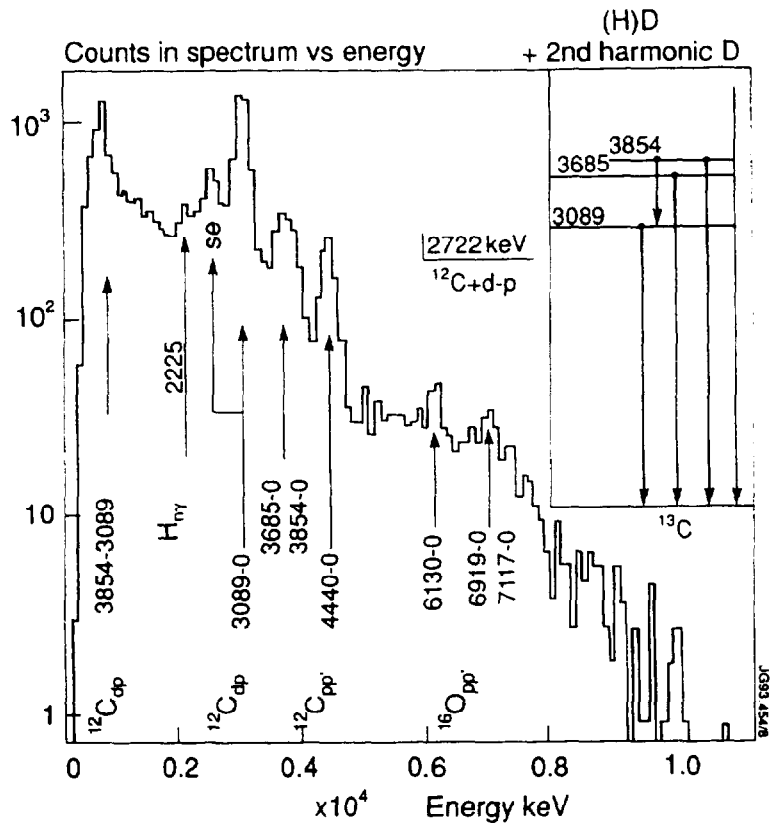

Figure 2.9 Gamma radiation measurements show the existence of high energy minority ions. In this discharge minority heating of hydrogen and second harmonic heating of deuterium were both present. For these measurements particular quantum transitions of ^{13}C have been used (courtesy of D.F.H. Start).

However there are cases (e.g. in a (^{3}He)D plasma) when the size of the evanescent region increases noticeably. In this case only a small fraction on the incident power can tunnel through the evanescent region and reach the resonance, while the remaining part is reflected. Toroidal eigenmodes can then be excited, and peaks in the antenna loading can occur when partially standing waves between the antenna and the cut-off layer reflect the power back to the RF generators through the transmission lines [2.03].

The conclusion that can be drawn from this discussion is that damping of the fast wave with ^{3}He minority is in general weaker than when H minority is present in the plasma. An example of this can be seen in Fig.2.8, where the coupled power of one of the RF generators of the JET ICRH system in dipole phasing ($k_{||}$=7 m^{-1} , see Section 2.5) is plotted against time for two JET discharges with H (Fig.2.8a) and ^{3}He (Fig.2.8b) minorities. When hydrogen is used the antenna-plasma coupling presents no problems, the forward power waveform is smooth and the reflected power is kept to a minimum. On the contrary in the helium case the fast wave crosses a very thin

cyclotron layer, where absorption is weak. The wave is thus partially reflected, and the forward part eventually encounters the cut-off layer, far apart from the ion-ion hybrid resonance. The wave is again reflected (the transmitted part is almost lost in the evanescent region) and a standing wave sets in. As a consequence the generator protection system is triggered, and trips cut the forward power. The overall effect is, of course, that coupling to the plasma in this case is poor.

During minority damping the distribution function of the resonant minority ions undergoes a major modification, developing a high energy tail. It will be shown in Chapter 4 that, when the electron slowing-down dominates, the pitch-angle averaged steady-state Fokker-Planck equation for the minority distribution f can be solved analytically [2.12] and that f is Maxwellian in shape, but with an effective temperature (called the tail temperature) much greater than the background ion temperature, even of order of a few MeV. Experimental evidence for the existence of high energy minority ions responsible for the creation of the tail is shown in Fig.2.9.

In JET it has been found [2.16] that at low concentration (a few percent) the fast ions produce high electron temperatures (as in Fig.2.10), while they do not seem to affect the background ions to a great extent. This means that energy is transferred from the fast ions mainly to the electrons and not to the ions. This phenomenon is easily explained if we note that the cross section for Coulomb collisions, which are responsible for the energy transfer, falls off with the relative velocity of the particles. Since the fast ions are accelerated to velocities much greater than the background ions thermal velocity, collisions with the latter are not very likely to occur. On the contrary, even though the fast ions velocity is well below the electron thermal velocity, the energy can be transferred more easily by minority ion-electron collisions. The electrons will eventually thermalize on the background ions, increasing the ion temperature.

However it has been recently shown [2.11] that ion heating through minority ion slow down directly on the background ions can be of the same order of magnitude of electron heating, depending on the minority species and on its concentration. It has also been shown mathematically [2.17,2.18] that at the RF power levels used in JET the classical Stix model [2.12] generally adopted to estimate the fast wave heating of a two ion species plasma is inadequate, since finite orbit effects are relevant to modify the minority ion distribution function and the electron power density deposition profile (see Chapter 4).

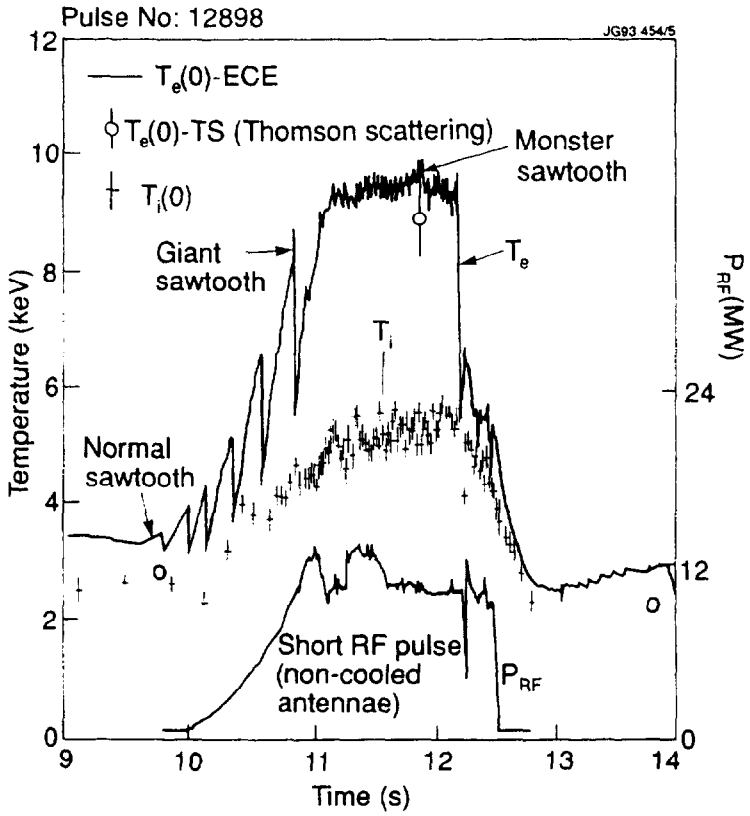

Figure 2.10 An example of high electron temperature regime in JET. The plasma is (^{3}He)D with $I_p = 2.5$ MA, $B_0 = 2.4$ T, $\overline{n}_e = 2 \times 10^{19}$ m^{-3}, and $\overline{T}_e = 3$ keV (courtesy of D.F.H. Start).

2.2.2.2 Mode Conversion

It is by now common knowledge that cyclotron damping at the ion cyclotron frequency is accompanied by mode conversion into the ion Bernstein mode at the ion-ion hybrid resonance layer. In some heating scenarios mode conversion can become as important as cyclotron damping. This happens because for small $k_{||}$ values, when the antenna coupling is more effective, mode conversion becomes stronger while cyclotron damping is weaker [2.19] due to the decreased width of the absorption layer.

What follows is a brief review of the most important methods used in treating mode conversion problems. No effort is here made to apply them to specific propagation problems, for which the interested reader is referred to the literature. Slab geometry is considered, with all quantities varying in the x direction.

Mode conversion is a linear process which takes place in an inhomogeneous plasma where two separate branches of the dispersion relation have the same value of the wavevector k at a point x_0 [2.03,2.12,2.19,2.20]. This causes the energy flux of the

incident wave to be split into separate fluxes of (generally two) independently propagating modes [2.03,2.19].

Pioneering work is due to T.H. Stix [2.21] who considered the propagation of the lower hybrid wave in a cold plasma. Stix showed that when warm plasma corrections are included the cold plasma resonance disappears, and a warm ion mode is born which couples to the original cold plasma mode. The addition of ion cyclotron motion gives rise to ion Bernstein modes which couple to each other and to the already present warm ion mode. At the heart of Stix' theory is the kinetic Bernstein dispersion relation [2.22] and the WKB approximation for a nonuniform plasma. The introduction of nonuniformities has important consequences. First, the wavevector k can vary in space, allowing branches of the dispersion relation to couple. Secondly, the distribution of saddle points of the dispersion relation in the complex k space (and corresponding branch points in the complex z space) can be determined. However the WKB approximation breaks at the branch points, where k varies rapidly, so that the energy exchange cannot be studied using the WKB theory only.

Stix had the idea to associate a differential equation (usually of the fourth order) to the local dispersion relation the asymptotic solutions of which can be found by means of a suitable integral-transform method. The differential equation in general reads [2.03,2.19,2.21],

$$E^{iv} + \lambda^2 x E'' + \delta\lambda^2 E' + (\lambda^2 x + \gamma) E = 0 \ ,$$

where γ and δ are complex constants, while $\lambda^2 > 0$. The superscripts indicate the derivative of the electric field E with respect to x. Even if very successful, Stix' theory has three important drawbacks. First, it is technically difficult to treat analytically a fourth order differential equation with variable coefficients. Secondly, the form of the differential equation can be ambiguous since there is no *a priori* prescription for the commutation properties between functions and the differential operators applying to them [2.20]. For instance in the inverse Fourier transform usually involved to find the differential equation, the terms,

$$adE/dx \qquad \text{and} \qquad d(aE)/dx \ ,$$

give the same Fourier transform if a is a constant coefficient in an homogeneous system [2.03]. Third, the dispersion relation in general contains the plasma dispersion function Z, which needs to be expanded in the wavenumber power series. However if no asymptotic approximation of Z can be justified, then the dispersion relation in

general cannot be put in polynomial form and as a consequence no differential equation can be found.

Partial solution to these problems was given by Heading [2.23] while working on a problem connected to the propagation of radio waves in the ionosphere. His main contribution involves the matrix formulation of a given n-th order linear differential equation with variable coefficients to obtain a matrix equation the diagonal elements of which give the WKB approximation $\exp\int q_i dx$, where q_i are the characteristic values of the original coefficient matrix. The WKB solutions represent waves in regions where they propagate independently. Departure from the local approximation occurs in regions where $q_i(x)$ merge (pairwise) as certain non-diagonal elements become very large and cannot be neglected.

More recently Chan et *al.* [2.24] noted that the WKB solutions of the fourth order differential equation describing the conversion of the lower hybrid wave into the warm plasma mode allow to extract a complex phase factor common to both waves, thus reducing the solution to a potential obeying a second order equation. This has important consequences, because it shows that mode conversion produces a backward propagating wave, like the specular reflection at a cut-off, but at a non-zero value of k and involves a change in the wave type, say from forward to backward [2.20].

Chan and Heading's formulations however fail to determine the actual forms of the common wavenumber and of the scattering potential. This is done by Fuchs, Ko and Bers [2.20] in a fundamental work where the problem of mode conversion is dealt with from a general point of view. In a very elegant way they extract the coupling equations by using the basic analytical properties of the mapping $z \rightarrow k$ and represented by the dispersion relation,

$$D(k,z) = 0 \, .$$

The method gives further insight into the formal and physical structure of mode coupling, and leads to an estimate of the needed quantities. It is also not restricted to dispersion relations that are polynomials in k. In a later work, Bers, Fuchs and Harten [2.25] extend the model and estimate the fraction of mode converted energy.

A theory in some respects similar was formulated by Cairns and Lashmore-Davies [2.26,2.27]. A comparison between these two models is given by Lashmore-Davies et *al.* [2.28].

2.2.2.3 Transit Time Damping

Consider the fast wave at a frequency much lower than the ion cyclotron frequency: all absorption effects due to cyclotron damping are now unimportant. However finite temperature effects give rise to other interesting phenomena at the frequency $\omega = k_{\parallel} v_{\parallel}$ [2.04]. One of them is the usual Landau damping, which will not be discussed here. The second one instead comes from the interaction of the charged particle magnetic moment $\mu = m v_{\perp}^2 / 2B$ (which in these conditions is an adiabatic invariant) with the parallel gradient of the parallel magnetic field. The particles then obey the following equation of motion [2.04],

$$m \frac{dv_{\parallel}}{dt} = -\mu \frac{\partial B_z}{\partial z} . \tag{2.9}$$

Note that this equation is equivalent to the Coulomb force equation when -μ is replaced with the particle energy and $\partial B_z/\partial z$ with the electric field in the z direction. It could then be said that transit time damping is the magnetic equivalent of ELD [2.04].

Eq.(2.9) is in principle valid for all charged particles, as long as the period of the oscillating field is comparable to the particle time of transit through the region where the field is applied, and the process can be considered collisionless. However the fast wave is damped mainly by electrons, because only electrons have the range of parallel velocities necessary to match the parallel component of the phase velocity of the fast wave.

This process forms the basis of the heating mechanism known as *Transit Time Magnetic Pumping* (TTMP) and was originally proposed by L. Spitzer, Jr. for ion heating. The power absorbed per unit volume P can be calculated in a standard way from the anti-Hermitian part of the susceptibility tensor [2.29]. For a shifted bi-Maxwellian velocity distribution and assuming that $E_{\parallel}$=0, then P reads [2.29],

$$P = \sum_s \left\{ \beta_{\perp} \frac{T_{\perp}}{T_{\parallel}} e^{-\lambda} [I_0(\lambda) - I_0'(\lambda)] \cdot \frac{\mu_0 |B_{\parallel}|^2}{2} \sqrt{\pi} \frac{\omega(\omega - k_{\parallel} v)}{|k_{\parallel}| w_{\parallel}} \exp\left[-\left(\frac{\omega - k_{\parallel} v}{k_{\parallel} w_{\parallel}} \right)^2 \right] \right\}_s , \tag{2.10}$$

in which $\beta_{\perp} = 2\mu_0 n T_{\perp} / B^2$, I_0 is the modified Bessel function of integer order n=0 and argument $\lambda = k_{\perp}^2 T_{\perp} / m\Omega^2$ (see also Section 2.2.1), $w_{\parallel} = 2T_{\parallel}/m$, and the sum is carried

out over all plasma species. From Eq.(2.10) it follows that the power density absorbed by the plasma through TTMP is proportional to $\beta_{\perp}$, that is the process is more likely to occur at high 9perpendicular) kinetic pressure.

As a matter of fact TTMP acts always combined with ELD. In fact although the Faraday screens in front of the RF antennae cancel out the E_z component of the electric field while the wave is being launched, in the plasma the wave field is modified and a small E_z component is created, which contributes to Eq.(2.9) with a eE_z force to accelerate the electrons in the direction parallel to the magnetic field.

2.3 Fast Wave Current Drive and Sawtooth Control Experiments

Use of the fast wave to generate non inductive current in the toroidal direction in a two species plasma war first proposed by Fisch [2.30]. The physical principle of Fast Wave Current Drive (FWCD) as proposed by Fisch is relatively simple. It is based on two steps;

- induce the minority ions to drift toroidally relative to the majority ion species;
- use the reaction of electrons to the modified ion distribution to produce a net current.

The first step can be achieved by creating an asymmetric ion drag [2.30]. For instance, minority ions moving, say, to the left may be induced to collide more frequently with the background ions than those moving to the right. The minority ions then move on average to the right, so that by conservation of momentum the background ions move to the left. This can be done by selectively heating the minority ions moving to the right (i.e., parallel to the magnetic field), thus reducing their collision frequency with the majority ions.

Once the first step is satisfied, consider the electron response to oppositely drifting ions with different charged states in the frame of reference where the total ion current vanishes. Since the electrons collide more often with the ion species with larger charge state, a force imbalance arises, leading to an electron drift and, consequently, to a net current.

Fisch calculated that the largest fraction of momentum transferred to the minority ions per unit power dissipated to sustain the process, p/P_d, is obtained when

$\nu_{ie} \cong \nu_{ii}$ [2.30]. Also, Fisch argued that in order to avoid power absorption by the background ions a condition over the wave parallel phase velocity must be satisfied, namely,

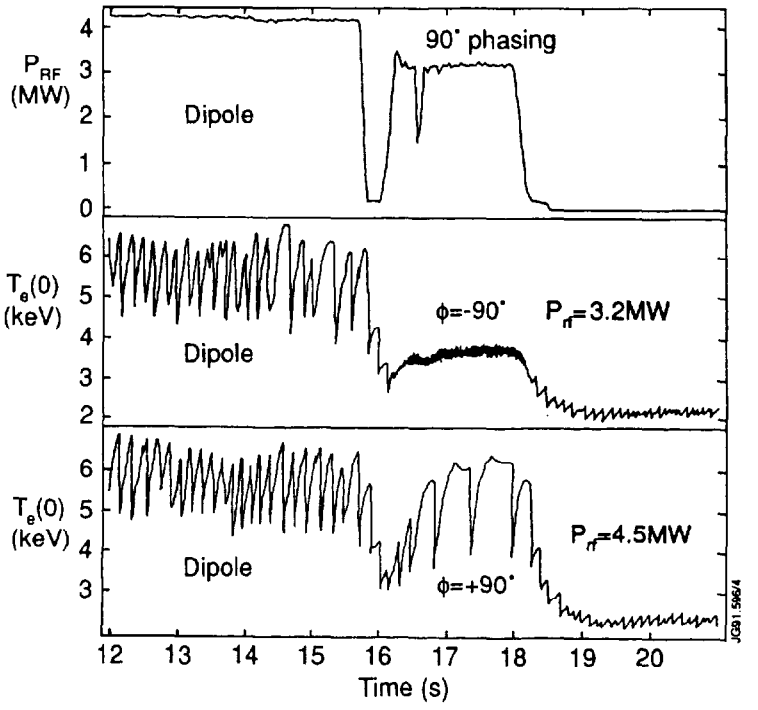

Figure 2.11 Effect of directed fast wave on sawtooth stability [2.31].

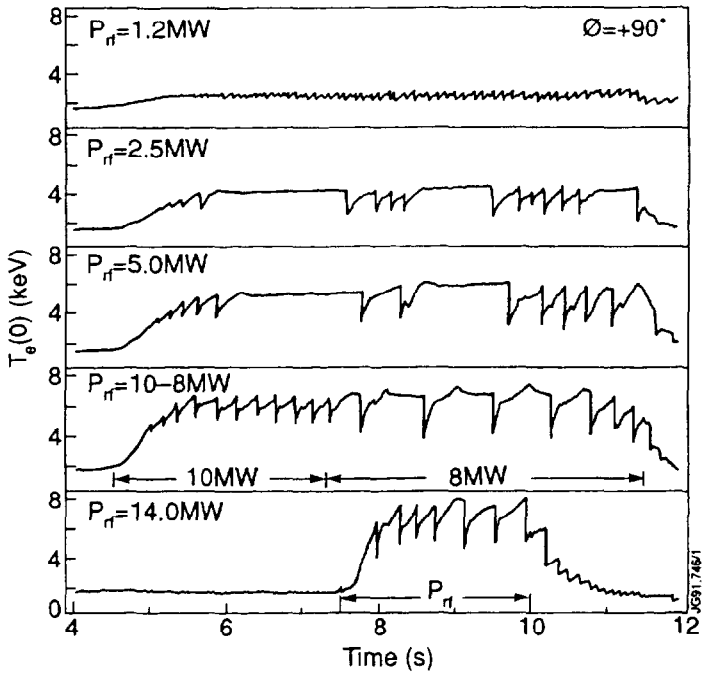

Figure 2.12 Sawtooth behaviour at $\phi=\pi/2$ and different RF power levels [2.31].

$$\frac{\omega}{k_{\parallel}} > \frac{5(m/m_i)^{1/2} - 3}{m/Zm_i - 1} v_{th} \,, \tag{2.11}$$

where v_{th} is the thermal velocity of the minority ions. This condition is obtained for $\omega > \Omega_{min}$, but a similar condition for $\omega < \Omega_{min}$ can be written [2.30]. Eq.(2.10) is equivalent to asking that the $k_{||}$ spectrum produced by the RF antennae be generated in an arbitrary configuration, in general different from either monopole or dipole (see Section 2.4).

Recent modifications now allow the JET ICRF antennae to be arbitrarily phased, and directed $k_{||}$ spectra with phase velocities up to the speed of light can be produced with no accessibility conditions. This new feature has been successfully applied in the JET 1991-92 operations period for the control of sawteeth on the q=1 surface [2.31].

In these experiments the fast wave was resonating near the sawtooth inversion radius and phase of π, $+\pi/2$ and $-\pi/2$ were applied at constant RF power (see Fig.2.11). In the first case (dipole) large sawteeth were produced, with a period of about 0.2s [2.31]. Changing phase to $\phi = +\pi/2$ resulted in stabilization of sawteeth, with an increased period of about 0.5s [2.32]. On the contrary, switching to $\phi = -\pi/2$ had a strong destabilizing effect, with sawteeth of very short period (30ms) [2.31]. Recent theoretical work [2.32] suggests that sawtooth control can be due to stabilization of internal kink modes by modification of the local magnetic shear at the q=1 surface.

A second experiment included a power scan at $\phi = +\pi/2$. Fig.2.12 shows that monster sawteeth were produced and sustained with RF power up to 5 MW. Above this value, the sawtooth period decreased [2.31]. The results of this second experiment are consistent with the hypothesis that FWCD has been produced. In fact an increase in the RF power results in an increase in the tail temperature and, as a consequence, of the perpendicular energy of the minority ions. This leads to acceleration of heated ions into trapped orbits and to an increase of their collisionality with electrons, with consequent reduction of p/P_d.

2.4 The JET ICRH System

The first studies for RF heating in JET date to 1980 and were aimed at providing substantial power with respect to ohmic heating while taking into account of the restrictions imposed by the already existing mechanical structure of the JET tokamak [2.33]. In 1981 it was decided to provide JET of a system capable of delivering 15 MW of ICRH power in a band of frequencies between 23MHz and 57MHz. The design studies showed that an antenna of the required dimensions (mainly determined by the frequency) could be installed through the main ports at the low field side of the vacuum vessel [2.33]. A modular system was thus developed, consisting of two 1.5MW amplifiers mounted in a single module and connected by two co-axial lines onto two loop conductors in a single antenna capable of handling 3MW. Other features decided in the design phase were:

Table 2.1 Nominal characteristics of the JET ICRF plant [2.42]

Frequency range	• 23 to 57 MHz (determined by the full field ion cyclotron resonances of deuterium and hydrogen), excluding 39-41MHz.
8 generators	• 4MW output per generator module (20s)
8 antennae	• berillium bars (15° inclination) screen • two adjacent loops operated with either monopole phasing (0,0) dipole phasing (0,π) or a phased array (0-π)
16 transmission lines (generator to antenna)	• each line long 84m rated at 50 kV peak (dia. 230mm, 30Ω)
feedback loops for	• plasma position for constant coupling resistance • RF power level or antenna RF current • phase between antenna conductors • frequency ($\Delta f \cong 1$MHz) for matching • motorized tuning stub for matching • tetrode screen dissipation and anode efficiency (acting on anode voltage)
8 HVDC power supplies: output (2 tubes) driver (2 tubes)	• 345 amp: 16-26 kV controlled by tetrode screen and current • 60 amp: 9-13 kV (remotely preset)

- use of rigid, 30Ω, ceramic insulated 25cm co-axial transmission lines to achieve the necessary voltage capability and reliability of the system;

- use of tuning stubs at the generator end of the long transmission lines to enable rapid on-line matching by frequency variation, together with a broad-band amplifier (±2MHz about the fixed pre-set frequency) with automatic tuning;

- use of integral antenna/limiter structures and all metal slotted electrostatic screens.

It was also realized that the major components of the ICRF antennae should be cooled to allow for long pulse (20s) operations.

The construction of the ICRF system before the 1992/93 upgrading went through two stages with two different antenna systems, named A_0 and A_1 (the upgraded system will consist of the so-called A_2 antennae). At first it was decided to install the two A_0 uncooled antennae for short-pulse operations only in order to obtain design data [2.33]. Later on the six cooled A_1 were installed for long-pulse operations, with the intention to upgrade the system to a final configuration of ten antennae by 1988 [2.33]. After various changes in order to include new developments and different requirements, the final A_1 system consisted of eight modules. The RF plant specification (upgraded 1989) is reported in Table 2.1.

2.4.1 The RF Generators

The design of the RF generator plant is based on the requirements for heating at the fundamental ion cyclotron frequency of either hydrogen or ^{3}He or second harmonic heating of deuterium, covering the frequency range 23-57MHz. In this range high power tetrodes are commercially available, and their technology is well established.

The generator design is of the tandem type, with two identical amplifier chains having their outputs combined, depending on their phase, in the antenna [2.34]. The selected power can be delivered into load mismatches of up to 20% reflected voltage (Voltage Standing Wave Ratio VSWR=1.5) for up to 20s [2.33,2.34]. Each amplifier chain consists of three tetrodes, the pre-driver, the driver and the endstage, producing 15kW, 100kW and 2MW of output power, respectively (1989 upgrade) [2.34]. For the generators specification, see Table 2.2. The generator is designed to operate in a bandwidth of ±2MHz centred on the selected frequency. The 4MHz bandwidth enables rapid matching of the generator by changing the frequency to compensate for changes in antenna coupling to the plasma [2.33,2.34].

The frequency range cannot be covered in one go during operations, but it is divided into eight channels, with reduced output power at the band edges of 1.6MW. After the latest upgrading (1992/93) it should be possible to deliver full 4MW at the edge as well [2.34].

The driver and endstage tubes are water cooled, while the pre-driver is air cooled [2.34]. Due to the high DC power supply used, the generators are protected

against flashovers by ignitrons which short-circuit the DC supplies, causing them to shut-down. The complete generator unit is mounted on a single transportable pallet isolated from local ground [2.33]. The unit is grounded to the tokamak during operations and grounded locally during test load to avoid DC loops on the vessel through the RF transmission lines [2.33]. During operations the plant is remote controlled from the machine Control Room through the JET COntrol and Data Acquisition System (CODAS) [2.33, 2.34].

Table 2.2 JET RF generator design specification 1990 [2.34]

output tube	Thomson TH525
power output at band centre	2 MW
anode dissipation	1.5 MW
anode current	160 A
anode voltage	27 kV
screen grid current	4 A
maximum tested output power anode dissipation	2.5 MW 1.7 MW
drive tube output power	Siemens SK 2054 >100 kW
pre-driver tube output power	Eimac 8990 15 kW

The main problem in the design of the RF generators was to deliver the requested power to a plasma whose parameters can widely and sometimes rapidly change during the discharge, thus causing an ever-changing fraction of the forward power to be reflected back through the transmission lines towards the generators. This reflected power can be partially compensated by shifting the RF frequency bandwidth range during the pulse, thus 'electrically' adjusting the transmission line length [2.33]. However a fraction of the reflected power can still reach the generator. Depending on the phase angle of the reflected power, any of the normal ratings in the Thomson tube of the endstage can be exceeded (e.g., anode dissipation or screen grid current). When this occurs, a limiter protection system automatically acts to reduce the forward power during the pulse.

2.4.2 The RF Transmission Line System

The RF generators are connected to the antennae through a system of co-axial transmission lines, each 84m in length [2.34]. Their characteristic impedance of 30Ω has been chosen to improve the bandwidth and reduce the voltage on the line. It is a non-standard line system, whose components have been developed for JET from the existing 50Ω technology [2.33].

The transmission line system not only transfers power from the RF generators to the antennae, but is also an important part of the system used to match the ensemble generator-antenna to the plasma. The situation is in fact similar to having a transmission line terminated by a load (the plasma) the impedance of which (a few Ohms) is not equal to the characteristic impedance on the line (30Ω). As a consequence the current and voltage in the load cannot match the current and voltage of the incident wave, and there will be a reflected wave sent back along the line, rejecting the wave energy back towards the generator [2.34].

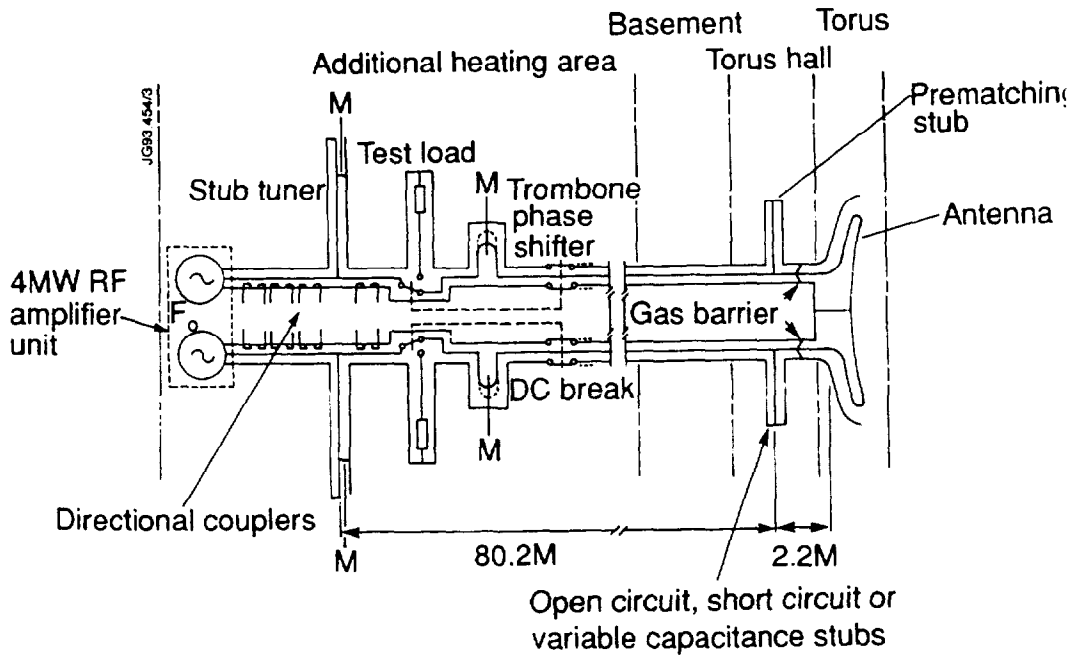

Figure 2.13 Block diagram of the JET ICRH transmission line system. The different components are identified in the picture [2.34].

The matching is provided by a stub tuner located at the generator end of the line, as shown in Fig.2.13, the length of which changes in real time during the pulse, combined with an automatic matching control system by frequency adjustment [2.33,2.35]. This in practise changes the electric length of the line by changing the wave frequency [2.34]. Small variations in the frequency cause rapid changes in the complex line impedance, which is a function of the number of electric wavelengths in the line, until it reaches a value sufficiently near to the 30Ω of the characteristic impedance [2.34].

In more detail, the system makes use of the properties of the ratio $\overline{\sigma}$ between the reflected and forward waves at the stub junction [2.36]. The module and the phase of both waves can be measured by means of directional couplers located at both sides of the stub base. The perfect matching conditions are then given by,

$$\mathrm{Re}(\overline{\sigma}) = 0 \quad \text{and} \quad \mathrm{Im}(\overline{\sigma}) = 0 \ . \tag{2.12}$$

It can be shown [2.34] that given any initial condition, the perfect match is found by imposing first,

$$\mathrm{Re}(\overline{\sigma}) = \frac{\rho}{\cos\theta}\cos(\phi + \theta) = 0 \ , \tag{2.13}$$

where ρ is the modulus of the load reflection coefficient, $\phi = \phi_1 - 2\beta l$ is the phase of the reflected wave at the stub junction, with $\beta = \omega / c$, l length of the line and ϕ_1 phase of the reflected wave, while,

$$\tan\theta = \frac{1}{2}\tan(\beta l_s) \ ,$$

where l_s is the stub length. Condition (2.13) can then be satisfied by means of a feedback loop acting on the angular frequency ω (or, equivalently, ϕ). Once Eq.(2.13) is satisfied, the other condition,

$$\mathrm{Im}(\overline{\sigma}) = \rho - \sin\theta = 0 \ , \tag{2.14}$$

is fulfilled by means of an automatic loop acting on the stub length (or θ).

Since the antenna is designed in two halves (see later), each fed by an independent transmission line, a problem of equalizing to a high degree of precision the electric length of the two lines arises. A trombone phase shifter has thus been introduced, with the specific task of coupling the two halves of the antenna by adjusting the phase settings during the pulse [2.36].

2.4.3 The JET ICRF Antennae

The prototype A_0 antennae were uncooled and designed for short pulse operations only, in order to investigate in fields like coupling efficiency to the plasma, impurity production, RF current and voltage limitations on the antenna and the transmission lines [2.33].

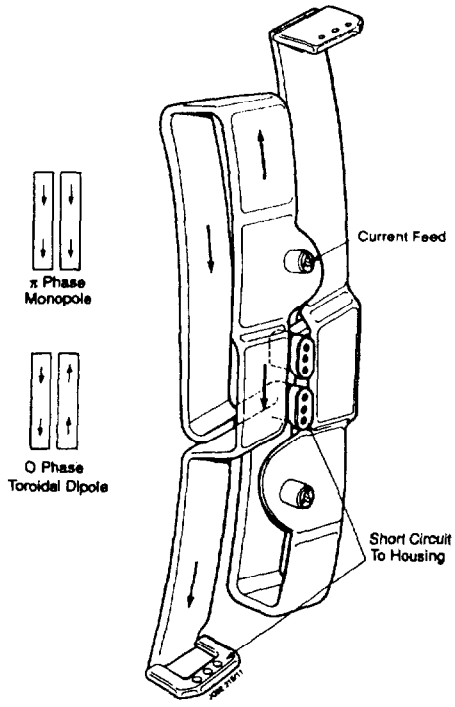

Figure 2.14 Central conductor of the A_1 antenna. The circulation of the current in the straps and the monopole/dipole phase current configurations are also indicated [2.34].

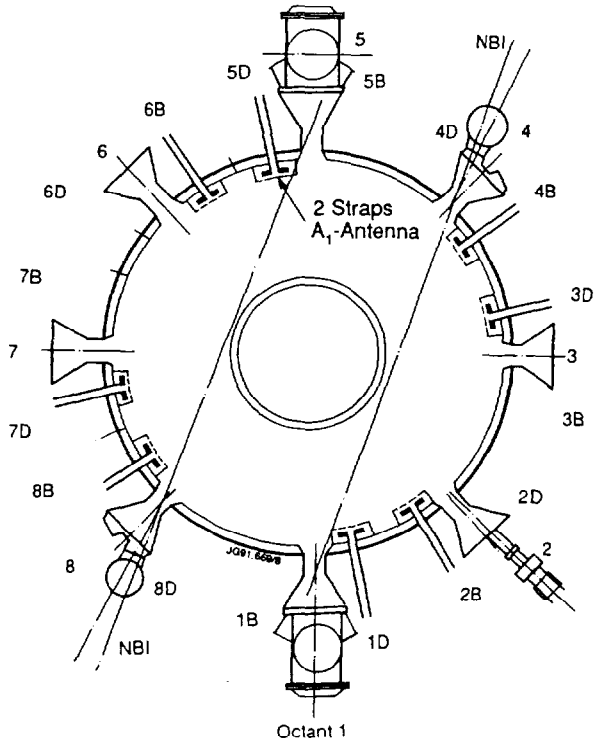

Figure 2.15 Position of the eight A_1 antennae in the vacuum vessel [2.41].

The A_1 antennae were designed on the basis of the data obtained from A_0. A picture of the A_1 central conductors is shown in Fig.2.14, while a layout of the position of the antennae in the torus can be seen in Fig.2.15. In both cases, though, design constraints were imposed by the pre-existing features of the vacuum vessel. In particular, the antennae must be located in a space 150mm wide between the plasma scrape-off layer and the wall, while the transmission lines have to enter the torus through the limiter guide-tubes [2.33]. Also, a clear view for diagnostics imposed the design of a very compact double vacuum-tight RF window [2.33].

Physics demands impose other restrictions, the most important of which is that the antennae must be very close to the plasma edge (≅30mm) in order to achieve efficient coupling. The main drawback in this setting is that the sides of the antenna are constantly bombarded by high energy particles, causing sputtering and high Z impurity release. Also the antenna conductor needs to be protected from the plasma itself. Screening with a low Z material is therefore necessary. This has been achieved by means of an electrostatic (Faraday) screen, originally in nickel [2.33] and now in berillium [2.37]. The Faraday screen is placed in front of the antenna conductors and consists of a series of shaped radiation cooled bars at an angle of about 15° with respect to the horizontal axis [2.38]. At this angle the bars are aligned with the total magnetic field at the edge during 5MA discharges at B_ϕ=3.4T (in most discharges the angle of the magnetic field lines at the edge is about 10°) [2.39]. Use of berillium as screening material has reduced considerably the production of impurities, the mechanisms of which are now well understood [2.39]. The alignment of the screen bars with the magnetic field allows to launch the fast wave with the correct polarization, suppressing the excitation of the slow wave and of surface modes, thus avoiding heating at the plasma edge.

The A_1 antennae have been designed to resonate at 42.7MHz, close to the fundamental ion cyclotron frequency of H on the magnetic axis at a magnetic field of 2.8 T. They are made of two straps of conducting material, each fed by one (up/down) transmission line. When the straps are fed out of phase (ϕ=0, or *monopole* phasing) the radiated spectrum is peaked around $k_{||}$=0, the peak occurring in front of the antenna. When instead the straps are fed in phase (ϕ=π or *dipole* phasing) the peak of the radiated spectrum is shifted away from the origin towards values of $k_{||}$ for JET typically around 7 m^{-1}. The names monopole and dipole are used because the $k_{||}$ spectrum is in many respects similar to that produced by a single current strap and by an oscillating dipole, respectively [2.40]. During 1991/92 operations a new system for

the control of the phase setting has been successfully used [2.41]. The system allows the RF antennae to be set at an arbitrary phase other than monopole or dipole for current drive experiments. Examples of $k_{||}$ spectra for ϕ=0, π, $\pi/2$ are shown in Fig.2.16.

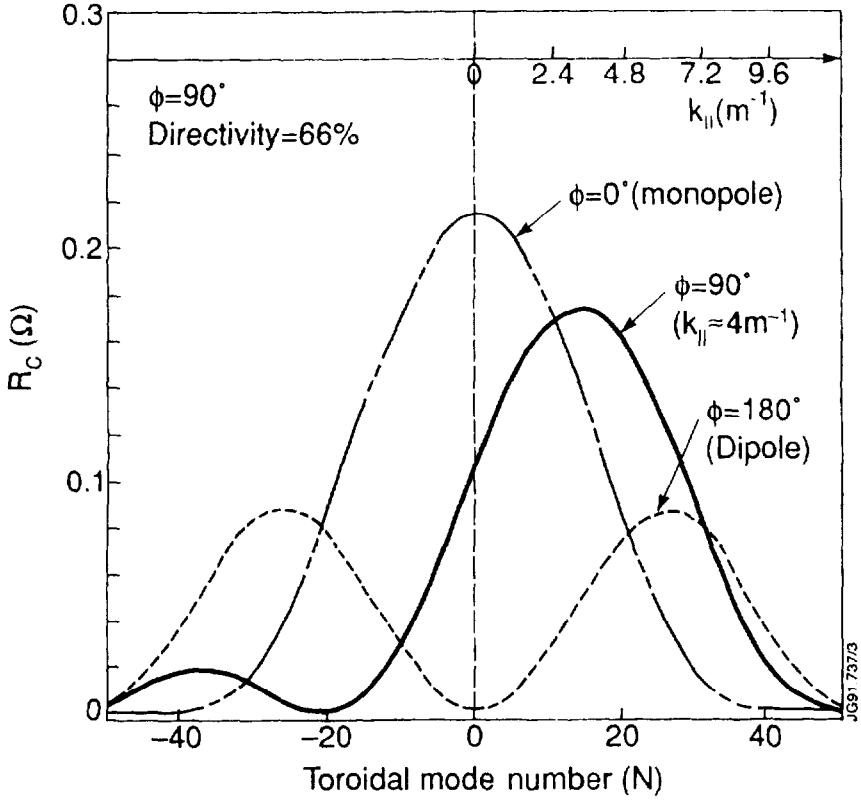

Figure 2.16 Parallel wavevector spectra for ϕ=0 (dipole phasing), ϕ=$\pi/2$ (arbitrary phasing) and $\phi = \pi$ (monopole phasing) [2.31].

2.4.4 The Pumped Divertor Phase Upgrading

During the 1992/93 shut-down for the installation of the new pumped divertor the ICRH system underwent another upgrading. The most noticeable change is the installation of the new A_2 RF antennae, one of which is shown in Fig.2.17. The change was necessary in order to couple RF power to a smaller, vertically elongated plasma having a magnetic configuration with a single (bottom) null point [2.42]. The new system consists of four arrays, each with four conducting straps to form a monopole, dipole quadrupole or arbitrary phase setting [2.43]. The antennae are located in the torus as in Fig.2.18 (cfr. with Fig.2.15). Consequently, approximately half of the ICRH transmission line system had to be re-located and re-grouped [2.42]. Each strap is fed by one amplifier. The existing generator output limit of 2MW for

long pulse operation has been removed [2.44], allowing the system to run up to its technological limits.

A technical treatment of the JET ICRH plant is beyond the aim of this Section. However it is necessary to point out that the old system (before 1993) had a series of drawbacks, which hopefully have been eliminated during this latest upgrading. Other problems related to the interaction of the new A_2 antennae with the RF plant have been taken care of as well. The main improvements can then be summarized as follows [2.44]:

- the operations of the four amplifiers in the same group is closely coordinated, since the A_2 antenna straps will be tightly coupled;
- a new phase control system allows better amplitude and phase control for current drive;
- matching with the A_2 antenna array is more difficult, so that a more sophisticated matching control system is required;
- narrowing the RF signal detection band reduces cross coupling between modules, now cause of spurious trips;
- modern electronics replaces the 10 years old existing technology.

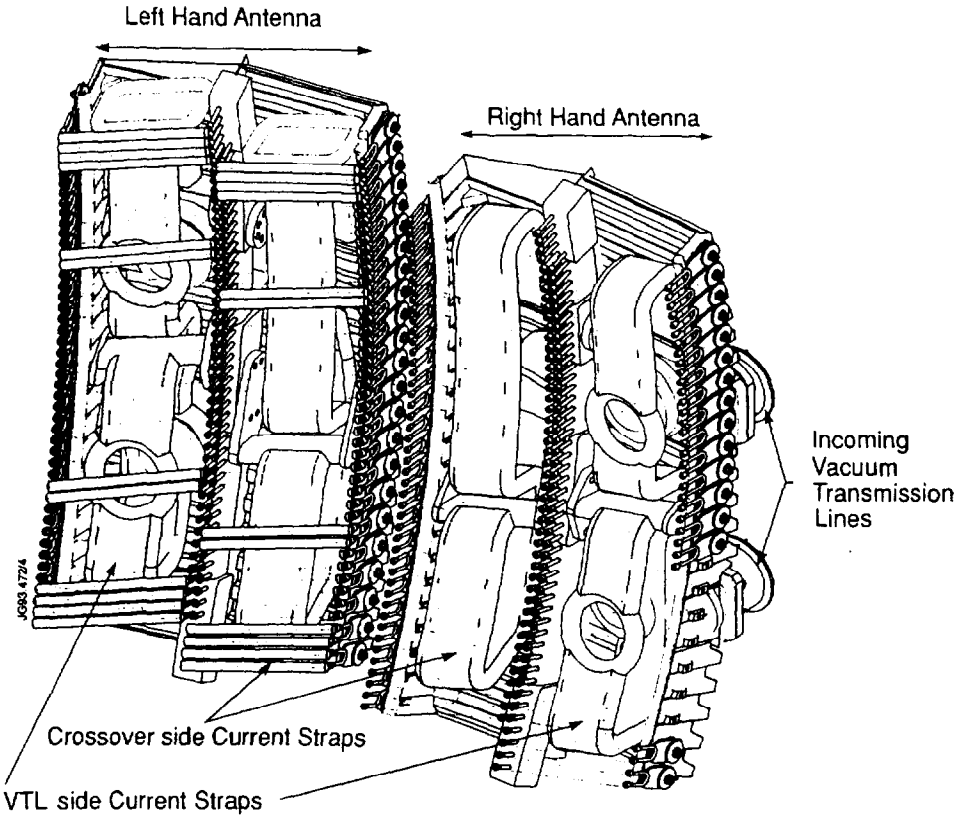

Figure 2.17 The new A_2 antenna used in the JET Pumped Divertor Phase (1992/1996).

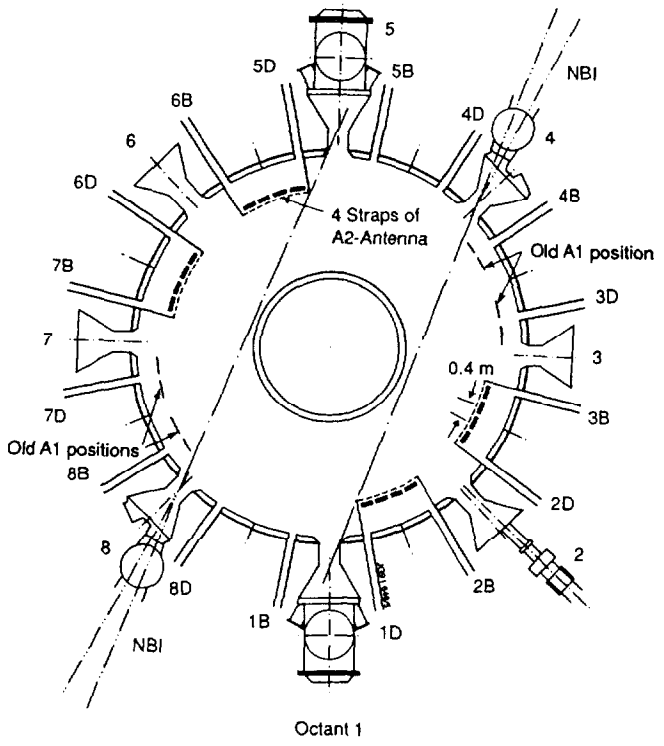

Figure 2.18 Position of the new A_2 antennae in the JET vacuum vessel [2.41].

2.5 References

1. J.P. Freidberg, *Ideal Magnetohydrodynamics*, Plenum Press, NY (1987).

2. Cross, *An Introduction to Alfven Waves*, Adam Hilger, Bristol (1987).

3. R.A. Cairns, *Radiofrequency Heating of Plasmas*, Adam Hilger, Bristol (1991).

4. T.H. Stix, *The Theory of Plasma waves*, McGraw-Hill, NY (1962).

5. A.I. Akhiezer et *al.*, *Plasma Electrodynamics-Vol. I: Linear Theory*, Pergamon Press, Oxford (1975).

6. J. Wesson, *Tokamaks*, Clarendon Press, Oxford (1987).

7. H. Takahashi, Jour. de Phys., suppl. to no. 12, **38** (1977), c6-171.

8. A.C. Riviere, in *Plasma Physics and Nuclear Fusion Research* (R.D. Gill Ed.), Academic Press, London (1981), p. 501.

9. M. Porkolab, in *Heating in Toroidal Plasmas* (B. Coppi et *al.* Eds.), Pergamon Press, Oxford (1978), p. 339.

10. L.-G. Eriksson et *al.*, Nucl. Fusion **29** (1989), 87.

11. D.F.H. Start et *al.*, JET Report JET-R(91)06.

12. T.H. Stix, Nucl. Fusion **15** (1975), 737.

13. C.F. Kennel and F. Engelmann, Phys. Fluids **9** (1966), 2377.

14. S.J. Buchsbaum, Phys. Fluids **3**, (1960), 418.

15. K.G. Budden, *Radio Waves in the Ionosphere*, Cambridge University Press, Cambridge UK (1961).

16. J. Jacquinot et *al.*, in *Application of Radio Frequency Power to Plasma*, (S. Bernabei and R.W. Motley Eds.), American Institute of Physics, NY (1987).

17. L.-G. Eriksson and F. Porcelli, JET Report JET-R(91)11, p.15.

18. E. Righi et *al.*, Proc. Europhysics Topical Conference on RF Heating and Current Drive of Fusion Devices, Brussels, Belgium (1992), p.113.

19. M.J. Alava and J.A. Heikkinen, JET Report JET-P(91)31.

20. V. Fuchs, K. Ko and A. Bers, Phys. Fluids **24** (1981), 1251.

21. T.H. Stix, Phys. Rev. Lett. **15** (1965), 878.

22. I.B. Bernstein, Phys. Rev **109** (1958), 10.

23. J. Heading, J. Res. Nat. Bur. Stand. **65D** (1961), 595.

24. V.S. Chan, S.C. Chiu and G.E. Guest, Phys. Fluids **23** (1980), 1250.

25. A. Bers, V. Fuchs and L. Harten, Proc. 4-th Intern. Symp. on Heating in Toroidal Plasmas **1** (1984), 463.

26. R.A. Cairns and C.N. Lashmore-Davies, Phys. Fluids **25** (1982), 1602.

27. R.A. Cairns and C.N. Lashmore-Davies, Phys. Fluids **26** (1983), 1268.

28. C.N. Lashmore-Davies, R.A. Cairns and V. Fuchs, Phys. Fluids **28** (1985), 1791

29 T.H. Stix, *Waves in Plasmas*, AIP, New York (1992).

30. N.I. Fisch, Nucl. Fusion **21** (1981), 15.

31. D.F.H. Start et *al.*, Proc. IAEA Technical Committee Meeting on Fast Wave Current Drive in Reactor Scale Tokamaks, Arles, France (1991).

32. F. Porcelli, Proc. 18-th EPS Conference on Controlled Fusion and Plasma Physics, Berlin, FRG (1991).

33. A. Kaye et *al.*, Fusion Tech. **11** (1987),???.

34. JET RF Pilot training document, 1991.

35. H.H. Skilling, *Electric Transmission Lines - Distributed Constants, Theory and Applications,* McGraw-Hill, NY (1951).

36. G. Bosia et *al.*, Proc. 15-th SOFT, Utrecht (1988).

37. C.I. Walker et *al.*, Proc. 15-th SOFT, Utrecht (1988).

38. T.J. Wade at *al.*, Proc. 14th Symp. on Fusion Engineering, San Diego, California (1991).

39. M. Bures et *al.*, Plasma Phys. and Controlled Fusion **33** (1991), 937.

40. D.J. Jackson, *Classical Electrodynamics*, John Wiley & Sons, NY (1962).

41. G. Bosia and J. Jacquinot, Proc. IAEA Technical Committee Meeting on Fast Wave Current Drive in Reactor Scale Tokamaks, Arles, France (1991).

42. T.J. Wade et *al.*, JET Report JET-P(92)81.

43. A. Kaye et *al.*, JET Report JET-P(92)46.

44. J.A. Dobbing, private communication.

3.0 Modelling ICRH Data on JET

This Chapter briefly outlines how the experimental quantities relevant to this thesis are measured. Thus, after a brief Introduction in which the criteria used to select discharges suitable for analysis are defined, the physical principles at the basis of measurements of electron temperature and density are introduced (Section 3.2), and the techniques used to derive fast ion energy content, direct electron heating and minority concentration are presented.

3.1 Introduction

The model developed in this thesis applies to steady-state plasmas. Five main criteria have thus been adopted to select time-slices from JET discharges which will be valid throughout the thesis:

1. mainly centrally heated deuterium discharges with H or ^{3}He minorities. In these experiments, the RF frequency is chosen to resonate with the minority fundamental cyclotron resonance within ±0.15m of the magnetic axis;

2. discharges in the datasets with a modulation in the RF power waveform are used to estimate the amount of direct electron heating through TTMP, ELD and mode conversion (see Section 3.4). This is then subtracted from the total coupled power to obtain the net power coupled to the minority ions;

3. near-stationarity of the total measured fast ion energy content W_f for times in excess of one central fast ion energy slowing-down time. Discharges meeting this criterion have fast ion distributions in or near steady-state conditions;

4. discharges in which the MHD sawtooth activity is suppressed for times in excess of one central fast ion energy slowing-down time, so that any fast ion redistribution driven by sawteeth can be neglected;

5. L-mode or monster sawtooth discharges with constant plasma current and toroidal magnetic field but with different RF power levels. Thus the effects of the variation of electron and ion heating with RF power can be examined while removing any possible confusion arising from underlying changes in the energy transport properties associated with different plasma currents.

3.2 Electron temperature and density measurement

In this Section the techniques used to measure the electron temperature and density are briefly introduced. The electron temperature can be measured on JET in different ways, the most important of which are the Electron Cyclotron Emission (ECE) measurement and the LIght Detection And Ranging (LIDAR) Thomson scattering. The electron density instead is measured using either LIDAR, or the Far InfraRed (FIR) interferometer. In the following Sections the physical principles on which these systems are based are briefly reviewed, and the uncertainties in measurements are given.

Throughout the thesis use will be made of the ECE temperature profiles and the density profiles from the FIR interferometer, checking that they do not differ from those from LIDAR by more than ±10%. These profiles will be approximated by the analytical expressions,

$$T_e(r) = [T_e(0) - T_e(a)]\left[1 - (r/a_0)^{\alpha_1}\right]^{\alpha_2} + T_e(a), \qquad (3.1\text{-}1)$$

$$n_e(r) = [n_e(0) - n_e(a)]\left[1 - (r/a_0)^{\alpha_3}\right]^{\alpha_4} + n_e(a), \qquad (3.1\text{-}2)$$

with $\alpha_i = 1,2,3,4$ fitting parameters, while $T_e(0)$, $n_e(0)$ and $T_e(a)$, $n_e(a)$ are the temperature and density in the plasma centre and at the edge, respectively. Such fittings, one of which is shown in Fig.3.1, do not differ from the experimental measurements by more than ±5%.

3.2.1 Measurement of T_e using ECE

Tokamaks have a magnetic field the main component of which varies inversely with major radius and is constant along a vertical line of sight, that is, $B_\phi(R) = B_0 R_0 / R$. This is of consequence when observing the EC emission from the

plasma. Firstly, at right angles to B_ϕ and along the major radius the emission lines are broadened by the magnetic field variation. Then the EC emission, which occurs at discrete harmonics of the electron cyclotron frequency, is spatially localized in the region where the resonance condition,

$$\omega = n\omega_{ce}(R), \quad n = 1,2,3... \tag{3.2}$$

holds. Spatial information about the localization of the emission can therefore be obtained from a measurement of the spectrum of the emitted radiation. From the theory of ECE it is possible to calculate the intensity of emission for both optically thin and thick plasmas [3.01]. An optically thick plasma can be considered as a black body, the emission intensity of which is given by the Rayleigh-Jeans law [3.01,3.02,3.03],

$$I(\omega) = \frac{\omega^2 T_e(R)}{8\pi^3 c^2}. \tag{3.3}$$

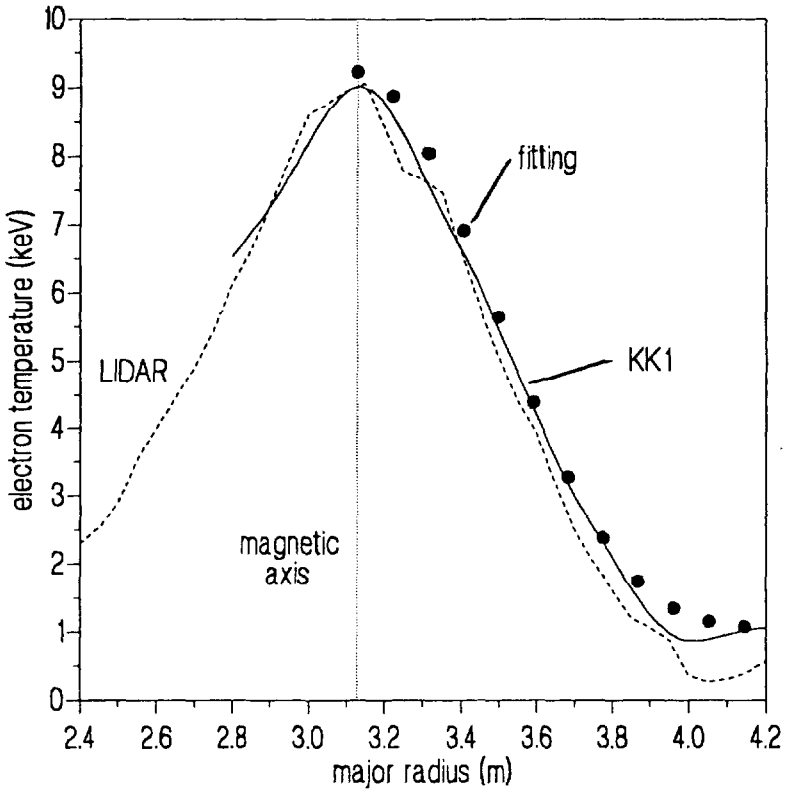

Figure 3.1 **Electron temperature profiles.** Plot of the electron temperature profiles as measured with the ECE diagnostic KK1 (continuous curve) and LIDAR (dashed curve). Overlaid is the analytical fitting of the KK1 signal as given by Eq.(3.1-1).

From the measurement of the frequency dependence of the emission it is thus possible to derive the temperature profile [3.01].

On JET three diagnostics based on the ECE measure the electron temperature profile: the Michaelson interferometer (system KK1), the grating polychromator (KK2), and the heterodyne radiometer (KK3) [3.04]. Although KK1 has only moderate spatial and temporal resolution (≅15cm and ≅15ms, respectively) it provides absolutely calibrated temperature profiles on all plasma pulses when the toroidal field is above 1.5T [3.04]. One such profile is shown in Fig.3.1, together with that obtained with LIDAR. These profiles are used routinely to cross-calibrate the temperatures measured with the other two multi-channel diagnostics, which are difficult to calibrate using black-body sources. It is then possible to use KK2 and KK3 to study in detail the time evolution of the absolute electron temperature at fixed radii with good both spatial and temporal resolution ($\Delta r \cong 6$cm for KK2, ≅3cm for KK3 and $\Delta t \cong 10$ms). The estimated absolute uncertainty for all ECE diagnostics is ±10% [3.05].

3.2.2 LIDAR Thomson scattering

The scattering of an electromagnetic wave provides an effective way to probe the plasma interior with a minimum of perturbation, since it requires only access of radiation to the plasma. Analysis of the scattered radiation provides detailed information on the electron temperature and density.

An electromagnetic wave is scattered by a charged particle as a result of the acceleration of the particle by the electric and magnetic fields of the wave, which causes emission of dipole electromagnetic radiation [3.02]. From a quantum-mechanical point of view, the process could be described as the collision of photons with the particle and their consequent 'bouncing off' in different directions. From a mathematical point of view, the two descriptions lead to identical results if the change in the mean particle momentum during the collision is negligible, that is if $\hbar\omega \ll mc^2$. This is called Thomson scattering, regarded as the classical limit of the quantum mechanical Compton scattering [3.02].

The theory is developed most correctly using a relativistic calculation for the electron motion. The interested reader is referred for example to [3.02] for the details. Here only the main results will be briefly discussed.

When the scattering from a single electron is considered, the Thomson scattering cross-section results to be [3.02,3.06],

$$\sigma_T = \frac{8\pi}{3} r_e^2 = 6.65 \cdot 10^{-29} \ \ m^2 \ , \tag{3.4}$$

where $r_e = e^2 / 4\pi\varepsilon_0 m_0 c^2$ is the classical electron radius. It is then understandable why use of Thomson scattering as a diagnostic had to wait for the development of high power lasers, since the ratio of scattered power to input power for typical plasma densities and scattering volumes is $\sim 10^{-13}$[3.06]. In order to calculate the total scattering, the contributions to the electric field of the scattered wave from each of the electrons must be taken into account. To do this, information about the relative phase of all contributions is needed. If the phases of all contributions can be assumed to be totally uncorrelated, that is when $\alpha \ll 1$, where $\alpha = 1/|k|\lambda_D$, then the total fraction of the incident power scattered over all angles per unit path length is [3.02],

$$n_e \sigma_T = \frac{8\pi}{3} n_e r_e^2 . \tag{3.5}$$

This is called incoherent Thomson scattering. However if the phases are found to be correlated ($\alpha \gg 1$), then collective (or coherent) scattering is observed, which can give information about the ion population in the plasma or about wave phenomena [3.06].

Supposing that the scattering is incoherent, then the form of the scattered spectrum can be estimated [3.06]. For the purposes of the present Section use of the cold plasma approximation can give correct estimates of the magnitude of the scattered signal, even if it is hardly adequate for a detailed analysis in thermonuclear plasmas. The differential scattering cross section $d\sigma/d\Omega$ can thus be calculated, and the net contribution to the spectrum in each frequency interval is determined by integrating the contribution from electrons in each velocity interval. For a Maxwellian velocity distribution, $d\sigma / d\Omega$ becomes [3.06],

$$\frac{d\sigma}{d\Omega}(\omega_s) = \frac{n_e \sigma_0}{\pi^{1/2} ak} \exp\left[-\left[c(\lambda_s - \lambda_0)/\lambda_0 a\right]^2 \left[1/(1-\cos\theta)\right]\right], \tag{3.6}$$

where the subscripts 0 and s refer to the incident and scattered waves, respectively. From Eq.(3.6) it then follows that the electron density is proportional to the intensity of the scattered signal. For a 90° scattering geometry of a laser with $\lambda_0 = 694$ nm and an electron temperature of 100 eV the FWHM of the spectral width is 33nm due to the Doppler effect, that is the spectrum is quite broad in spectroscopic terms, and it can be

easily resolved with simple instruments. The absolute temperature can then be obtained by measuring the scattered light in two different wavelength channels once their relative sensitivity is known [3.06].

On JET both electron temperature and density are measured by combining the Thomson scattering technique at 180° and the time of flight principle [3.05]. First proposed in [3.07,3.08] the system is well suited for measurements on fusion devices, where accessibility of the systems becomes impossible due to materials activation. On JET a short (300 psec) laser pulse is used, and temperature and density are measured with an uncertainty of ±5-10% [3.05].

3.2.3 Laser measurement of n_e

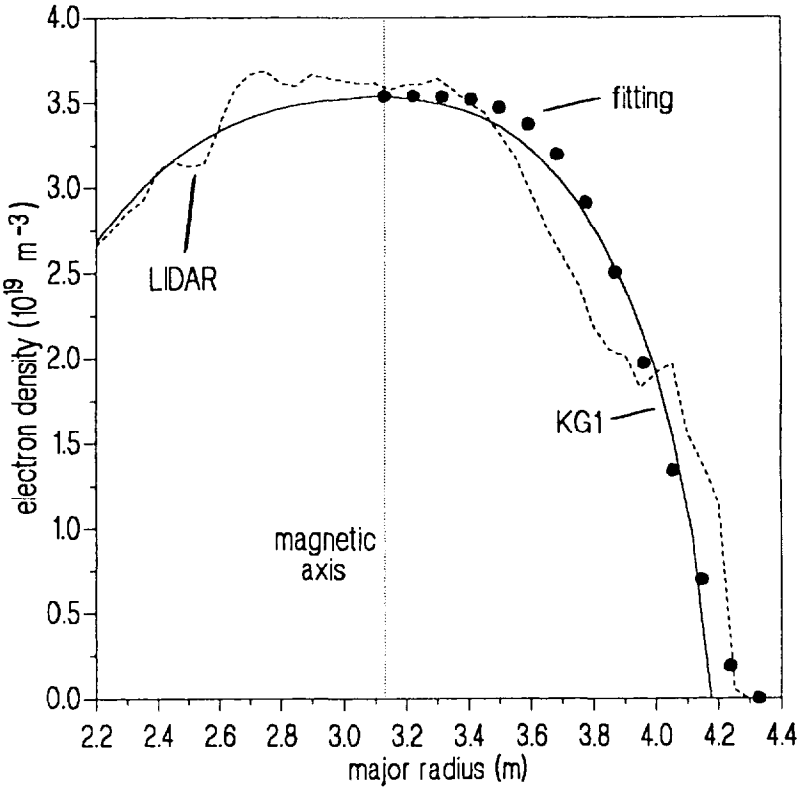

Figure 3.2 **Electron density profiles.** Plot of the electron density profiles measured with the interferometer KG1 (continous curve) and with LIDAR (dashed curve). Overlaid is the analytical fitting of the KG1 profile as given by Eq.(3.1-2).

The plasma electron density can be determined by measuring the change in the refractive index caused by the presence of the electron gas. A laser beam, usually in the visible or infrared range, is then used to probe the plasma and its phase change due to the crossing of the plasma is compared with that of an outside reference beam.

The laser beam is split into three components, one of which is modulated, while the others travel either through the plasma or along a reference path, and then is combined with the modulated component before reaching the detectors. These determine the beat frequency of the signal (typically in the range 1-10^3 kHz). The phase shift of the probing beam is determined from the outputs of two detectors by measuring the time difference Δt between two zero-crossings [3.01]. The measurement of the phase shift determines the line-integrated density $\int n_e dz$ along the chord through the plasma. The electron density profile is then found by Abel inversion of the line-integrated density with a resolution proportional to the number of chords employed.

On JET electron density profiles are obtained using a multi-channel Far InfraRed (FIR) interferometer KG1 based on the principles described above, with an uncertainty of ±10% in the worst cases [3.05]. An example of electron density profile obtained from KG1 is shown in Fig.3.2, together with its analytical fitting from Eq.(3.1-2) and the correspondent profile from LIDAR.

3.3 The fast ion energy content

In Chapter 2 it has been shown that during high power ICRF heating discharges the resonant (fast) minority ions absorb energy in the perpendicular direction which is not shared with the parallel degree of freedom. The fast ions are thus characterized by an excess of perpendicular energy with respect to the isotropic background which can be determined experimentally. To this effect consider the total plasma energy W_{MHD} derived from calculations of the magnetic equilibrium and the total plasma energy derived from diamagnetic energy measurements, W_{DIA}. The fast ion energy is then defined as,

$$W_f = \frac{4}{3}\left(W_{DIA} - W_{MHD} - \Delta W\right). \tag{3.7}$$

An example of fast ion energy measurement is reported in Fig.3.3. This global measurement technique is insensitive to heating regimes in which the fast ions have an isotropic velocity space distribution. Such cases arise in the low energy range $(E \cong E_c)$, where ion-ion pitch angle scattering isotropizes the tail to a large extent, as in the ion heating regime [3.09]. The method of using Eq.(3.7) to determine the fast ion energy content is, in practice, sensitive to the presence of baseline offsets both in W_{DIA} (through calibration errors) and in W_{MHD} (through, for example, non-

equilibrium conditions). In addition, possible systematic baseline offsets in the data (ΔW in Eq.(3.7)) are taken into account by measuring (when possible) W_{DIA} and W_{MHD} at two suitable times, t_1 and t_2 both before and after the application of the RF pulse, and estimating the linear offset,

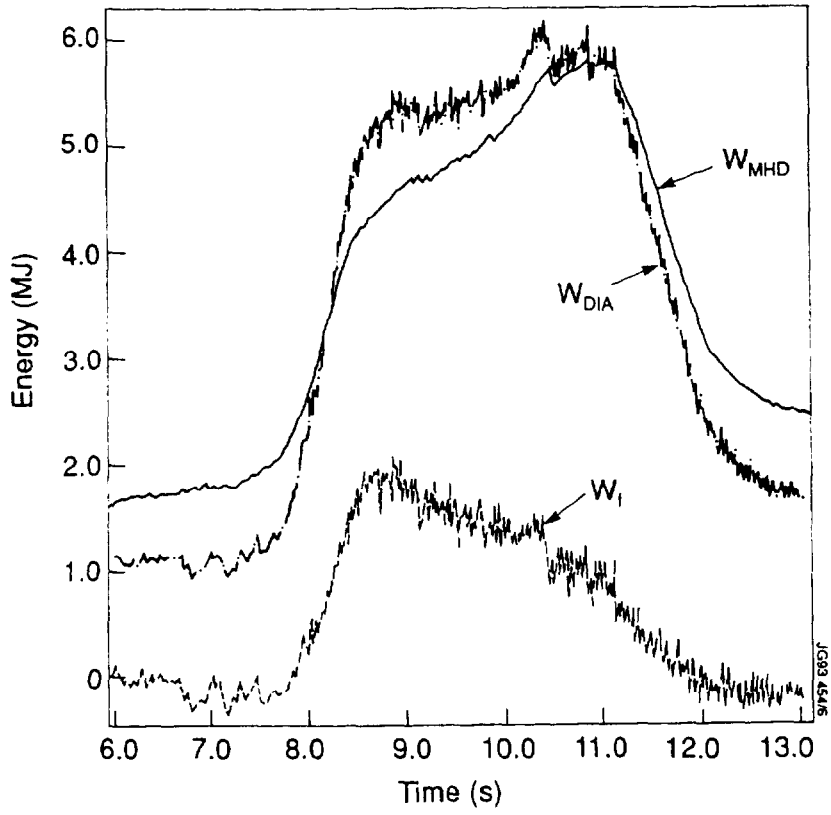

Figure 3.3 Fast ion energy. Example of measurement of the fast ion energy W_f from the total plasma energy measured with the diamagnetic loop, W_{MHD}, and the total plasma energy W_{MHD} from calculations of the magnetic equilibrium.

$$\Delta W(t) = \frac{\Delta W_2 - \Delta W_1}{t_2 - t_1}(t - t_1) + \Delta W_1 , \tag{3.8}$$

where $\Delta W_i = W_{DIA}(t = t_i) - W_{MHD}(t = t_i)$, i=1,2. In this way $W_{DIA} - W_{MHD} = 0$ both before and after RF is applied, a constraint equivalent to assuming a negligible density of suprathermal ions during the steady ohmic heating phase of the discharge. Experimental error in determining the total fast ion energy content have been estimated to be approximately ±20%.

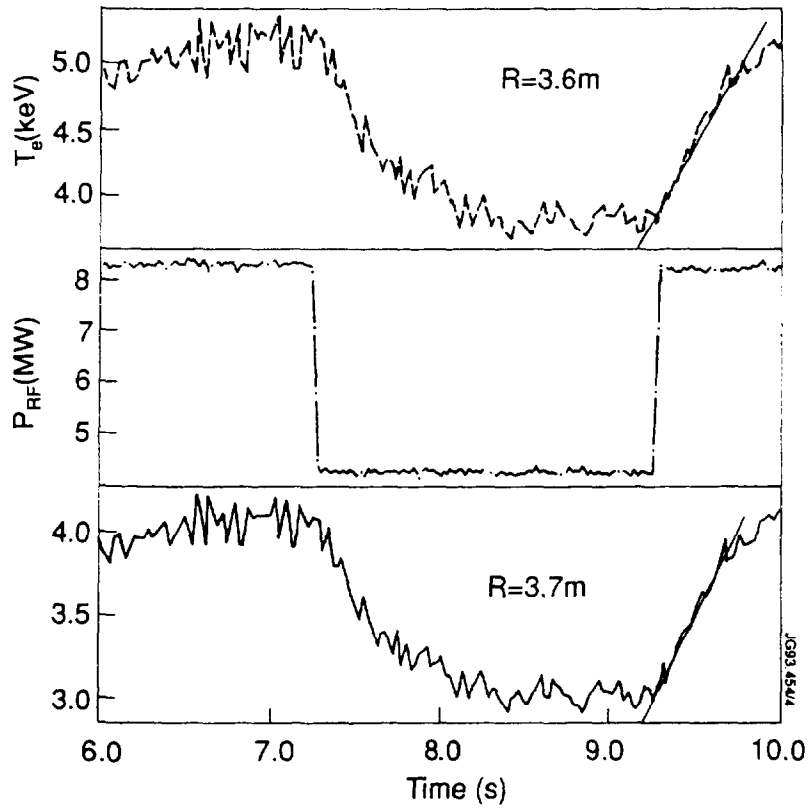

Figure 3.4. Measurement of direct electron heating. The step in the power waveform during RF modulated discahrges is used to measure the temporal response of electron temperature and density at different radii and estimate ρ_{de} in Eq.(3.9).

3.4 Direct electron heating

The fraction of RF power absorbed by the electron population through a combination of TTMP, ELD and mode conversion (collectively called direct electron heating) can be estimated by using measurements of electron density and temperature during RF modulation experiments. With reference to Fig.3.4, at the time $\bar{t}$ of the step in the RF heating pulse the power density damped on the electrons can be written as,

$$\rho_{de}(r,\bar{t}) = \frac{3}{2}\frac{d}{dt}\left[n_e(r,t)T_e(r,t)\right]_{t=\bar{t}}, \tag{3.9}$$

while the total power is simply the volume integral of Eq.(3.9),

$$P_{de}(\bar{t}) = \int_V d^3r\, \rho_{de}(r,\bar{t}), \tag{3.10}$$

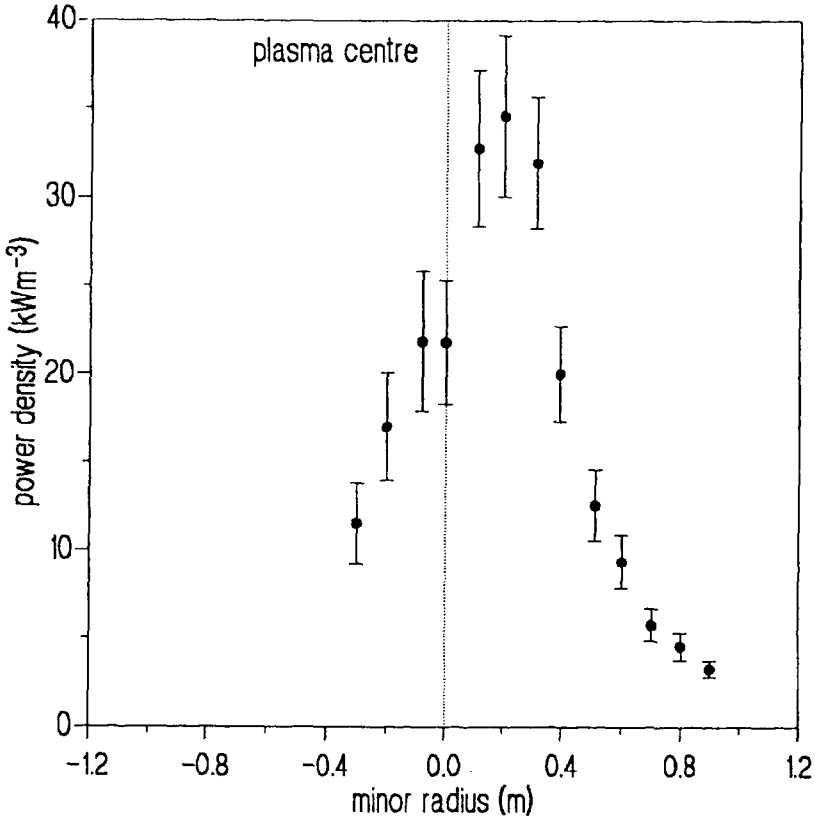

Figure 3.5. Direct electron heating profile.

where V is the plasma volume.

Consider then the profiles of the electron density and temperature, as in Fig.3.4. The time derivative in Eq.(3.9) can be estimated by considering a small time interval centred around $\bar{t}$ and computing the slope of n_e and T_e in that interval for increasing values of the radius. The width of such a time interval must be chosen in order to allow for sufficient precision in the temperature data ($\delta t \geq 15$ms). The resulting power density profile is reported in Fig.3.5 for a typical (^{3}He)D discharge, where the RF power rises from 4.2MW to 8.2MW.

Volume integration in this and other cases indicates that the total power damped on the electrons is about 20% of the total coupled power for a minority concentration of $\eta = n_{He} / n_{e0} \cong 0.10$.

3.5 Neutral Particles Analysis

Even in thermonuclear conditions neutral atoms are continually formed within the plasma, which can therefore travel undisturbed straight across the magnetic field

without colliding. These atoms, called *fast neutrals* to distinguish them from the neutrals which usually surround the plasma at the edge, carry with them precious information about the inner plasma regions.

The proportion of fast neutrals that can reach the plasma edge without colliding depends on the magnitude of the cross sections for the different types of collisions, the most important of which in general are [3.02],

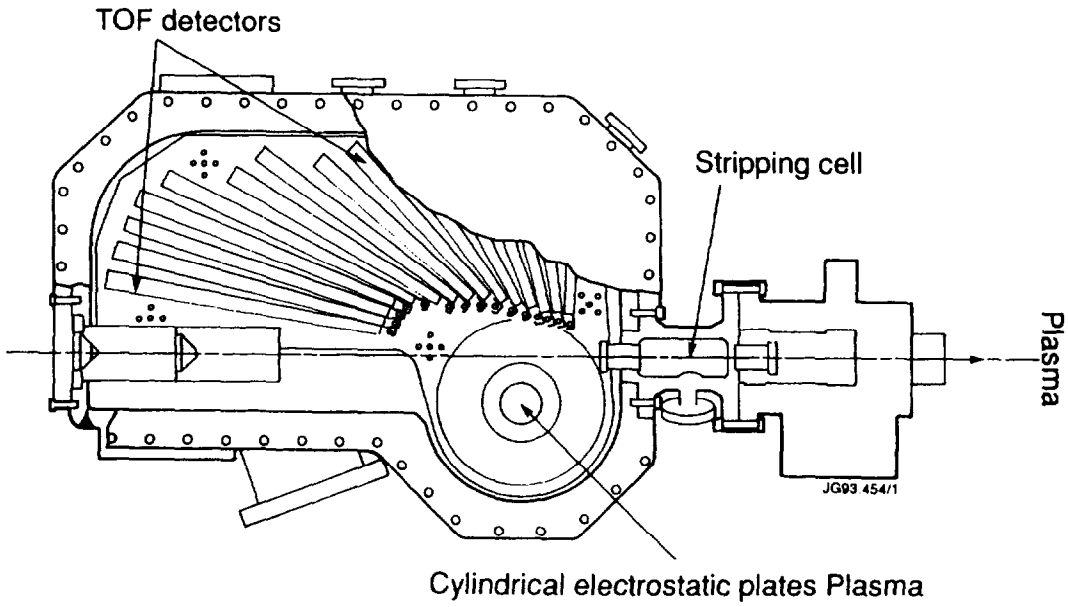

Figure 3.6 Neutral particle analyser. Top view of the time-of-flight analyser [3.10].

1. ionizing collisions with electrons,
2. ionizing collisions with ions,
3. charge-exchange collisions.

The relative importance of these processes depends on the velocity of the neutral. So charge exchange, in which a bound electron is transferred from one atom to an ion, is possible at energies of order of the atomic levels (usually the ground state), and can involve very little translational kinetic energy. Electron and ion impact ionizations,

instead, occur at higher energies, since for these processes to occur the velocity of the electron or ion must be of the same order of that of the atom [2.02].

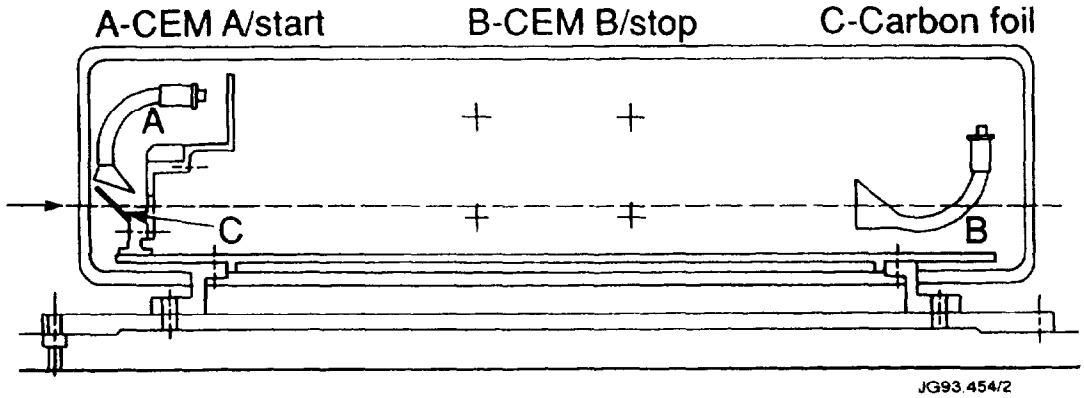

Figure 3.7. Details of the time of flight detector [3.10].

On JET the Neutral Particle Analyser (NPA) (system KR2) is based on the principle of the time of flight of the analyzed particles in order to discriminate between signal and background noise, a problem which heavily affected the old NPA system KR1. The energy range of the analyser is 0-200 keV and it is absolutely calibrated to detect hydrogen, deuterium and helium neutrals [2.10].

The analyser (its layout is reported in Fig.3.6) is located at the bottom of the torus, with its vertical line of sight passing at a major radius R=3.1m on the equatorial plane of the machine [2.10]. The neutrals coming from the plasma are ionized in a gas stripping cell and energy analyzed by means of a cylindrical electrostatic plate system. A set of 15 time of flight detectors collect the ions having a dynamic energy range 1:25 [2.10]. In each detector the ions hit a thin (1 $\mu g/cm^2$) carbon foil where secondary electrons are produced. These are detected by a first channeltron (A in Fig.3.7), thus providing the start trigger for the coincidence, while the ions themselves produce the stop trigger signal in detector B. The start pulse triggers a set of three

programmed time delays (in the range 10-400 ns) at the end of each of which a time gate of pre-programmed length is generated. A coincidence event is then counted if the stop signal occurs during this interval [2.10]. In this way up to three different masses can be counted by each detector.

The NPA system provides measurements of the fluxes of hydrogen, deuterium and helium, from which the relative concentrations n_H/n_D and n_{He}/n_D can be obtained, with an accuracy of ±20%.

3.6 References

1. J. Wesson, *Tokamaks*, Clarendon Press, Oxford UK (1987).

2. I.H. Hutchinson, *Principles of plasma diagnostics*, Cambridge University Press, Cambridge, UK (1987).

3. R. Pozzoli, *Fisica del plasma termonucleare e astrofisico*, CLUED, Milano, Italy (1984).

4. JET Annual Report 1991.

5. M.L. Watkins and M. Keilhacker, Jet Report JET-IR(88)12.

6. C. Gowers, Proc. Course and Workshop on Diagnostics for Contemporary Fusion Experiments, Varenna, Italy (1991), p.63.

7. H. Salzmann et *al.*, Rev. Sci. Instrum. **59** (1988), 1451.

8. R. Kristal, Proc. Course on Diagnostics for Fusion Experiments, Varenna, Italy (1978), p.617.

9. V.P. Bhatnagar et *al.*, Nucl Fusion **33** (1993), 83.

10. S. Corti et *al.*, Proc. Course and Workshop on Diagnostics for Contemporary Fusion Experiments, Varenna, Italy (1991), p.107.

4.0 The Orbit Model

Resonant minority ions during high power ICRF experiments can be accelerated to energies of order of a few MeV and have radii a significant fraction of the radius of the discharge. Therefore when the orbit width is comparable with the width of the RF power density profile spatial corrections for orbits of particles trapped in the toroidal magnetic field become important for the calculation of the energy transfer to the bulk ions [4.01].

The model presented here has been developed by the author in order to introduce the effect of such large orbits in the calculation of the power transferred to electrons through collisions with the minority ions. Compared with its zero-orbit equivalent, the overall effect is to broaden and flatten the electron power deposition profile, thus spreading the input power over a bigger volume. As a consequence heating in the plasma centre may be reduced.

The outline of the Chapter is the following. Firstly, a brief overview of the zero-orbit model as given by Stix [4.02] is presented. Then, the orbit model itself is described. Starting from the guiding centre orbits of resonant particles, the collision frequency is made energy-dependent by averaging it over one closed orbit, the collision operators are re-deduced and the expressions for the electron and ion collisional power transfers are calculated. Lastly, the energy of the fast minority ions is estimated and compared with its experimental counterpart as measured on JET.

4.1 Fast Wave Heating of a Two Component Plasma

This Section is devoted to a detailed overview of an analytical model, due to T.H. Stix [4.02], for fast wave heating of a two component plasma.

In his work Stix derived under certain simplifying assumptions (listed in Section 4.1.1) two forms for the distribution function of the heated minority, necessary to estimate all the quantities relevant to plasma heating. The first

distribution describes minority heating in a plasma where dependence from the pitch-angle can be neglected (Section 4.1.2). The second one is instead valid in high RF power conditions, when the perpendicular energy of the resonant ions is not shared with the parallel degree of freedom and the distribution itself develops a tail in the perpendicular energy direction (Section 4.1.3).

4.1.1 The Fokker-Planck Equation

High power ICRF accelerates the minority ions to energies of up to a few MeV, thus creating a high energy tail. In order to estimate how the minority ion distribution function is affected, it is necessary to consider the Fokker-Planck equation,

$$\frac{\partial f_{m,a}}{\partial t} = Q(f_{m,a}) + C(f_{m,a}), \tag{4.1}$$

where $C(f_{m,a})$ and $Q(f_{m,a})$ are the collisional operator and the RF diffusion operator, respectively. The subscript a in the expression for the distribution function indicates the dependence of f_m on the flux surface radius a (normalized over the major radius). Assuming that the test particles diffuse in a isotropic Maxwellian plasma of ions and electrons, the Coulomb coefficients in $C(f_{m,a})$ as given by Spitzer [4.03] in cartesian coordinates in velocity space are $<\Delta u_{\|}>$, $<(\Delta u_{\perp})^2>$, and $<(\Delta u_{\|})^2>$, where the subscripts $\|$ and $\perp$ are taken with respect to the direction of the test particle velocity **u**. Changing to spherical coordinates in velocity space with unit vectors $(\hat{u},\hat{\theta},\hat{\phi})$, that is setting,

$$< \Delta \mathbf{u} >= \hat{u} < \Delta u_{\|} > \ ,$$
$$< \Delta \mathbf{u} \Delta \mathbf{u} >= \hat{u}\hat{u} < (\Delta u_{\|})^2 > + (\hat{\theta}\hat{\theta} + \hat{\phi}\hat{\phi}) < (\Delta u_{\perp})^2 / 2 > \ ,$$

the collision operator reads,

$$C(f_{m,a}) = -\frac{1}{u^2}\frac{\partial}{\partial u}\left[u^2\left(< \Delta u_{\|} > + \frac{1}{2u} < (\Delta u_{\perp})^2 >\right) f_{m,a}\right] + \\ + \frac{1}{2u^2}\frac{\partial^2}{\partial u^2}\left[u^2 < (\Delta u_{\|})^2 > f_{m,a}\right] + \frac{1}{4u^2}\frac{\partial}{\partial \mu}(1-\mu^2)\frac{\partial}{\partial \mu}\left(< (\Delta u_{\perp})^2 > f_{m,a}\right), \tag{4.2}$$

with μ cosine of the angle between **u** and the magnetic field **B**. The Coulomb coefficients have a fairly simple expression [4.03],

$$< \Delta u_{\parallel} >= -\sum_{\alpha} C_{\alpha} l_{\alpha}^{2} \left(1 + \frac{m}{m_{\alpha}} \right) G(l_{\alpha} u) \ , \tag{4.3-1}$$

$$< (\Delta u_{\parallel})^{2} >= \sum_{\alpha} \frac{C_{\alpha}}{u} G(l_{\alpha} u) \ , \tag{4.3-2}$$

$$< (\Delta u_{\perp})^{2} >= \sum_{\alpha} \frac{C_{\alpha}}{u} [\Phi(l_{\alpha} u) - G(l_{\alpha} u)] \ , \tag{4.3-3}$$

where

$$C_{\alpha} = (2 n_{\alpha} Z_{\alpha}^{2} Z^{2} e^{4} \ln \Lambda) / (\varepsilon_{0} m^{2}) \ , \quad l_{\alpha}^{2} = m_{\alpha} / (2 k_{B} T_{\alpha}) \ ,$$

$$\Phi(x_{\alpha}) = \frac{2}{\sqrt{\pi}} \int_{0}^{x_{\alpha}} dy e^{-y^{2}} \ , \quad G(x_{\alpha}) = [\Phi(x_{\alpha}) - \Phi'(x_{\alpha})] / (2 x_{\alpha}^{2}).$$

As usual the quantities referred to electrons and cackground ions have been labelled with the subscript α (α=e,i), while the fast ions have no subscript.

Randomization of the phase between minority ion motion and the wave field allows the application of the quasi-linear theory to minority heating [4.04], so that the flux surface averaged diffusion term can be written as,

$$Q(f_{m,a}) = \sum_{l,n} Q_{l,n} \delta[\Omega_{i} - (\omega - k_{\parallel} u_{\parallel}) / l] R_{n}(f_{m,a}) \ . \tag{4.4}$$

Here $Q_{l,n}$ are the coefficients of $u_{\perp}^{2n}$ in the following power series,

$$\sum_{n} Q_{l,n} u_{\perp}^{2n} = \frac{Z^{2} e^{2}}{32 \varepsilon_{0} m_{i}^{2} |l|} \left| E_{x} + i E_{y} \right|^{2} \left| J_{l-1}(k_{\perp} u_{\perp} / \Omega_{i}) \right|^{2} \ ,$$

where $J_{l}(b)$ is the Bessel function of integer order l and argument $b = k_{\perp} u_{\perp} / \Omega_{i}$. The differential operator $R_{n}(f_{m,a})$ instead reads,

$$R_n(f_{m,a}) = (1-\mu^2)^{n+1}\frac{1}{u^2}\frac{\partial}{\partial u}u^{2n+1}\frac{\partial}{\partial u}uf_{m,a} +$$

$$+u^{2n-2}\frac{\partial}{\partial \mu}\mu(1-\mu^2)^{n+1}\frac{\partial}{\partial \mu}\mu f_{m,a} +$$

$$-u^{2n-2}\frac{\partial}{\partial \mu}\mu(1-\mu^2)^{n+1}\frac{\partial}{\partial u}uf_{m,a} +$$

$$-(1-\mu^2)^{n+1}u^{2n-2}\frac{\partial}{\partial \mu}\mu\frac{\partial}{\partial u}uf_{m,a} +$$

$$-2n(1-\mu^2)^{n+1}u^{2n-2}\frac{\partial}{\partial \mu}\mu f_{m,a} .$$

An analytical solution of the Fokker-Planck equation (4.1) cannot in general be found. A number of assumptions must then be introduced in order to simplify Eq.(4.1) and solve it. Depending on the energy range considered, different hypotheses can be introduced and, following Stix, two forms of the distribution function can be found. However some very general approximations can be made:

- the plasma is in steady-state conditions. This allows to find a stationary solution of the equation $\partial f_{m,a} / \partial t = 0$;
- the minority ion-electron collision frequency is independent of the energy of the minority ion. This is equivalent to assuming that the minority ions do not leave the given magnetic flux surface;
- density and temperature profiles are constant on a flux surface, so that the Fokker-Planck equation can be averaged over a magnetic surface, and

$$\frac{1}{2\pi}\int d\theta\, Q_{l,n}(x,y)\delta[\Omega_i - (\omega - k_\parallel u_\parallel)/l] \cong \frac{R}{\pi\Omega_i r|\sin\theta_0|}Q_{l,n}(x_0,|y_0|) , \qquad (4.5)$$

where $\theta_0 = \tan^{-1}|y_0|/x_0$ and (x_0,y_0) are the coordinates in the plasma cross-section where the selected magnetic surface intersects the central ($u_{||}$=0) resonant surface. Other assumptions in obtaining Eq.(4.5) are that the cross-section of the magnetic surface is a circle centred in (x,y)=(0,0), that $f_{m,a}$ is independent of θ, that $Q_{l,n}$ is

symmetric for $y = \pm|y_0|$ and is well approximated over the resonant region by its value at (x_0, y_0) [4.02];

- the test particle velocity is much less than the electron thermal velocity, that is $u \ll (2k_B T_e / m_e)^{1/2}$. In this case the functions $G(x_\alpha)$ and $\Phi(x_\alpha)$ defined earlier can be approximated as follows: for electrons,

$$G(x_e) \cong \kappa x_e, \qquad \Phi(x_e) \cong 3\kappa x_e;$$

for ions,

$$G(x_i) \cong \frac{\kappa x_i}{1+2\kappa x_i^3}, \qquad \Phi(x_i) \cong \kappa x_i \frac{3+2x_i^2}{1+2\kappa x_i^3},$$

where $\kappa = 2/(3\sqrt{\pi})$.

Bearing this in mind, in the following two Sections two solutions of the steady-state Fokker-Planck equation as given by Stix [4.02] are outlined.

4.1.2 The steady-state $f(u)$ solution

The determination of the minority ion velocity distribution function can be further simplified by assuming that the distribution function is symmetric in (u,μ) space. In this case it is convenient to average the steady-state Fokker-Planck equation over the pitch-angle μ to obtain an equation for the new distribution function $f(u) = (1/2)\int d\mu f_{m,a}(\mu, u)$. Note that this is equivalent to expanding $f_{m,a}$ in series of Legendre polynomials and retaining only the lowest order term, independent of μ. Considering also heating at the fundamental ion cyclotron frequency of the minority ions, Eq.(4.1) can then be re-written as follows,

$$0 = \frac{\partial f}{\partial t} \cong \frac{1}{u^2}\frac{\partial}{\partial u}\left[-\alpha u^2 f + \frac{1}{2}\frac{\partial}{\partial u}(u^2 \beta f) + K u^2 \frac{\partial f}{\partial u}\right], \tag{4.6}$$

where,

$$\alpha = < \Delta u_{\parallel} > + < (\Delta u_{\perp})^2 >, \quad \beta = < (\Delta u_{\parallel})^2 >,$$

$$K = \frac{2R}{3\pi\Omega_i r|\sin\theta_0|} Q_{0,1}(x_0, |y_0|) = \frac{\rho_{RF}}{3n_i m_i},$$

with ρ_{RF} input power density (coupled to the minority ions). The solution then reads,

$$\ln[f(u)/f_0] = -\int_0^u du \frac{-2\alpha u^2 + d(\beta u^2)/du}{\beta u^2 + 2Ku^2}, \tag{4.7}$$

where $f_0 = \int_0^\infty duu^2 f(u)$ is the normalization constant. Substituting the correct expressions for the coefficients α and β the integral in Eq.(4.7) can be carried out to obtain,

$$\ln[f(E)/f_0] = -\frac{E}{k_B T_e(1+\xi)}\left[1 + \frac{R_i(T_e - T_i + \xi T_e)}{T_i(1+R_i+\xi)} H(E/E_{i)}\right], \tag{4.8}$$

where $E=mu^2/2$, $R_i = n_i Z_i^2 l_i / n_e l_e$, $\xi = 2K/(\kappa C_e l_e)$ and,

$$E_i(\xi) = \frac{mk_B T_i}{m_i}\left[\frac{1+R_i+\xi}{2\kappa(1+\xi)}\right]^{2/3},$$

$$H(x) = \frac{1}{x}\int_0^x \frac{dy}{1+y^{3/2}}.$$

For most pratical purposes, it is useful to consider an effective temperature of the minority distribution called the *tail temperature* and defined as,

$$T_t = -\left(\frac{\partial \ln f}{\partial E}\right)^{-1}. \tag{4.9}$$

Using Eq.(4.8) the tail temperature reads,

$$T_t = T_e(1+\xi)\left[1+\frac{R_i(T_e - T_i + \xi T_e)}{T_i(1+R_i+\xi)}\frac{1}{1+(E/E_i)^{3/2}}\right]^{-1} . \qquad (4.10)$$

From Eq.(4.10) it can be seen that for ξ=0 (no heating) $T_t \cong T_i$, that is the minority distribution is Maxwellian with a temperature close to that of the background ions. For ξ>0 instead in the high energy limit ($E \gg E_i$) Eq.(4.10) can be written as,

$$T_t \cong T_e(1+\xi) . \qquad (4.11)$$

Plots of the distribution function against energy at different plasma radii is shown in Fig.4.1 for a JET discharge.

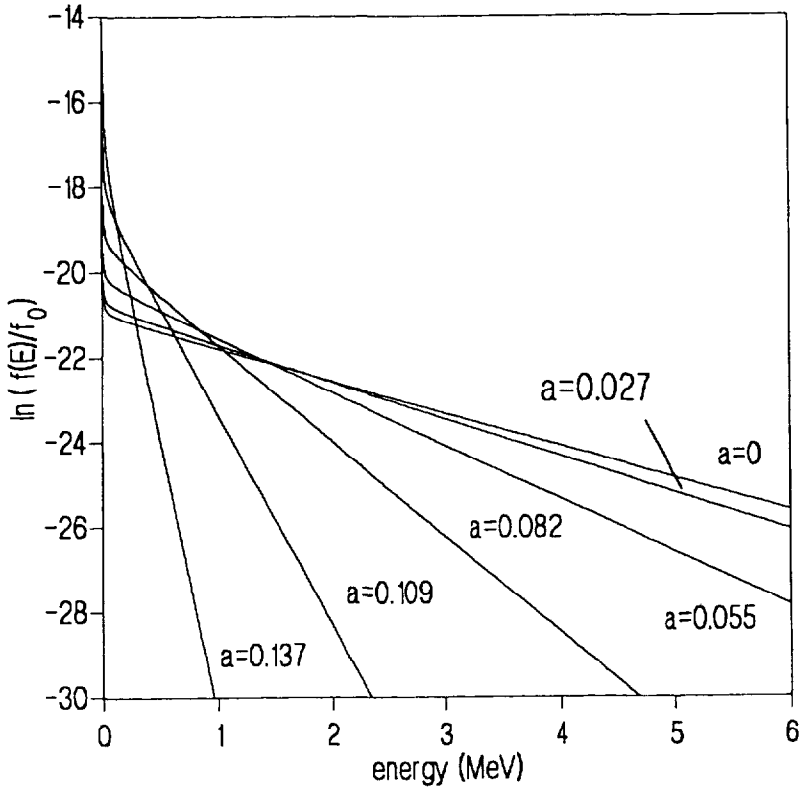

Figure 4.1 **Stix distribution functions** for increasing positions $a=a'/R_0$ from the plasma centre. The picture refers to an (H)D JET discharge, with plasma parameters I_p=3MA, B_0=3T, $n_e(0)$=3.88×10^{19} m^{-3}, $T_e(0)$=9.23 keV and 8.5MW of on-axis ICRF.

4.1.3 The steady-state $f(u_\perp)$ solution

In high power experiments the resonant ions often acquire energies which are in general much higher than the critical energy [4.02],

$$E_c = 14.8 k_B T_e \left[\frac{A^{3/2}}{n_e} \sum_i \frac{n_i Z_i^2}{A_i} \right]^{2/3}, \tag{4.12}$$

at which electrons and background ions experience the same collision rate with the minority ions. In this energy range, where minority ion-electron collisions dominate, the main Coulomb process is electron drag, which does not introduce appreciable pitch-angle scattering. It is important to note that the perpendicular energy acquired during cyclotron damping is not shared with the parallel degree of freedom. A useful description of the strongly anisotropic distribution function can then be obtained by changing to $(u_{||}, u_\perp)$ variables in velocity space. Remembering that the plasma is in steady-state conditions, the Fokker-Planck equation thus transformed reads [4.02],

$$\begin{aligned} 0 = \frac{\partial}{\partial t} f_{m,a}(u_\parallel, u_\perp, t) = & -\frac{1}{u}\left(u_\perp \frac{\partial}{\partial u_\perp} + u_\parallel \frac{\partial}{\partial u_\parallel} + 2 \right)(\alpha f_{m,a}) \\ & + \frac{1}{2u^2}\left(u_\perp^2 \frac{\partial^2}{\partial u_\perp^2} + 2u_{\perp\parallel} u_\parallel \frac{\partial^2}{\partial u_\perp \partial u_\parallel} + u_\parallel^2 \frac{\partial^2}{\partial u_\parallel^2} + 4u_\perp \frac{\partial}{\partial u_\perp} + 4u_\parallel \frac{\partial}{\partial u_\parallel} + 2 \right)(\beta f_{m,a}) \\ & + \frac{1}{4u^2}\left(u_\parallel^2 \frac{\partial^2}{\partial u_\perp^2} - 2u_\parallel u_\perp \frac{\partial^2}{\partial u_\perp \partial u_\parallel} + u_\perp^2 \frac{\partial^2}{\partial u_\parallel^2} + \frac{u_\parallel^2 - u_\perp^2}{u_\perp^2} \frac{\partial}{\partial u_\perp} - 2u_\parallel \frac{\partial}{\partial u_\parallel} \right)(\gamma f_{m,a}) \\ & + \sum_{l,n} Q_{l,n} \delta[\Omega_i - (\omega - k_\parallel u_\parallel)/l] \frac{1}{u_\perp} \frac{\partial}{\partial u_\perp} u_\perp^{2l+1} \frac{\partial f_{m,a}}{\partial u_\perp}, \end{aligned} \tag{4.13}$$

where $u = (u_\parallel^2 + u_\perp^2)^{1/2}$ and $\gamma = <(\Delta u_\perp)^2>$, while α, β and $Q_{n,l}$ are unchanged. As in Section 4.1.2, some further simplifying assumptions are introduced;

- suppose that $<u_\perp^2> \gg <u_\parallel^2>$, so that terms can be ordered according to

  $u_\perp \gg |u_\parallel|$,
  $u_\perp \approx u$,
  $u_\parallel (\partial / \partial u_\parallel) \approx u_\perp (\partial / \partial u_\perp)$;

- average out the parallel degree of freedom in the distribution function by defining,

$$f(u_\perp,t)=\int_{-\infty}^{+\infty}du_\parallel f_{m,a}(u_\parallel,u_\perp,t)\ .$$

This can be achieved by integrating Eq.(4.13) over the parallel velocity.

After some further algebraic manipulations, the new 1D steady-state Fokker-Planck equation reads,

$$\begin{aligned}0=\frac{\partial}{\partial t}f(u_\perp,t)\cong-\frac{1}{u_\perp}\frac{\partial}{\partial u_\perp}(\alpha u_\perp f)+\frac{1}{2u_\perp}\frac{\partial^2}{\partial u_\perp^2}(\beta u_\perp f)\\ +\frac{1}{4u_\perp}\frac{\partial}{\partial u_\perp}(\gamma f)+\frac{3K}{2u_\perp}\frac{\partial}{\partial u_\perp}u_\perp\frac{\partial f}{\partial u_\perp}\ ,\end{aligned}\tag{4.14}$$

the solution of which can now be readily found,

$$\ln[f(u_\perp)/f_0]=-\int_0^{u_\perp}du_\perp\frac{-4\alpha u_\perp+2\partial(\beta u_\perp)/\partial u_\perp+\gamma}{2\beta u_\perp+6Ku_\perp}\ ,\tag{4.15}$$

where this time $f_0=\int_0^\infty du_\perp u_\perp f(u_\perp)$. If $f(u_\perp)$ is compared with the expression for $f(u)$, it can be seen that the only difference is the pitch-angle scattering coefficient γ present in Eq.(4.15) and absent in Eq.(4.7). The presence of γ, like dispersion and drag, reduces $u_\perp$ when $u_\perp^2 \gg <u_\parallel^2>$.

Following the same steps that led to Eq.(4.8), the integration in Eq.(4.15) can be carried out and terms can be rearranged to obtain f in terms of the perpendicular energy $E_\perp=mu_\perp^2/2$,

$$\ln[f(E_\perp)/f(0)]=-\frac{2E_\perp}{k_BT_e(2+3\xi)}\left[1+\frac{R_i[(2A+A_i)(2+3\xi)T_e-4AT_i]}{2AT_i(2+2R_i+3\xi)}H(E_\perp/E_i)\right]\tag{4.16}$$

where now,

$$E_i=\frac{Ak_BT_i}{A_i}\left[\frac{2+2R_i+3\xi}{2\kappa(2+3\xi)}\right]^{2/3}\ .$$

In this approximation a useful estimate of the perpendicular energy of the resonant ions is given by the tail temperature. At the lowest order in $E_\perp$ it reads,

$$T_t \cong T_e(1+\frac{3}{2}\xi) \ . \tag{4.17}$$

It should be remembered that Eq.(4.16) holds only in that energy range when $f_{m,a}(\boldsymbol{u},t)$ is strongly anisotropic. A rough estimate of the lower boundary of validity is given by the energy at which the pitch-angle term in Eq.(4.15) is comparable with the electron drag term, that is when [4.02],

$$E_\perp \cong 14.8 k_B T_e \left[\frac{A^{1/2}}{2n_e}\sum_i n_i Z_i^2\right]^{2/3} \ .$$

4.2 The Orbit Model

The usual calculations of ICRF minority heating in a two-component plasma use one of the two forms of the Stix distribution function as seen in Section 4.1 for the minority ions, which are assumed to have zero orbit width and therefore remain on a given flux surface. On each flux surface the plasma parameters are assumed to be constant so that, in particular, the minority ion-electron collision frequency at that flux surface radius is the same for all ions in the distribution. Collisional power transfer to the electrons and background ions is calculated by applying the appropriate collision operators to the distribution and integrating over velocity space. Radial profiles are then obtained by calculating the Stix distribution and power transfer for each flux surface. The flux surface averaged power density P_{RF} entering this calculation is often assumed to have a Gaussian radial dependence which simulates direct electron heating profiles obtained from modulation experiments (e.g. $P_{RF} = P_0 e^{-r^2/w^2}$ for on-axis heating, with $w \cong 0.3$m for JET discharges, see Chapter 3).

The present modifications to the original model can be described with reference to Fig.4.2, which shows typical trapped ion orbits. As in the Stix model, Larmor radius effects are neglected in the RF diffusion coefficient (which is equivalent to taking $J_0(0) \approx 1$). It is also assumed that the dominant effect of the orbit-induced departure from the flux surface of (normalized) radius a is through the minority ion-electron collision frequency ν_{ie} on the following basis. The orbit-induced departures from the flux surface of radius a allow the minority ions to reach both the

cooler outer and the hotter inner regions of the plasma, which affects ν_{ie} through its dependence on T_e and n_e, since $\nu_{ie} \propto n_e T_e^{-3/2}$. The effect is greatest for the most energetic ions. In JET significant departures occur for energies above the critical energy (usually 100-200 keV) and therefore for ions which slow down mainly by collision with electrons. Usually the low energy ions which slow down with the background ions have negligible orbit sizes.

Thus the distribution function f_a is calculated using a collision frequency ν_{ie} which is averaged over each minority ion orbit and, by virtue of this process, depends on the minority ion energy. The result is an increase in ν_{ie} and a reduction in f_a at high energies (see Fig.4.3). The new calculations assume the same Gaussian profile for the absorbed power density, as in the old model.

The power deposition profiles are now more complicated to obtain since the orbits allow ions with a given energy in the distribution function to heat a range of flux surfaces and this range varies with the ion energy itself. Thus, each distribution f_a produces a contribution to the whole heating profile rather than just on a single flux surface as in the zero orbit width model. This contribution is obtained from the local heating rate (local collision frequency) as the ion passes through each flux surface and from the fraction of time spent on that flux surface. The aggregate electron and ion heating profiles are then found by integrating over the variable a.

Since the distribution function f_a is determined using the orbit averaged collision frequency $<\nu_{ie}>$and the power transfers use the local values of ν_{ie}, a question of self-consistency arises. This self-consistency is established analytically. Numerically the sum of the ion and electron heating rates is found to be within ±5% of the input power.

4.2.1 Guiding Centre Orbits

The geometry used here is based on the simplified model for the magnetic field of the tokamak in polar coordinates(ε,θ).Here ε is the plasma minor radius normalized to the position R_0 of the magnetic axis, while θ is the angle in the poloidal plane. The field is given by [4.05],

$$B(\varepsilon,\theta) = \frac{B_0}{1+\varepsilon\cos\theta}\,, \tag{4.18}$$

where B_0 is the magnetic field at R_0.From the three invariants of motion (particle energy, magnetic moment and the longitudinal invariant) an equation for the guiding centre orbit can be found [4.05],

$$(\psi_1^2+\varepsilon\cos\theta)(1+\varepsilon\cos\theta)^2=[\psi_1+\alpha(\varepsilon^2-a^2)]^2\,, \tag{4.19}$$

where the pitch-angle $\psi_1=(v_\parallel/v_\perp)_1$, ratio of the parallel to perpendicular velocity, is defined at the reference position ($\varepsilon=a,\theta=\pi/2$). In Eq.(4.19) $\alpha=R_0/(2\rho q)$, where $\rho=(v_\perp/\Omega)_{\pi/2}$ is the ion Larmor radius in the total magnetic field, and $\Omega=ZeB/M$ is the gyrofrequency of the heated ion of mass $M=Am_p$ and charge $+Ze$. The safety factor $q=rB_\phi/(R_0B_\theta)$ in the plasma centre is assumed constant and of order of unity.

The orbit equation can be solved analytically for the poloidal angle θ in the interval between the minimum and maximum radii of the particle orbit, $\varepsilon_{min}\le\varepsilon\le\varepsilon_{max}$. In fact Eq.(4.19) can be rewritten as a cubic in the variable $x=\cos\theta$,

$$x^3+a_1x^2+a_2x+a_3=0\,, \tag{4.20}$$

with coefficients,

$$a_1=\frac{2+\psi_1^2}{\varepsilon}\,,\quad a_2=\frac{1+2\psi_1^2}{\varepsilon^2}\,,\quad a_3=-\frac{\alpha}{\varepsilon^3}(\varepsilon^2-a^2)[\alpha(\varepsilon^2-a^2)+2\psi_1]\,.$$

The orbit solution then reads,

$$\theta=\cos^{-1}[S+T-a_1/3]\,, \tag{4.21}$$

where $S=[R+\sqrt{D}]^{1/3}$, $T=[R-\sqrt{D}]^{1/3}$, $D=Q^3+R^2>0$ is the discriminant of the cubic,and $Q=a_2/3-(a_1/3)^2$, $R=a_1a_2/6-a_3/2-(a_1/3)^3$. A set of typical calculated guding centre orbits of trapped particles is shown In Fig.4.2, where both low energy bananas and high energy D-shaped orbits are present. Note that the latter type of orbit streches out as far as half the minor radius, where the plasma is cool and highly collisional.

4.2.2 Minority ion-electron collision frequency

An important parameter in the present model is the critical energy at which the minority ions experience equal magnitudes of ion-ion and ion-electron friction [4.02] and given by Eq.(4.12). In the limit of high particle energy ($E \gg E_c$) and when the

minority concentration is of order of a few percent, the fast ions lose energy mainly through ion-electron collisions, characterized by the energy collision frequency,

$$\nu_{ie} = \tau_E^{-1} = \frac{2e^4 Z^2 n_e \ln\Lambda}{3\pi^{3/2}\varepsilon_0^2 v_{the}^3 m_e M}, \tag{4.22}$$

where τ_E is the energy slowing-down time, and $\ln\Lambda$ is the Coulomb logarithm. However, to take into account correctly the change in collisionality when the minority ions travel along the D-shaped orbits, it is necessary to consider also an energy dependent ion-electron collision frequency averaged over one closed orbit,

$$<\nu_{ie}>(E) = \frac{\oint d\varepsilon\, \nu_{ie}(\varepsilon, E)}{\oint d\varepsilon}. \tag{4.23}$$

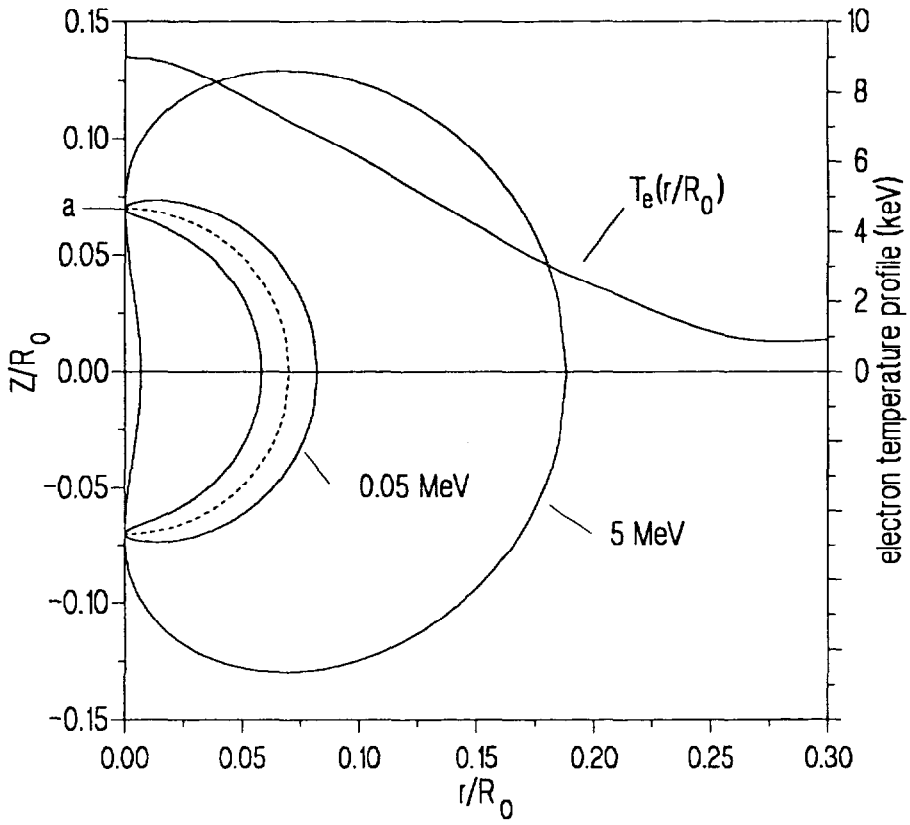

Figure 4.2 **Guiding centre orbits.** Plot of the analytical solution of the guiding centre equation of motion for two different energies of the resonant ions. The circular birth flux surface of radius a=0.07 is indicated by the dashed line. Superimposed is the electron temperature profile. The test particle parameters are ψ_1=0, a=0.07 in a magnetic field B_0=3T.

In the following both forms of collision frequency (4.22) and (4.23) will be used. To avoid possible confusions the brackets <...> indicating the orbit average will always be written explicitely.

4.2.3 The Collision Operators

The orbit results can now be applied to the kinetic theory. Consider the Fokker-Planck equation in the (v,μ) space, where $v=|\mathbf{v}|$ and μ is as before the cosine of the angle between **v** and the magnetic field **B**, in the form,

$$\frac{\partial f_{m,a}}{\partial t}=\left(\frac{\partial f_{m,a}}{\partial t}\right)_C+\left(\frac{\partial f_{m,a}}{\partial t}\right)_{RF}, \tag{4.24}$$

and $f_{m,a}=f_m(v,\mu,t;a)$ is the distribution function of the minority species, dependent also on the flux surface radius a. The first term on the right-hand side of Eq.(4.24) is the collision operator, while the second term accounts for the variations of the distribution function due to the presence of fast wave heating at the fundamental minority ion cyclotron frequency. In order to solve Eq.(4.24), the following assumptions are made:

1. the plasma is in steady-state conditions. A solution of the equation $\partial f_{m,a}/\partial t=0$ can then be found without losing in generality, since RF heated discharges on JET easily reach steady-state regimes;

2. the distribution function is symmetric in (v,μ) space. The steady-state Fokker-Planck equation can then be averaged over the pitch-angle μ to obtain an equation for the new distribution function,

$$f_a(v,t)=f_m(v,t;a)=\frac{1}{2}\int_0^1 d\mu f_{m,a}(v,\mu,t)\ .$$

   This approximation does not introduce significant differences with respect to the two-dimensional solution, as Anderson et *al.* [4.06] have shown;

3. the minority ion velocity is much less than the electron thermal velocity, that is $v \ll (2k_B T_e/m_e)^{1/2}$.

Using the former assumptions the collision operator can now be written as,

$$\left(\frac{\partial f_a}{\partial t}\right)_C = \frac{1}{v^2}\frac{d}{dv}\left[-\alpha v^2 f_a + \frac{1}{2}\frac{d}{dv}(\beta v^2 f_a)\right], \tag{4.25}$$

where α, β formally are the Coulomb diffusion coefficients as given in [4.03], but containing both ν_{ie} and $<\nu_{ie}>$. With some mathematical rearrangements the contributions from ion-electron and ion-ion collisions can be separated, and the collision operator can be written as the sum of two terms, namely,

$$\left(\frac{\partial f_a}{\partial t}\right)_{Ce} = \frac{\nu_{ie}}{2v^2}\frac{d}{dv}\left[\left(1+\frac{1}{\nu_{ie}}\frac{2k_BT_e}{Mv}\frac{d}{dv}<\nu_{ie}>\right)v^3 f_a + \frac{k_BT_e}{M}v^2\frac{df_a}{dv}\right], \tag{4.26-1}$$

$$\left(\frac{\partial f_a}{\partial t}\right)_{Ci} = \kappa v_\alpha^3 \nu_{ie}\frac{1}{v^2}\frac{d}{dv}\left[\frac{l_i v}{1+2\kappa(l_i v)^3}\left(l_i v f_a + l_i\frac{k_BT_i}{M}\frac{df_a}{dv}\right)\right]. \tag{4.26-2}$$

In Eqs.(4.26) v_α is such that $Mv_\alpha^2/2 = E_c$, while $l_i^2 = m_i/(2k_BT_i)$. The RF heating term remains quite simple and reads,

$$\left(\frac{\partial f_a}{\partial t}\right)_{RF} = \frac{K}{v^2}\frac{d}{dv}v^2\frac{df_a}{dv}, \tag{4.27}$$

with $K = \rho_{RF}/(3m_in_i)$. Here ρ_{RF} is the coupled RF power density as defined below in Section 4.2.5. As in the previous Section, the subscript i refers to the background ions with mass $m_i = A_i m_p$ and number density n_i.

4.2.4 The distribution function

With the assumptions listed above, the self-consistent steady-state solution of the Fokker-Planck equation (4.24) reads,

$$\ln[f_a(E)/f_0] = -\int_0^E \frac{dE}{k_BT_e(1+\xi)}\frac{1}{1+(E/E_i)^{3/2}}\times \tag{4.28}$$
$$\times\left[1+\frac{R_i(T_e-T_i+\xi T_e)}{T_i(1+\xi+R_i)}+\frac{k_BT_E}{<\nu_{ie}>}\frac{d}{dE}<\nu_{ie}>\left(\frac{1+\xi}{1+\xi+R_i}+(E/E_i)^{3/2}\right)\right].$$

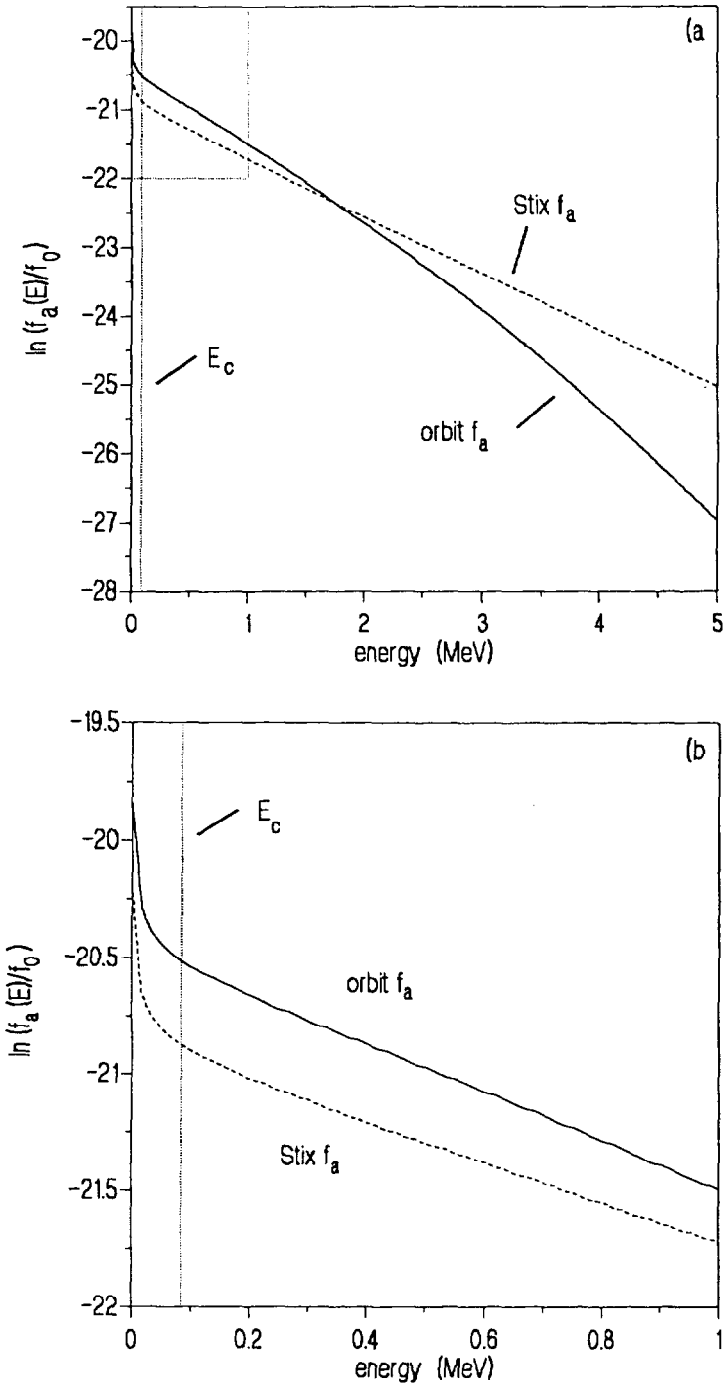

Figure 4.3 **Minority distribution function**. Comparison of the self-consistent steady-state minority distribution function Eq.(4.28) (continuous curve) with the correspondent one from the Stix model, given by Eq.(4.8) (dashed curve), for the normalized flux surface radius a=0.02. At large values of the particle energy the deviation from the linear behaviour is apparent (Figure 4.3a). This led in the past to overestimate the number of high energy resonant particles. Figure 4.3b shows instead that in the low energy range, where ion-ion collisions dominate (in this case E_c =8.5 keV) the two models are qualitatively the same.

Here $f_0 = \int_0^\infty dE\sqrt{E} f_a(E)$ is the normalization constant, $R = \nu_{ii} T_i / (<\nu_{ie}> T_e)$, with ν_{ii} ion-ion collision frequency (constant with respect to E) and T_i temperature of the background ions, $\xi = KM / (k_B T_e <\nu_{ie}>)$, and,

$$E_i = \frac{A k_B T_i}{A_i}\left[\frac{1+R_i+\xi}{2\kappa(1+\xi)}\right]^{2/3}.$$

In Eq.(4.28) terms can be recognized which were already present in the Stix formulation given by Eq.(4.8), although in a very simplified way. In fact the dependence of the collision frequency on the energy now makes it impossible to carry out analytically the integral in Eq.(4.28). The behaviour of the distribution function with energy for one heating radius a is compared in Fig.4.3 with the Stix counterpart for a typical H minority discharge on JET. Its negative curvature at high energy values, absent in the Stix model, is due to the increased collision rate that the high energy heated ions experience.

4.2.5 Collisional power transfer

In earlier JET experiments [4.07,4.08] the temporal response of the plasma to square-wave pulses of RF heating power has been measured. Results show that, for centrally heated H and ^{3}He minority plasmas, the direct electron heating deposition profile can be approximated by a Gaussian function with characteristic e-folding radius w=0.3±0.05 m (see also Chapter 3). It is here assumed that the same profile can be attributed to the left-handed circularly polarized component of the electric field intensity $|E_+|^2$ which drives minority heating.In particular the RF power density ρ_{RF} for on-axis heating is taken to be,

$$\rho_{RF}(a) = \frac{P_{RF}}{2\pi^2 w^2 R_0} e^{-(aR_0)^2/w^2}, \qquad (4.29)$$

where P_{RF} is the total power coupled to the minority ions.

Using the quantities introduced earlier, the electron and ion power density deposition profiles can now be derived. The explicit derivation of the electron heating term is as follows.

We will assume the input power absorption per unit volume as in Eq.(4.29), and calculate the power density transferred from the minority ions to the electrons on the flux surface of non-normalized radius $r=\varepsilon R_0$.The energy lost on each orbit bounce at the position $a'=aR_0$ by the fast ion in the time interval dt is $\delta E=Edt/\tau_E(r)$. The orbit average power loss at r then reads,

$$\delta P=\frac{E}{\tau_E}\frac{dr}{v_r}\frac{1}{\tau_b},$$

where τ_b is the bounce time, and $dr=dtv_r$. The radial velocity v_r can be written as,

$$v_r=\frac{v_0^2}{\Omega_i R_0}\frac{0.5+(r/R_0)\cos\theta}{1+(r/R_0)\cos\theta},$$

with $v_0^2=2E/M$. Thus for one orbit the power deposition profile reads,

$$P_e(E,a',r)=\frac{\delta P}{2\pi R_0\times 2\pi r dr}=\frac{1}{4\pi^2 R_0}\frac{E}{\tau_b v_r}\frac{1}{r\tau_E}.$$

Now define an effective minority density $n_{\min}$ in terms of the number N_a of fast ions passing through da' as $N_a=n_{\min}\times 2\pi R_0\times 2\pi a' da'$. Using Eq.(4.26-1) for the electron collision operator, and changing to normalized variables (ε,a) the electron power density deposition profile can be written as,

$$P_e(\varepsilon)=\frac{n_{\min}}{\varepsilon f_0}\int_0^{a_0/R_0}da\,a\int_{E_{\min}}^{E_{\max}}dE\frac{\sqrt{E}}{v_r\tau_b}\left[\nu_{ie}(E-\frac{3}{2}k_BT_e)+E\frac{d}{dE}(k_BT_e<\nu_{ie}>)\right]f_a(E)$$

.(4.30-1)

To estimate the ion heating term there is no need to consider orbit effects explicitely, since the fast ions collide with the background ions at low energies, typically of order of E_c. A straightforward calculation then leads to the following expression,

$$P_i(\varepsilon\cong a)=n_{\min}E_c^{3/2}\nu_{ie}\frac{\kappa}{f_0}\int_0^{E_{\max}}dE\frac{(E/E_t)^{1/2}f_a(E)}{1+2\kappa(E/E_t)^{3/2}}\left[\frac{2E}{E_t}-\frac{3A_i/A}{1+2\kappa(E/E_t)^{3/2}}\right],\quad(4.30\text{-}2)$$

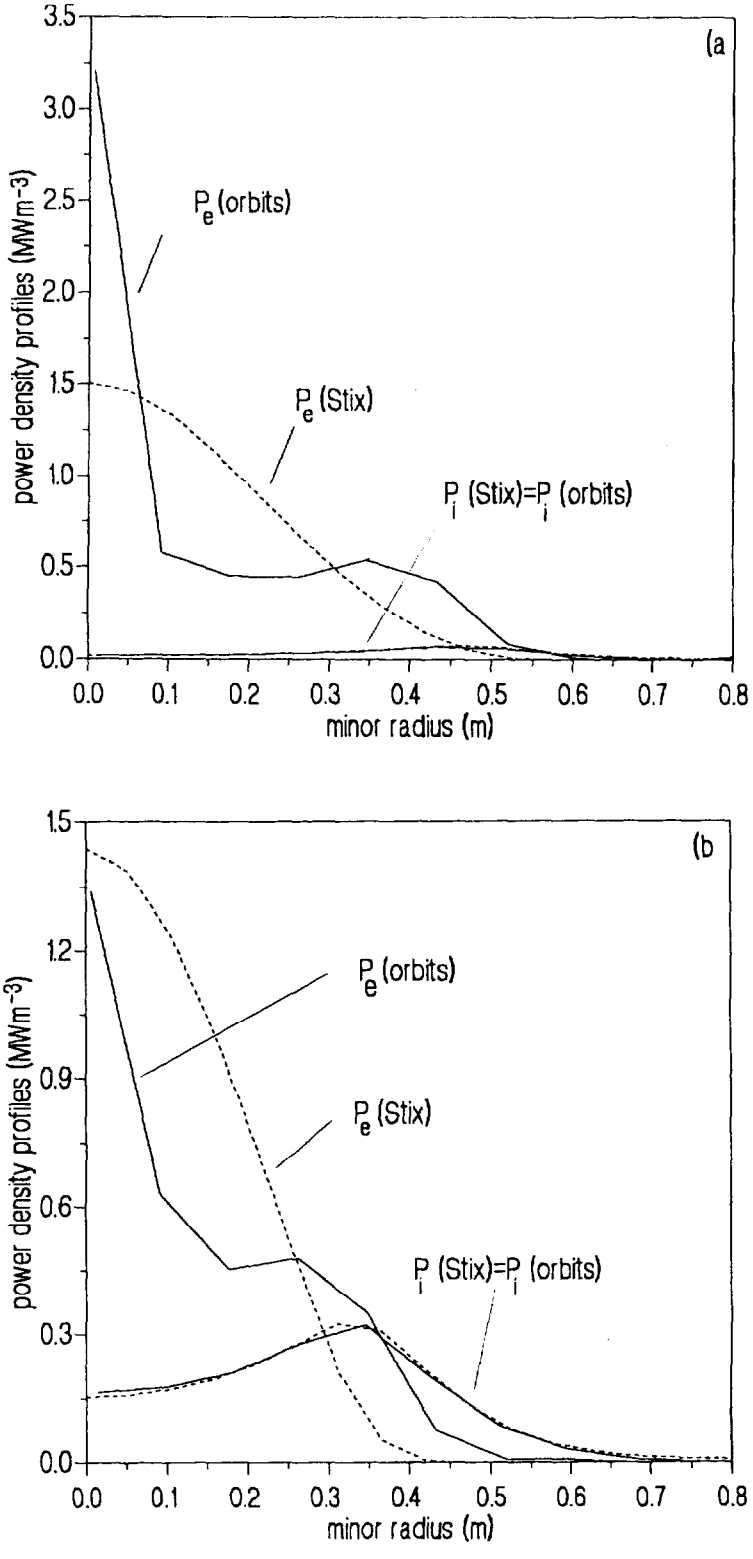

Figure 4.4 Power deposition profiles. Radial electron and ion heating profiles calculated with orbits (continuous curves) and without (dashed curves) for two JET discharges with H (Figure 4.4a) and ^{3}He (Figure 4.4b) minorities, with concentrations equal to 5% and 8%, respectively.

where $E_t=Ak_BT_f/A_i$. In Eq.(4.30-1) the lower limit of integration E_{min} is calculated at each flux surface radius ε (also equal to the fast ion orbit radial position) and is such that the fast ion with energy E_{min} just touches this flux surface at the midplane. The upper limit E_{max} is instead given by the condition that the maximum radius of the fast ion orbit just touches the wall of the vacuum vessel ($\varepsilon=a_0/R_0$ at the mid-plane). The particles which strike the wall are lost and therefore not considered.

Typical calculations of ion and electron power deposition profiles are shown in Fig.4.4, together with their zero-orbit counterparts, for H and ^{3}He minorities. It can be seen that in both cases there is a big difference between the ion and electron heating profiles, mainly due to the different role that orbits have in the collisional power transfers at the energies involved. In fact the electron radial heating profile is determined mainly by collision of the electrons with the fast ions, with energies well above the critical energy E_c. As already noted, at such energies the fast ion orbits are mainly D-shaped (see Fig.4.2), with (non-dimensional) finite width equal to $v_r\tau_b/R_0$. On the other hand, due to the different ratio m_f/M, the background ions collide with the heated species only when their energy is of order of E_c or lower. In this case the banana orbits have width of order of one centimeter or less. It is thus clear why in the second case the orbit effects can be completely negligible in Eq.(4.30-2), with the possible exception of the innermost plasma region. This can be seen from another point of view by comparing Eq.(4.28) with the Stix solution when $E\geq E_c$, as in Fig.4.3b: the two distribution functions have the same slope in this energy range.

By a further integration over the minor radius ε the total power transferred to electrons and background ions through collisions with the fast ions can be estimated. This simple calculation is an important numerical check for the self-consistency of the model, because the sum of these two quantities must equal the total power coupled to the minority.

On the basis of the present model a numerical code, called PHANTOM, has been developed. It calculates both electron and ion collisional power deposition profiles, as well as the fast ion energy content (see the next Section). The check on the total power is carried out routinely, and the error is estimated to be within ±5% of the input power in the worst cases. For those interested, a brief description of the PHANTOM code is reported in Appendix B.

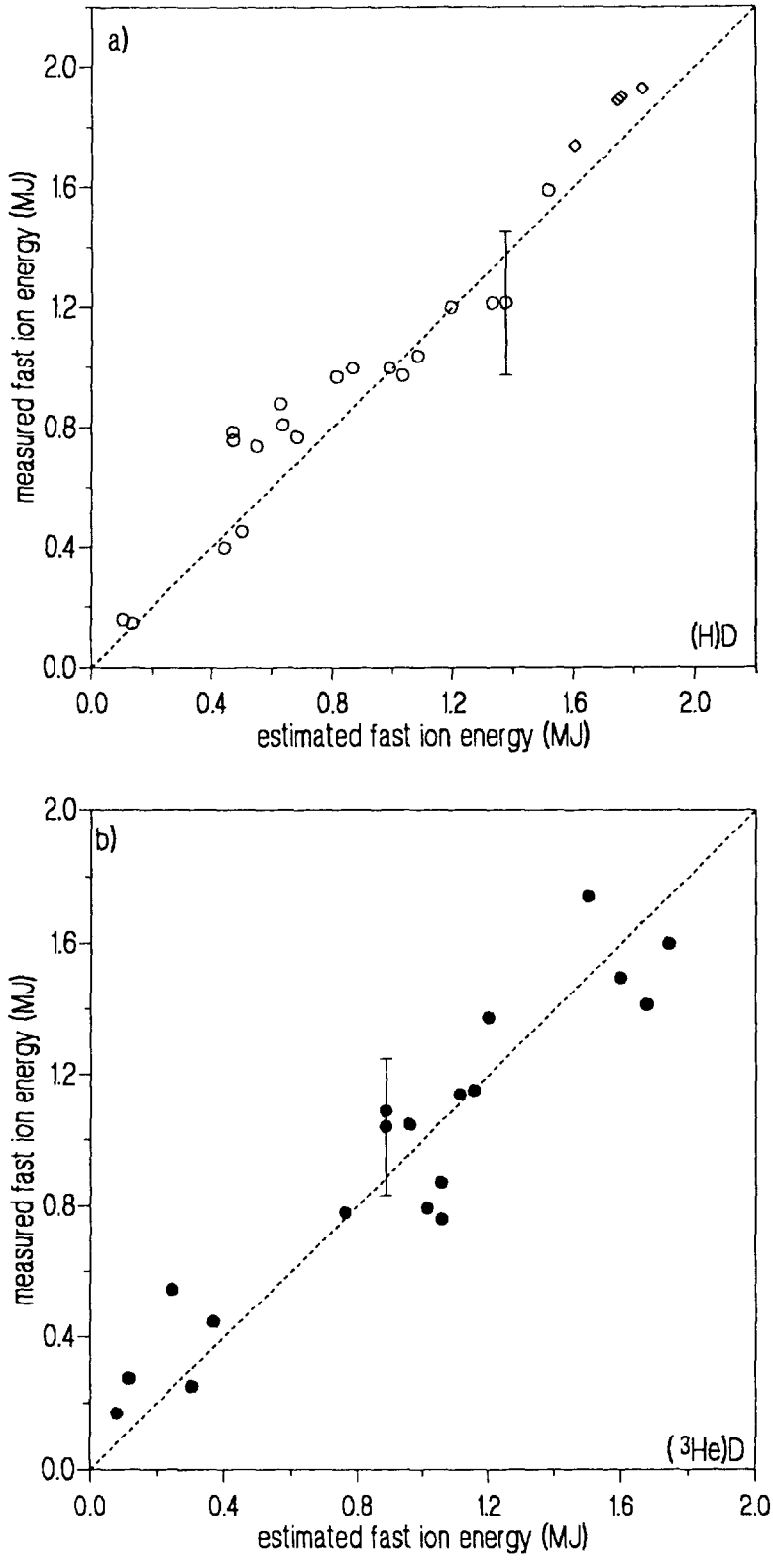

Figure 4.5 **Fast ion energy.** The measured fast ion energy W_f is compared with the average perpendicular energy in anisotropic regime W_c as calculated with the PHANTOM code for H (Fig.4.5a) and ^{3}He (Figure 4.5b) minorities. The error bars refer to two reference discharges, labelled A and B, used to check the sensitivity of W_c to the minority concentration and reported in Fig.4.6.

4.2.6 The fast ion energy content

Unfortunately, there is no reliable way to measure on JET the radial profiles of the collisional power transfer to electrons and background ions during minority ICRF experiments. Any comparison of the present model with the experiment must therefore rely on measurable quantities related to the heating profiles. One such measurement is the fast ion energy content W_f, already introduced in Chapter 3 as the energy of the heated (fast minority ions in excess of the isotropic component.

Theoretically the fast ion energy content can be calculated by estimating the average energy of the minority ions in the strongly anisotropic regime, when $E \approx E_\perp \gg E_c$. To this end, orbit effects have been incorporated into the Stix distribution function $f_a(E_\perp)$ in the strongly anisotropic regime [4.02] in a way similar to that described in Section 4.2.2. A good estimate of the average perpendicular energy characterizing the minority species can therefore be obtained by estimating,

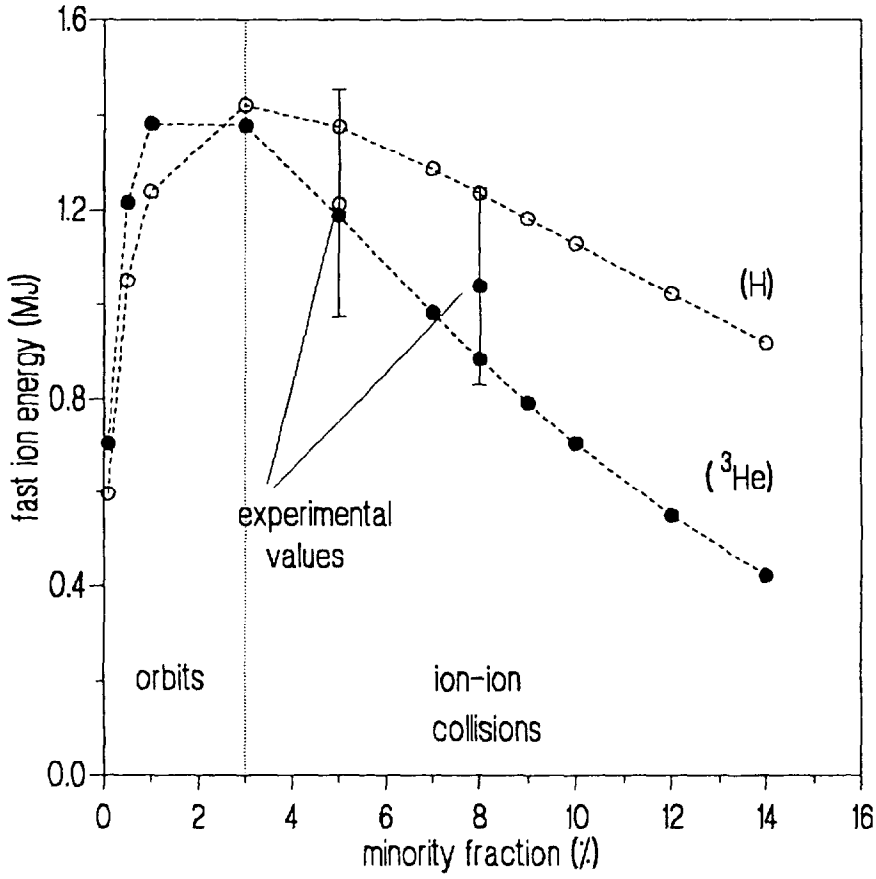

Figure 4.6 **Sensitivity test.** Sensitivity of the calculated fast ion energy W_c to variations in the minority concentration η for two selected discharges from the database of Fig.4.5 with H and ^{3}He minority, the heating profiles of which have been reported in Fig.4.4.

$$W_c = 4\pi^2 R_0 n_{\min} \int_0^{a_0/R_0} da\, a \frac{\int_{E_c}^{E_{\max}} dE_\perp f_a(E_\perp) E_\perp}{\int_0^\infty dE_\perp f_a(E_\perp)} . \qquad (4.31)$$

Eq.(4.31) is by definition greater than zero only in those regions where the tail temperature T_t (defined by Eq.(4.17)) is greater than E_c.

In order to check the validity of Eq.(4.31), two series of JET (H)D and (^{3}He)D discharges have been selected, and their fast ion energy compared with the correspondent values of W_c. This has been calculated with the PHANTOM code, making use of the values of the minority concentration $\eta = n_{min}/n_{e0}$ derived from the NPA measurements when available. The results are shown in Fig.4.5:both datasets show reasonably good correlation in view of the known experimental uncertainties. However, the possibility of differences between the values of n_{min} in the plasma centre (where heating occurs) and at the edge (where the NPA is active) cannot be entirely eliminated. This could be partially responsible for some of the scatter in the data. In view of this, the sensitivity of the calculated total fast ion energy to variations in the assumed value of the minority concentration has been examined, and the results plotted in Fig.4.6 for two selected discharges characterized by H and ^{3}He minorities and labelled A and B, respectively (see also Fig.4.5). The two curves show that for both types of minority the fast ion energy shows qualitatively the same characteristics. In fact $W_c(\eta)$ increases sharply until it reaches a maximum generally at quite a low value of η, then it decreases, with a slope depending on the minority species. These features can be understood in terms of the physics of the collisional processes involved. At very low minority concentration the presence of the D-shaped orbits causes a net increase in the fast ion friction, leading to a low W_c. As η increases the coupled power per fast ion decreases causing the fast ions to penetrate less and less deeply into the cooler plasma region, so that W_c can reach its maximum. At some stage, though, while η increases the energy damped on the single fast ion becomes of order of the critical energy E_c, so that ion-ion collisions are no longer negligible. Both effects account for the decrease of the fast ion energy for high values of the minority concentration. The different slopes at high η values are also explained remembering that the H ions have a critical energy about three times lower than that of the ^{3}He ions so that in the former case, even at high minority concentration there is a significant contribution to the fast ion energy content.

4.3 Summary and conclusions

In the present Chapter a model, based on the solution of the steady-state pitch-angle averaged Fokker-Planck equation, has been developed to calculate the collisional ion and electron power deposition profiles and the fast ion energy content. This model differs from that developed by T.H. Stix (summarised in Section 4.1) mainly in that the minority ion-electron collision frequency is energy dependent, thus reflecting the changes in collisionality that the resonant minority ion experiences when travelling along one trapped orbit. This has profound implications. Firstly, the number of high energy minority ions (the 'tail' of the distribution) is considerably reduced with respect to the old model. Then, the electron power deposition profile is substantially modified and broadenend, since the power absorbed by the minority ions is now transferred to the electrons in those regions of the plasma with higher collisionality. The ion power deposition profile, on the contrary, is unchanged. Lastly, the fast ion energy content calculated with the orbit model is systematically lower than that estimated with the zero-orbit model, and agrees with experiment well within error bars.

4.4 References

1. G.A. Cottrell and D.F.H. Start, Nucl. Fusion **31** (1991), 61.

2. T.H. Stix, Nucl. Fusion **15** (1975), 737.

3. L. Spitzer Jr., *The Physics of Fully Ionized Gases*, Interscience NY (1962).

4. C.F. Kennel and F. Engelmann, Phys. Fluids **9** (1966), 2377.

5. T.E. Stringer, Plasma Phys. **16** (1974), 651.

6. D. Anderson et *al.*, Nucl. Fusion **27** (1987), 911.

7. D.J. Gambier et *al.*, Nucl. Fusion **30** (1990), 23.

8. D.F.H. Start et *al.*, (1990), to be submitted to Plasma Physics and Controlled Fusion.

5.0 Orbit Effects on the (^{3}He)D Fusion Yield

In the present Chapter the effects that finite orbit width of minority ion orbits have on the fusion yield in a (^{3}He)D plasma during ICRF heating experiments on JET are studied. A series of (^{3}He)D high fusion yield experiments performed on JET at the end of 1990 are therefore considered, the characteristics of which are briefly illustrated in Section 5.1. These discharges have already been analyzed [5.01] assuming an anisotropic Stix [5.02] distribution for the ^{3}He ions (see also Chapter 4) and taking into account their orbit size by broadening the RF power density profile coupled to the minority ions. In Section 5.2 the technique used to measure the reaction rate is described. In Section 5.3 it is shown that neglecting the parallel degree of freedom is strictly incorrect and leads to erroneous results for energies around E_c or lower [5.02]. For this reason both the local reactivity $\Re$ and the total fusion power P_{fus} are at first calculated in this Chapter using a pitch-angle averaged isotropic distribution and are found to be substantially higher than previously estimated (Section 5.3.1). Then orbit effects are introduced (Section 5.3.2). In Section 5.3.3 the same orbit calculations are compared with the experimental results, together with simulations of actual discharges. In Section 5.4 the calculations developed so far are applied to ITER scenarios in order to optimise ICRF heating in (^{3}He)D plasmas before the D(T) active phase. Lastly in Section 5.5 the analysis is summarized and conclusions are drawn.

5.1 Preparation of the experiment and results

In order to obtain the maximum total fusion power output in a two-component plasma it is necessary to achieve the required minority tail temperature by optimising the parameters important for the experiment. To this effect it can be shown (see Appendix B) that, once the tail temperature has reached a value near to the energy of the peak of the reaction rate $< \sigma v >$, the fusion yield can be optimized by varying only the RF power and the electron temperature or, equivalently, the minority concentration η, that is,

$$P_{fus}^{opt} \propto P_{RF} T_{e0}^{3/2} \propto \eta^{opt} ,$$

provided that the profiles of the relevant quantities do not change.

The strategy for optimizing the total fusion power output for a given RF power is therefore to vary the minority density in a high electron temperature discharge in order to maximise $<\sigma v>/T_t$, that is to obtain a tail temperature T_t (see Chapter 4 for its definition) as near as possible to the energy correspondent to that of the peak of the cross-section (~800 keV in the present case). A high T_e discharge usually means low electron density n_e, so H-modes must be avoided, because the electron temperature remains rather low while the density increases throughout the H phase. The best possible scenario makes use of monster sawtooth plasmas. During these discharges the confinement time is higher than during an L-mode (although lower than in the H-mode), and the plasma density can be kept constant by gas puffing during feedback control. The long periods between sawtooth crashes also minimize the ejection of fast ions from the plasma centre. Also care must be taken that the impurity level is kept low in order not to reduce the ratio n_D / n_e. Note that some variation in this ratio is inevitable as $n_{\min}$ is varied. However since for this kind of experiments $n_{\min} \approx 0.1\ n_e$, the effect is small.

In optimizing the minority concentration, the ratio n_{He} / n_D must satisfy the relation [5.01,5.03],

$$0.01 \le n_{He} / n_D \le 1.05 \left(S_{\parallel} \sqrt{\beta_{He}} \right)^{2/3} , \qquad (5.1)$$

in order to avoid excessive mode conversion (upper limit, important especially in monopole antenna phasing when $k_{||}$ is low), and to ensure sufficient wave damping (lower limit). In Eq.(5.1) $S_{\parallel} = k_{\parallel} c / \omega_{pD}$ is the averaged normalized wavenumber of the incident wave at the resonance, while β_{He} is the kinetic pressure of the minority species normalized to the magnetic pressure. During these experiments however the fast wave has been launched in monopole phasing, with parallel wavenumber $-3\mathrm{m}^{-1} \le k_{\parallel} \le 3\mathrm{m}^{-1}$. Part of this spectrum therefore violates the criterion given by Eq.(5.1), contributing to direct electron heating which, however, is found not to exceed 20% of the RF power coupled to the plasma (see Chapter 3 for the technique used for the measurement). Because of technical problems with the RF plant,

discharges in dipole phasing did not exceed 4 MW of coupled power [5.01] and are therefore not considered in the present analysis.

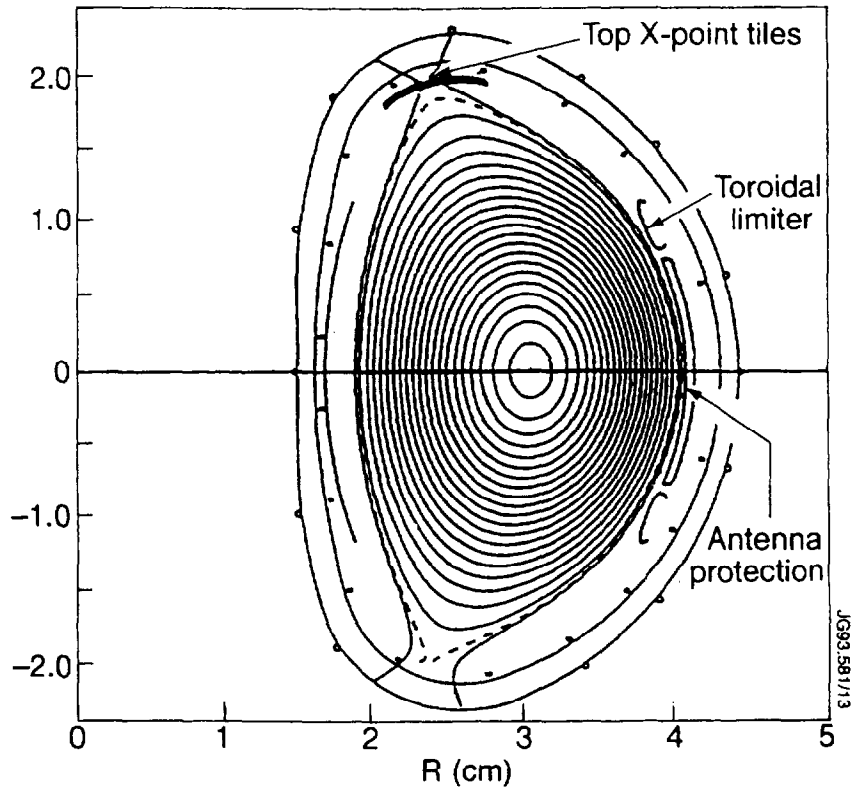

Figure 5.1 Magnetic configuration of the high fusion yield experiment.

Within these limits, the Stix expression for the tail temperature [5.02] can be used to obtain the optimum ^{3}He concentration [5.01],

$$(n_{He}/n_e)_{opt} = 8.4\times10^{31}\,\frac{\rho_{He}(\mathrm{MWm^{-3}})T_e^{3/2}(\mathrm{eV})}{n_e^2(\mathrm{m^{-3}})}\,, \qquad (5.2)$$

where ρ_{He} is the RF power density coupled to the minority ions. Unfortunately on JET it is not possible to measure the minority concentration in the plasma centre, but only at the edge by using the Neutral Particle Analyser (see Chapter 3 for details). Thus in this experiment both gas puffing and the NBI system have been used, the latter providing a central source of helium by injecting a known quantity of high energy neutrals. Since the beams energy is 120 keV and their power only 1.2MW, they do not contribute to the fusion yield.

In these experiments the impurity influx has been kept low by minimizing the power loading on the first wall components. This is achieved by keeping the plasma in contact with the upper divertor target plates (in carbon), the belt limiters (in beryllium) and the RF antenna side protections (also in carbon). As a consequence the plasma is very triangular and elongated (see Fig.5.1). Also the presence of beryllium Faraday screens reduces to negligible levels the impurities produced by the antennae due to the low sputtering coefficient of Be at high energy [5.04,5.05]. The overall effect is to keep the effective ionic charge Z_{eff} as low as 2 for most cases (see Table 5.2) for electron densities around 2.5×10^{19} m^{-3}. Transition to H-mode is avoided by particle recycling with limiters on the low magnetic field side.

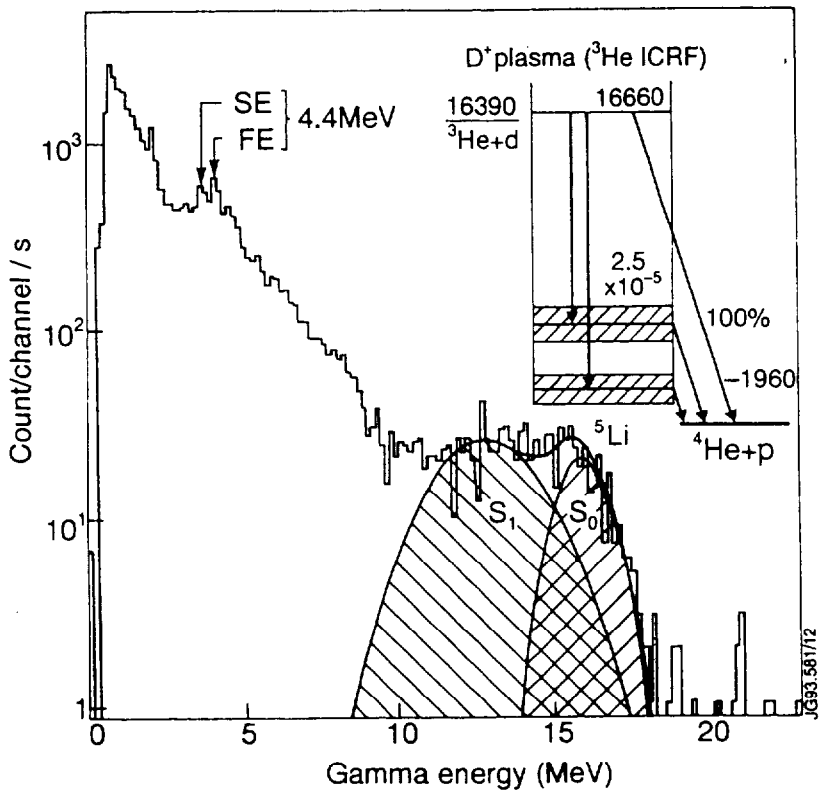

Figure 5.2 **γ spectrum measured during high power ^{3}He minority heating** (courtesy of G. Sadler).

With these guidelines, up to 15 MW of RF power were coupled to an (^{3}He)D plasma in a series of discharges performed at the end of 1990. Measurements of electron temperature and density variations during modulations in the RF waveform show that about 80% of the coupled power is absorbed by the ^{3}He ions. The remaining part is damped on electrons through a combination of mode conversion, TTMP and Electron Landau Damping (see Chapter 3 for the technique used for the measurement). From the ECE spectrum the ^{3}He cyclotron resonance position has been

estimated to be about 4 cm from the magnetic axis position in most cases, with the exception of some cases where a few of the RF generators were resonating at about 10 cm from R_0. For all the data-points considered here, the fast ion energy content does not exceed 1.5 MJ.

5.2 Measurement of the ^{3}He-D reaction rate

When ICRF is applied, the resonant minority ions may acquire enough energy to undergo fusion reactions with the background ions. The unique proof that these reactions have taken place is the emission of photons in the γ energy spectrum. The main fusion reaction,

$$^3\text{He} + \text{D} \rightarrow {}^4\text{He}\ (3.7\ \text{MeV}) + \text{p}\ (15\ \text{MeV}) ,$$

can be monitored by measuring the 16 MeV photons emitted in the weak (0.03%) secondary reaction,

$$^3\text{He} + \text{D} \rightarrow {}^5\text{Li} + \gamma\ (16.6\ \text{MeV}) .$$

This is done in JET by means of one NaI(Tl) scintillator and two BGO crystals, with an intrinsic efficiency of 50%. These two branches are shown in the decay scheme of Fig.5.2, together with a typical spectrum obtained with the NaI detector [5.04]. These detectors view the plasma vertically along two similar lines of sight from two shielded locations in the Roof Laboratory, shown schematicaly in Fig.5.3. Remote controlled pre-collimators are positioned on top of the vertical ports of the vacuum vessel. To compensate for the narrower line of sight imposed by the pre-collimators, an horizontal line of sight has been also installed, which however in the series of experiments considered here has been used only to check the volume integration of the emission as deduced from the NaI detector. Extra Pb absorbers have been added to attenuate the γ-ray flux. They absorb the low energy γ's preferentially, thus reducing the count rate and therefore the risk of electronic pile-up which would give spurious counts in the 16 MeV region. The count-rate is then converted into total γ yield, and finally into total fusion power.

Together with γ-rays produced by the ^{3}He(D,γ)^{5}Li reaction, the detectors also measure the reactions that high energy ^{3}He ions undergo with beryllium [5.06],

$$^3\text{He} + {}^9\text{Be} \rightarrow {}^{11}\text{B} + \text{p} + \gamma\ (6.7\ \text{MeV}),$$

$$^{3}He + {}^{9}Be \rightarrow {}^{11}C + n + \gamma\,(6.3\ MeV),$$

which is present in the plasma as impurity. Reactions with high energy levels of ^{9}Be ions can produce γ-rays in a broad energy spectrum which cannot be resolved by the detector and as a consequence are picked up as a spurious signal which in extreme cases can mask the spectrum in the 16 MeV region. For this reason some potentially good discharges had to be discarded.

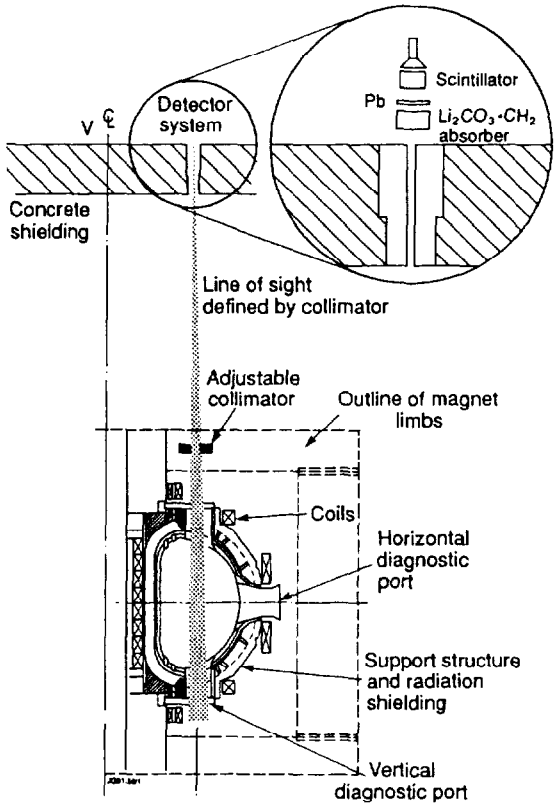

Figure 5.3 Experimental arrangement of the γ detectors in JET (courtesy of G. Sadler).

5.3 Local reactivity and total fusion power

In this Section the local reactivity $\Re$ and the total fusion power P_{fus} are calculated, and the results compared with both previous estimates and with the experiment. Thus, after defining the radial profiles of the plasma parameters used throughout the analysis, it is shown why the use made in [5.01] of the anisotropic distribution function is not correct. A comparison is then made between the old and the new results without orbit effects. Lastly, orbits are introduced, and the results are discussed.

Consider then the power density profile coupled to the minority ions, given by,

$$\rho_{He}(r) = \frac{P_{RF}}{2\pi^2 R_0 w^2 \varepsilon} e^{-r^2/w^2} , \tag{5.3}$$

where ε=1.3 is the plasma ellipticity. As usual, when orbits are considered the half-width of the Gaussian given by Eq.(5.3) is set to w=0.30m (see Chapter 4).

In order to compare most effectively the presents calculations with those in [5.01], the same radial profiles of the plasma parameters of [5.01] are used. Thus, the electron density and temperature profiles read,

$$n_e(r) = (n_{e0} - n_{ea})\left[1 - (r/a_0)^2\right]^{0.5} + n_{ea} ,$$

$$T_e(r) = (T_{e0} - T_{ea})\left[1 - (r/a_0)^2\right]^{4} + T_{ea} .$$

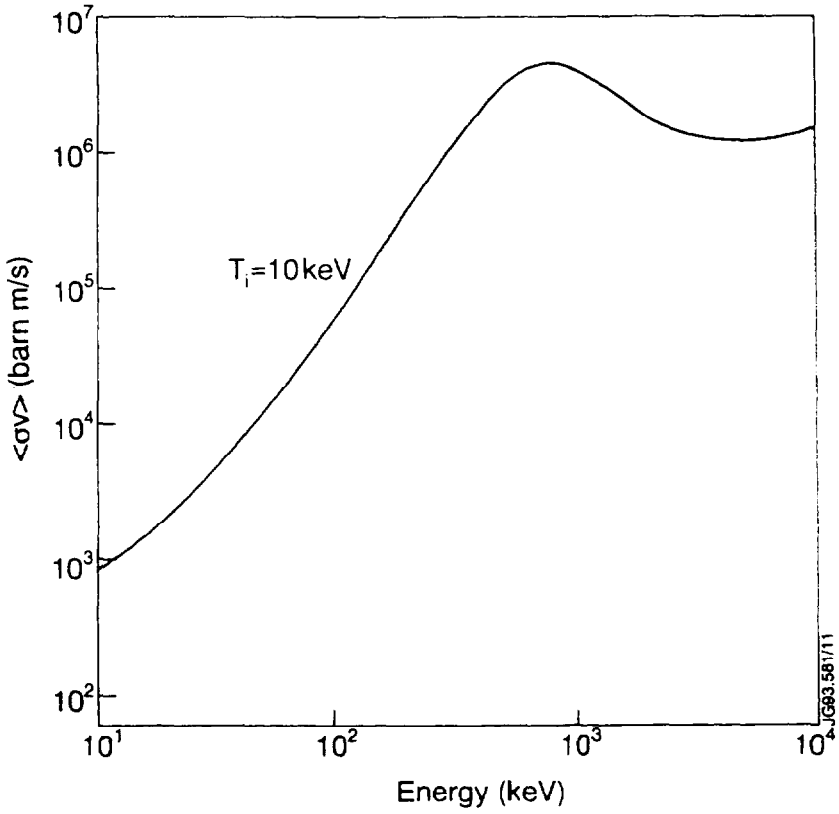

Figure 5.4 **Plot of the ^{3}He-D reaction rate.** <σv> has been averaged over a Maxwellian background distribution of D ions at T_i=10 keV colliding with test ^{3}He particles and using an updated cross-section.

The ^{3}He and deuterium density profiles are assumed to be in a fixed ratio with the electron density profile, namely,

$$n_{He}(r)/n_e(r) = \eta \ ,$$

$$n_D(r)/n_e(r) = \frac{Z_{eff} - Z_{imp}}{1+4\eta - Z_{imp}(1+2\eta)} \ ,$$

where Z_{imp}=4 is the ionic charge of the main impurity present in the plasma (beryllium in the present case), while Z_{eff}=2 for these calculations unless stated otherwise. Lastly, the deuterium temperature is also taken to be,

$$T_i(r)/T_e(r) = 0.8 \ .$$

In order to calculate the reactivity it is necessary to know the reaction rate $<\sigma v>$. This analysis uses a $<\sigma v>$ averaged over a Maxwellian background distribution of deuterium ions at a temperature T_i=10 keV colliding with ^{3}He test particles and using an updated ^{3}He-D cross-section [5.07]. A plot of the reaction rate as a function of energy is shown in Fig.5.4. Note that the peak of the reactivity is around 800 keV.

5.3.1 Zero orbit reactivity

In [5.01] the local reactivity $\Re$ and the total fusion power P_{fus} are calculated assuming an anisotropic distribution $f(E_\perp)$ of the minority species as given by Stix [5.02] (see also Chapter 4, Eq.(4.16)). Furthermore orbit effects are taken into account by broadening the power density profile and setting w=0.35m.

It is here shown that to use $f(E_\perp)$ is not correct, for the following reason. Consider the reactivity calculated using the steady-state distribution, which is a function of both velocity v and pitch angle μ [5.02],

$$\Re = \frac{n_D n_{He}}{f_0} \int_0^\infty dv v^2 <\sigma v> \int_{-1}^{1} d\mu f_{m,a}(v,\mu) \ , \qquad (5.4)$$

where as usual $f_0 = \int_{-1}^{1}\int_0^\infty d\mu dv \ v^2 f_{m,a}(\mu,v)$ is the normalization constant. If $f_{m,a}$ is expanded in a series of Legendre polynomials,

$$f_{m,a}(v,\mu)=\sum_{l=0}^{\infty} g_{2l}(v)P_{2l}(\mu)\ ,$$

then the reactivity can be written as,

$$\Re=\frac{n_D n_{He}}{f_0}\int_0^{\infty} dv v^2 g_0(v)<\sigma v>+\frac{n_D n_{He}}{f_0}\int_0^{\infty} dv v^2<\sigma v>\sum_{l=1}^{\infty} g_{2l}(v)\int_{-1}^{1} d\mu P_{2l}(\mu)\ , \quad (5.5)$$

where the second integral on the RHS is zero since $\int_{-1}^{1} d\mu P_{2l}(\mu)=0 \quad \forall l>0$. The reactivity is therefore calculated correctly *only* by using a distribution isotropic in velocity space. This can be estimated by considering the steady-state pitch-angle averaged Fokker-Planck equation [5.08],

$$<C(f)>+<Q(f)>=0=.\frac{1}{v^2}\frac{d}{dv}\left\{\left[-\alpha v^2+\frac{1}{2}\frac{d}{dv}(\beta v^2)\right]+\frac{1}{2}\beta v^2\frac{d}{dv}\right\}<f> \\ +\frac{3K}{2v^2}\frac{d}{dv}\left[v^2\frac{d}{dv}<(1-3\mu^2)f>+v<(1-3\mu^2)f>\right]\ . \quad (5.6)$$

The zero and second order moments of f in Eq.(5.6) can be formally decoupled by following D. Anderson, L.-G. Eriksson and M. Lisak [5.08], and L.-O. Pekkari [5.09] and introduce an effective pitch-angle,

$$<\mu^2 f>=\mu_{eff}^2<f>\ , \quad (5.7)$$

defined as,

$$\mu_{eff}^2=\frac{1}{3}\frac{1+(v/v_*)^2}{1+(v/v_*)^2+(v/v_*)^4}\ . \quad (5.8)$$

In Eq.(5.8) v_* is proportional to the velocity v_γ over which the pitch-angle ceases to be important. Such velocity has been estimated by Stix [5.02] to be,

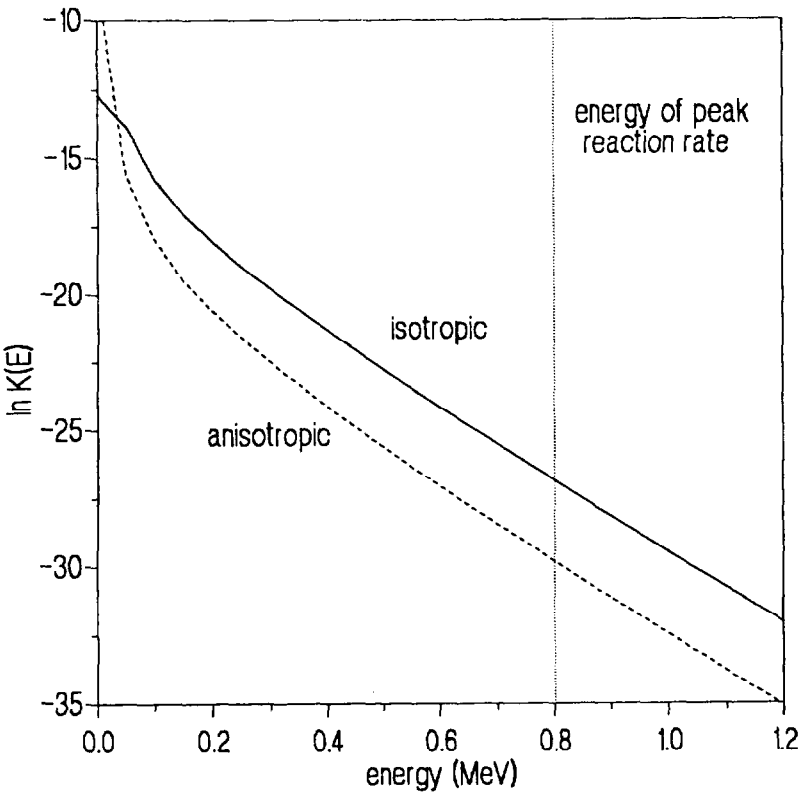

Figure 5.5 **Comparison between the isotropic and anisotropic distribution functions.** In the picture *K(E)* represents the kernel in the integral Eq.(5.4): $K(E)=\sqrt{E}f(E)$ for the isotropic distribution, and $K(E)=f(E_{\perp})$ for the anisotropic one. The distributions have been estimated for the parameters relative to simulation B at r/R_0=0.166 and $\eta=0.11$, correspondent to the peak reactivity.

$$\frac{1}{2}mv_{\gamma}^2=E_{\gamma}=14.8k_BT_e\left[\frac{2A^{1/2}}{n_e}\sum_i Z_i^2 n_i\right]^{2/3}. \tag{5.9}$$

Following D. Anderson, L.-G. Eriksson and M. Lisak [5.08], v_* is set to be $v_*=0.42v_{\gamma}$ thus enabling the present distribution function to accurately represent the ^{3}He-D fusion yield predicted by the 2-D Fokker-Planck code BAFIC [5.08]. Eq.(5.6) can thus be solved to obtain,

$$\begin{aligned}\ln\frac{<f>}{f_0}=&-\frac{1}{k_BT_e}\int_0^E\frac{dE}{1+\omega(1-\mu_{eff}^2)}\left\{1+\frac{R_i[T_e-T_i+T_e\omega(1-\mu_{eff}^2)]}{T_i[1+R_i+\omega(1-\mu_{eff}^2)]}\frac{1}{1+(E/\tilde{E}_i)^{3/2}}\right\}+\\&-\int_0^E\frac{dE}{2E}\frac{\omega(1-3\mu_{eff}^2-vd\mu_{eff}^2/dv)}{1+\omega(1-\mu_{eff}^2)}\left\{1-\frac{R_i}{1+R_i+\omega(1-\mu_{eff}^2)}\frac{1}{1+(E/\tilde{E}_i)^{3/2}}\right\},\end{aligned} \tag{5.10}$$

where $\omega = 3\xi_{Stix}/2$. With reference to Eq.(4.8) and related definitions,one can see that the expressions for R_i and $\tilde{E}_i$ of Chapter 4 correspond to those of Eq.(5.10) if to ξ is substituted $\xi_{eff} = \omega(1-\mu_{eff}^2)$, while,

$$v\frac{d\mu_{eff}^2}{dv} = -\frac{2}{3}(E/E_*)^2\frac{2+E/E_*}{[1+E/E_*+(E/E_*)^2]^2},$$

with $E_* = 0.1764E_\gamma$. Note that in the limits of low energy, when $\mu_{eff}^2 \to 1/3$, and of high energy, when $\mu_{eff}^2 \to 0$, the second integral on the RHS of Eq.(5.10) goes to zero. However while in the first case $< f >$ becomes the Stix isotropic $f(E)$, in the second case $< f >$ tends to the anisotropic $f(E_\perp)$ (see Chapter 4 or [5.02]). Eq.(5.11) thus provides a link between $f(E)$ (valid when $E \cong E_c$) and $f(E_\perp)$, valid in the strongly anisotropic regime ($E \cong E_\perp \gg E_c$). Note also that use of Eq.(5.10) rathen than Eq.(4.28) does not introduce significant differences in the calculation of the heating profiles (see Appendix C).

Use of the anisotropic $f(E_\perp)$ leads to an underestimate of the reactivity of about 20% as deduced from the difference between the two distribution functions shown in Fig.5.5 and calculated for the parameters relevant to Simulation B in Table 5.1, at the energy (and radius) corresponding to the peak of the reaction rate. These distributions are normalized to the same ^{3}He density.

By means of Eq.(5.10), and setting as in [5.01] w=0.35m in Eq.(5.3), the values of the local reactivity,

$$\Re(r) = \frac{n_D n_{He}}{f_0}\int_0^\infty dE\sqrt{E} < f > (E) < \sigma v > (E), \qquad (5.11)$$

and the total fusion power,

$$P_{fus} = 4\pi^2 R_0 \varepsilon e 18.3\times 10^6 \int_0^{a_0} dr\, r\, \Re(r), \qquad (5.12)$$

can now be calculated. To be consistent with [5.01], P_{fus} is plotted in Fig.5.6 against the average perpendicular energy of the minority ions,

$$< W_{He} >= 4\pi^2 R_0 e \int_0^{a_n} dr\, r \frac{\int_0^{\infty} dE_\perp E_\perp f(E_\perp)}{\int_0^{\infty} dE_\perp f(E_\perp)}, \qquad (5.14)$$

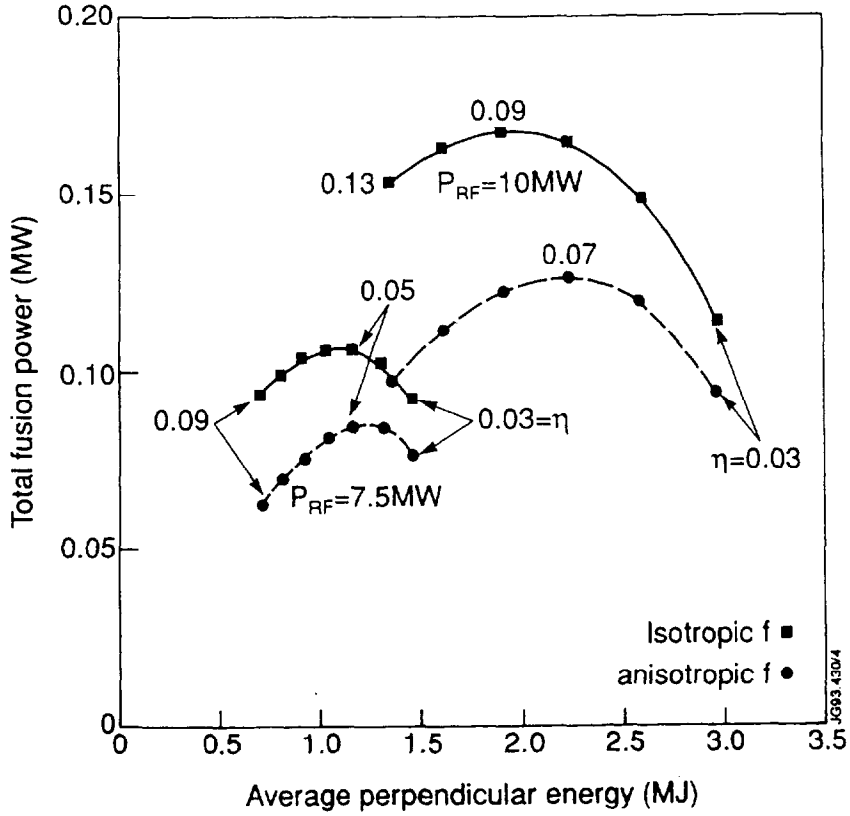

Figure 5.6 Fusion yield calculated with isotropic and anisotropic distributions. The curves refer to simulations A (P_{RF}=7.5 MW) and B (P_{RF}=10 MW) and are plotted against the average perpendicular energy of the minority ions (different from the fast ion energy).

for different minority concentrations. Note that the expression given by Eq.(5.14) and used in [5.01] does not coincide with the fast ion energy content W_c as measured in JET (see Chapter 3) and mathematically defined in Chapter 4, because here the particles with energy $E \cong E_c$ or lower are also considered. In general $< W_{He} > \; > W_c$.

Table 5.1. Parameters for (^{3}He)D Fusion Yield Simulations

	Simulation A	Simulation B
central electron density (10^{19} m^{-3})	2.5	2.5
central electron temperature (keV)	8	10
central ion temperature (keV)	6	8
RF coupled power (MW)	7.5	10
Z_{eff}	2	2

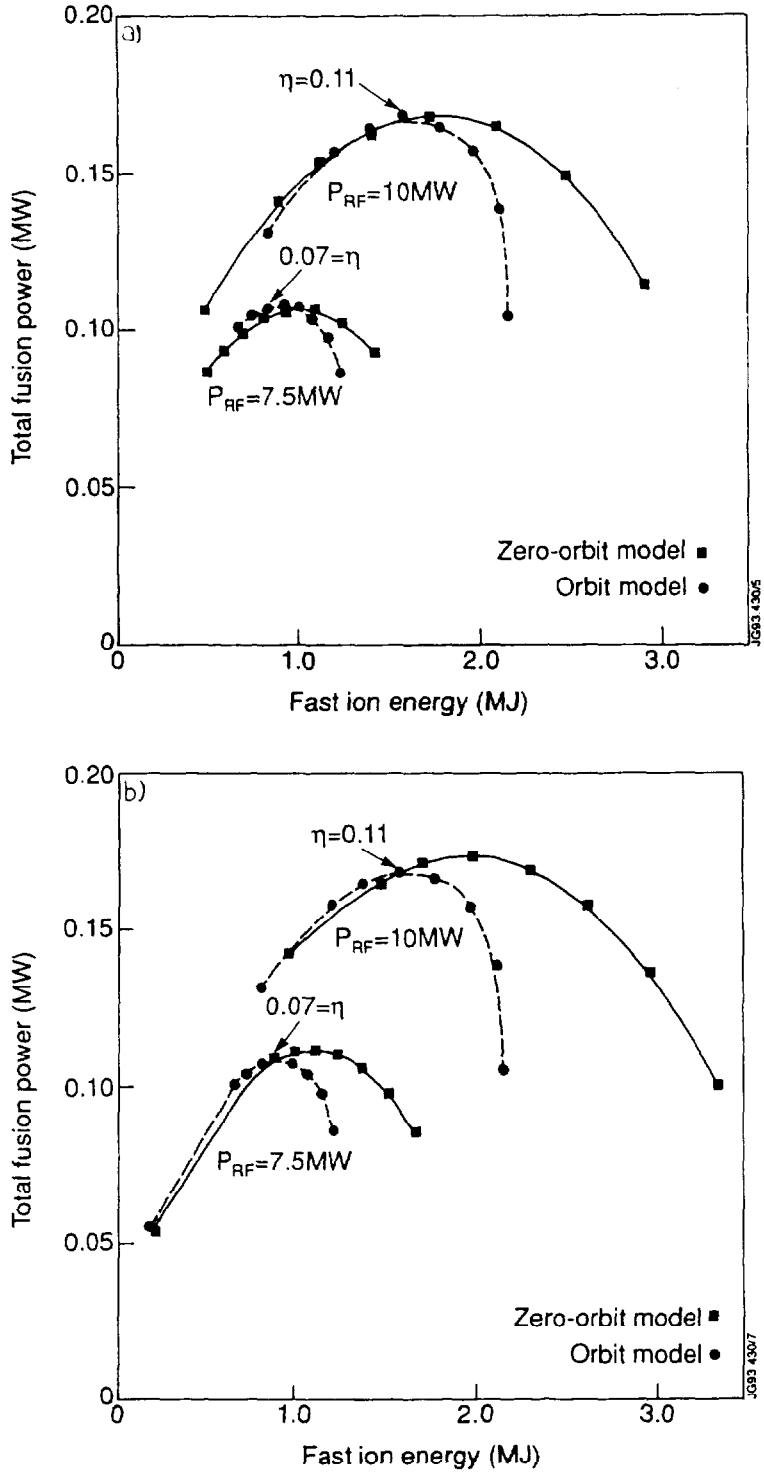

Figure 5.7 **Comparison between zero-orbit and orbit fusion yields.** P_{fus} is calculated with the isotropic distribution function and an RF half-width w=0.30 m for the orbit case. In the case of the zero-orbit model P_{fus} has been estimated using a broader RF power density profile (w=0.35 m, Fig.5.7a) to simulate orbit effects and the same half-width of the orbit model (Fig.5.7b). In both cases the fusion yield is plotted against the fast ion energy.

The results shown in Fig.5.6 correspond to the two simulations labelled A, B in Table 5.1: the maximum fusion yield calculated with the isotropic distribution function is a factor 1.25 greater than that with the anisotropic distribution function. The reason, as shown in Fig.5.5, is that in the latter case (anisotropic) there are fewer ^{3}He ions at the optimum energy (800 keV). Note also that the two curves of Fig.5.6 relative to the same RF power at high minority concentration are farthest apart, since $< f >$ tends to the usual Stix isotropic distribution. On the contrary, at low η they come together, since at high power per particle $< f >$ tends to the anisotropic Stix distribution.

5.3.2 Reactivity calculations including fast ion orbits

The second step in the present analysis is to include finite orbit effects in the estimate of the reactivity $\Re$. This is done by introducing orbits in Eq.(5.10) in a way very similar to that used in Chapter 4 to deduce Eq.(4.28). The results of the orbit calculations are reported in Fig.5.7. In order to better compare the results with the experiment (see Section 5.3.3), both zero-orbit and orbit P_{fus} are plotted against the

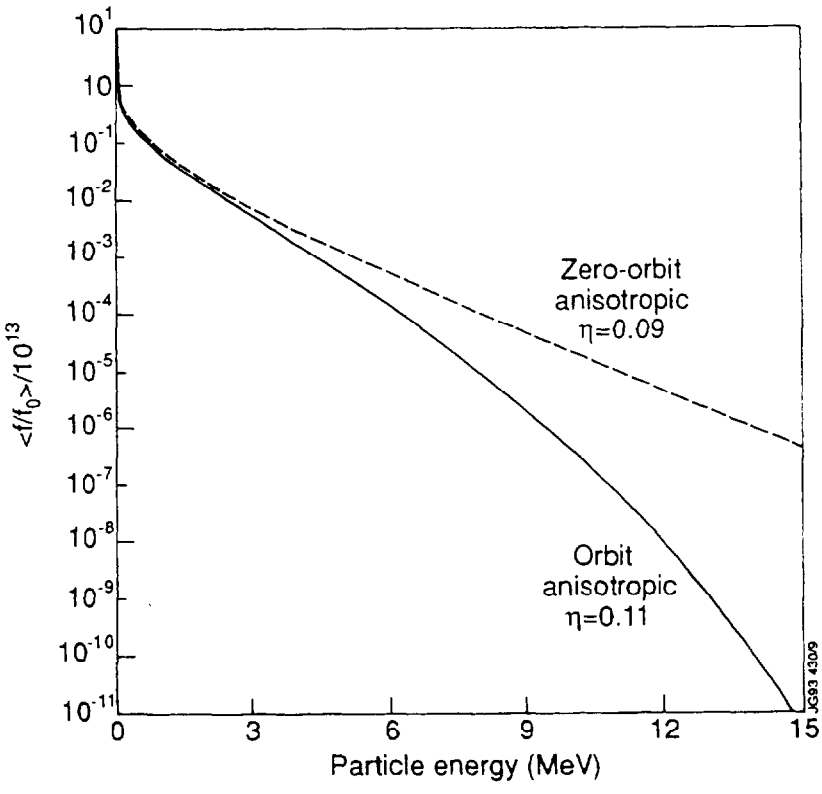

Figure 5.8 Comparison between zero-orbit and orbit anisotropic distributions. Both distribution functions have been calculated for the parameters correspondent to the peak of the reaction rate and averaged over the minor radius.

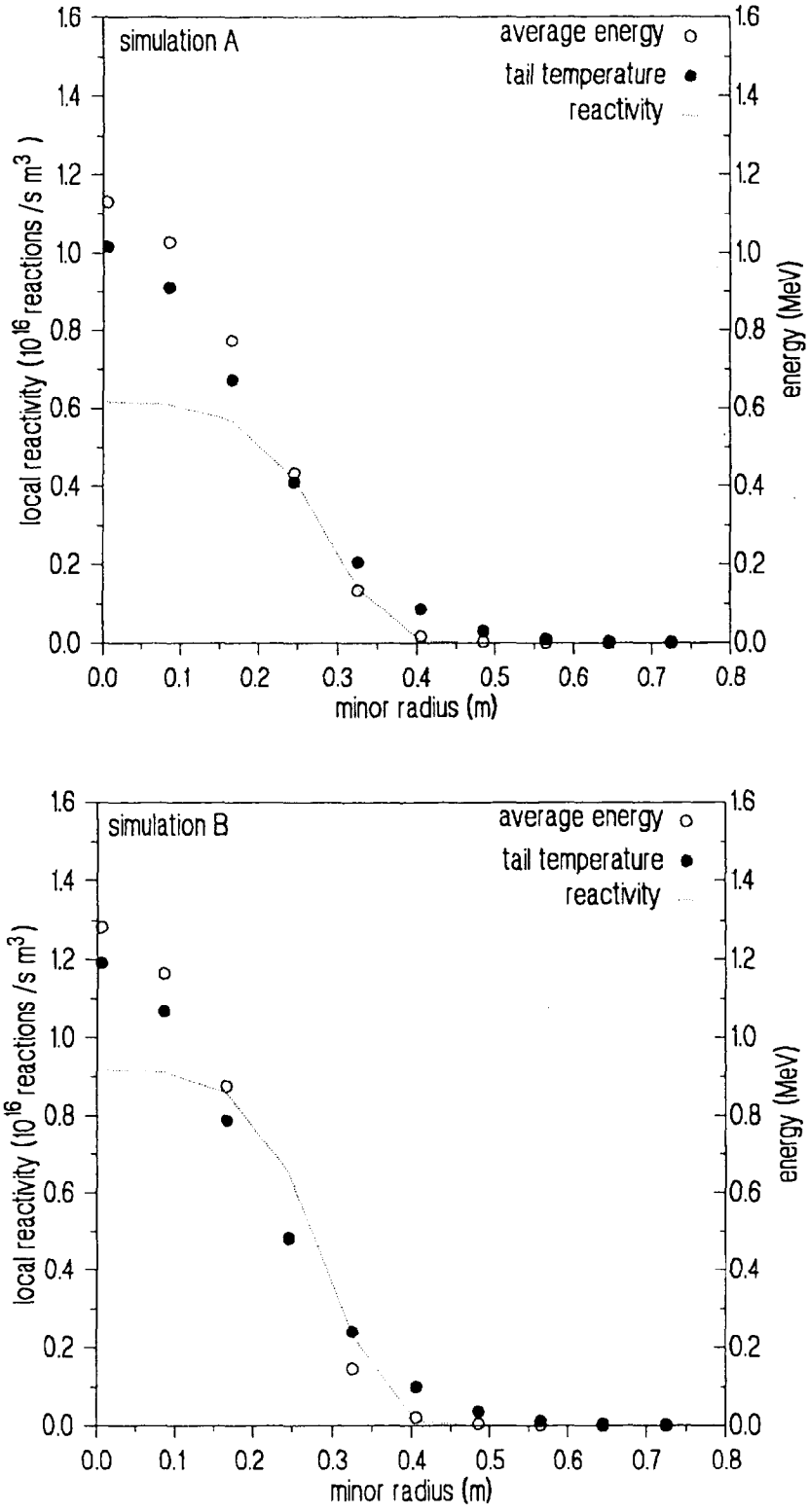

Figure 5.9 **Local reactivity.** The local reactivity correspondent to the peak P_{fus} is plotted for simulations A (Fig.5.9a) and B (Fig.5.9b) together with the profiles of the tail temperature (full circles) and of the average energy per minority ion (open circles).

calculated fast ion energy W_c as given by Eq.(4.31). If orbit effects are artificially introduced in the zero-orbit calculations by broadening the RF power density profile (w=0.35 m in Fig.5.7a), then the two models predict roughly the same amounts of fusion power. However if the same RF half-width (w=0.30 m) is assumed in both calculations, then from Fig.5.7b it follows that orbit effects contribute to decrease slightly the fusion yield. This can be explained by remembering that the zero-orbit model overestimates the number of particles in the critical energy range (~800 keV). Note that at high minority concentration there is no significant difference between the two models, since they both predict roughly the same amount of fusion power (and of fast ion energy contents) for a given η. This is due to the decreased size (and importance) of orbits caused by the lower power per particle available at higher η.

Another consequence of orbit effects is that for both simulations at 7.5 MW and 10 MW the peak of the fusion power is shifted towards lower fast ion energy with respect to its zero-orbit counterpart. This effect can be explained by comparing the zero-orbit and orbit distribution functions at a flux surface radius correspondent to the peak of P_{fus}. At low energy the two isotropic distributions roughly coincide, that is they predict the same number of particles in this energy range, thus yielding to similar amounts of fusion power. Consider however the anisotropic distribution averaged over the minor radius, which is used to calculate W_c, as in Fig.5.8: at high energy the orbit $<f(E_\perp)>$ decreases much more rapidly than the zero-orbit distribution does. Use of the latter then leads to an overestimate of the number of high energy particles and to the shift of the P_{fus} peak towards lower η.

A notable feature of the curves in Fig.5.7 is that the total fusion power at the peak is in the same ratio of the corresponding minority concentration, that is $\eta_{10MW} / \eta_{7.5MW} \cong 1.5$. This has been confirmed with another series of simulations using a different value of the electron density and different RF power levels. In order to understand physically this relation, the local reactivity $\Re(r)$ corresponding to the peak of P_{fus} has been plotted in Fig.5.9 together with the local average energy per fast ion, defined by,

$$< W >= \frac{\int_0^\infty dE E\sqrt{E} < f > (E)}{\int_0^\infty dE\sqrt{E} < f > (E)}, \qquad (5.14)$$

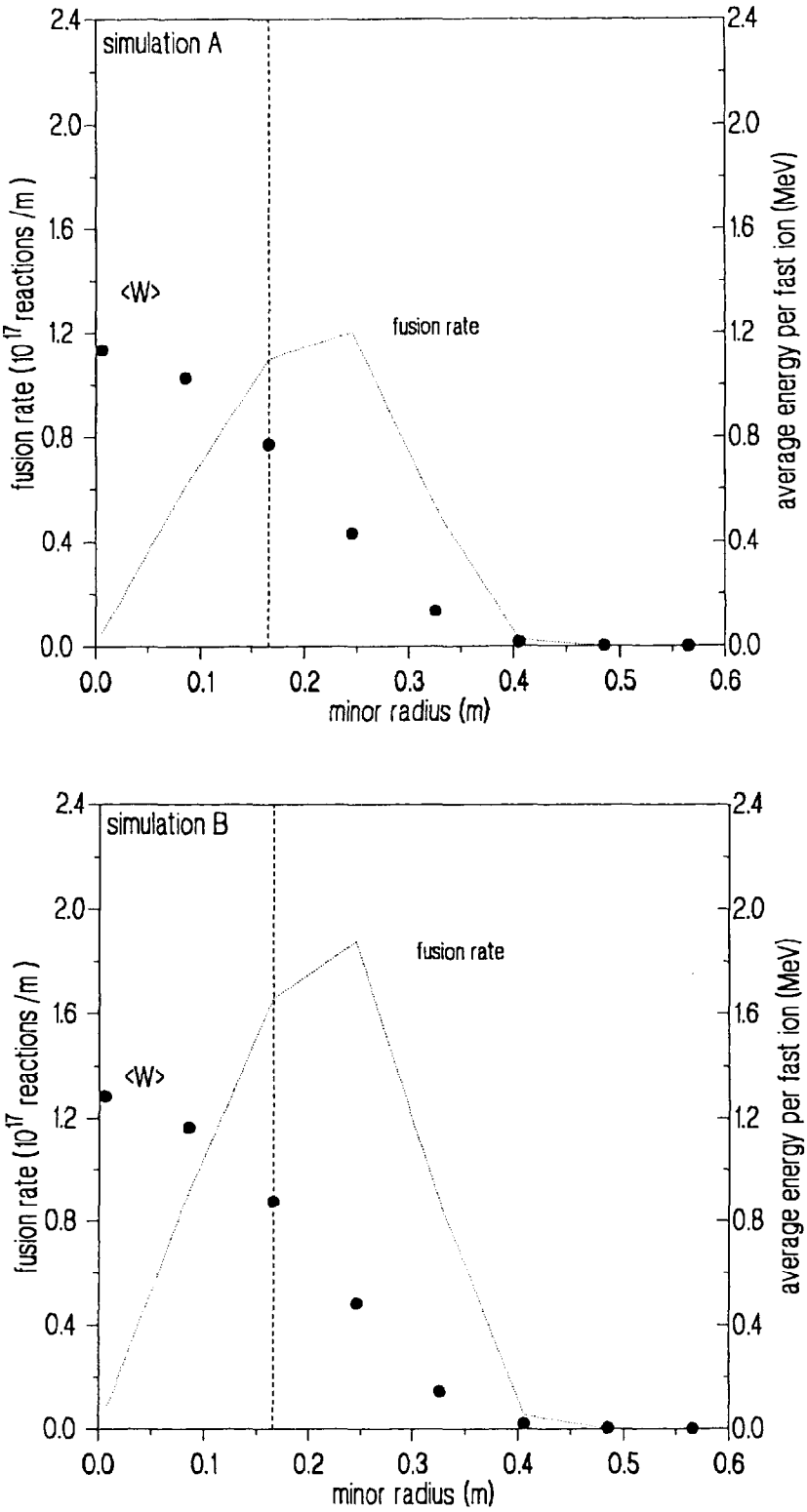

Figure 5.10 Effects of geometry on the local reactivity. the fusion rate per meter of minor radius, $4\pi^2 R_0 r\Re(r)$, is plotted together with the average energy per fast ion $<W>$ for simulations A (Fig.5.10a) and B (Fig.5.10b). The peak fusion rate occurs around where $<W> \cong 800$ keV (at the peak of the cross-section).

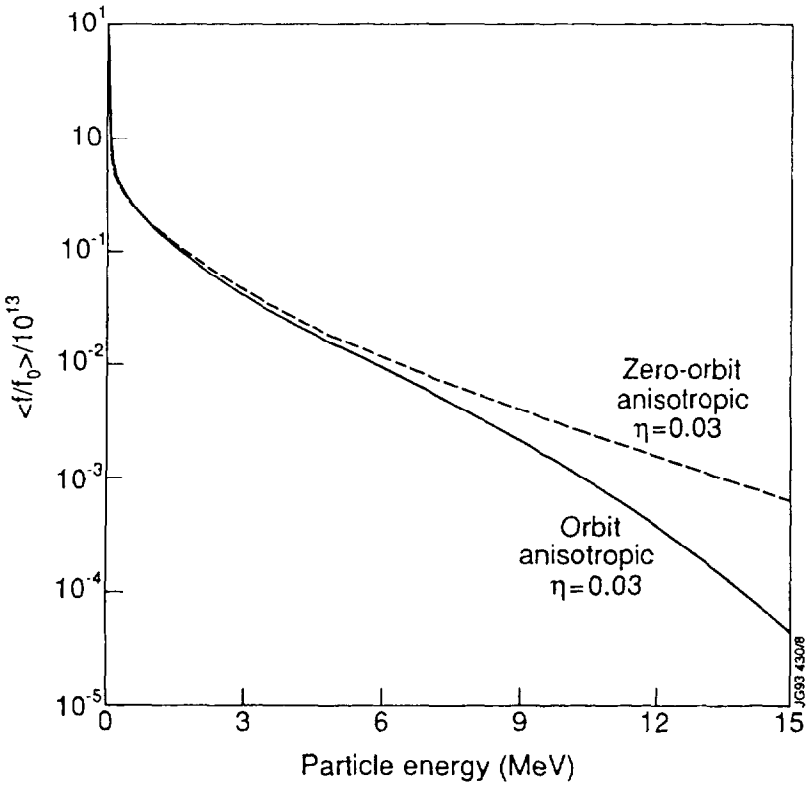

Figure 5.11 Orbit and zero-orbit distribution functions at η=0.03.

and the local tail temperature for the two RF powers considered. Comparison between Figs.5.9a-b shows that while the central reactivities differ of about 35%, reflecting the different RF power levels, both the average energy and the tail temperature do not vary appreciably (within 10%). In other words, the peak fusion power output corresponds to the optimum local ^{3}He tail temperature for the fusion reaction to occur. Furthermore, if the effect of geometry (volume) is taken into account by plotting the fusion rate per meter of minor radius, $4\pi^2 R_0 r\Re(r)$, as in Fig.5.10, it is clear that the peak reactivity is obtained at a distance from the plasma centre corresponding to $<W>$ ≅800 keV (i.e., at the peak of the cross-section).

Lastly, it can be noticed that when η decreases, the orbit P_{fus} as a function of W_c decreases much more rapidly than in the zero-orbit case. To explain this last feature, consider again the zero-orbit and orbit distribution functions, both isotropic and anisotropic and averaged over the minor radius, for P_{RF}=10 MW and η=0.03 (the lowest minority concentration considered in the curves of Fig.5.7). Around the optimum energy of the cross-section (800 keV) both isotropic distributions predict the same number of ^{3}He ions, so that the total fusion output in the two cases is roughly the same. Consider now the anisotropic $<f(E_\perp)>$, as in Fig.5.11: although at such a low

minority concentration the high energy ^{3}He are a significant fraction of the total number of minority ions, the Stix distribution largely overestimates their number, thus leading to a larger value of the fast ion energy content W_c.

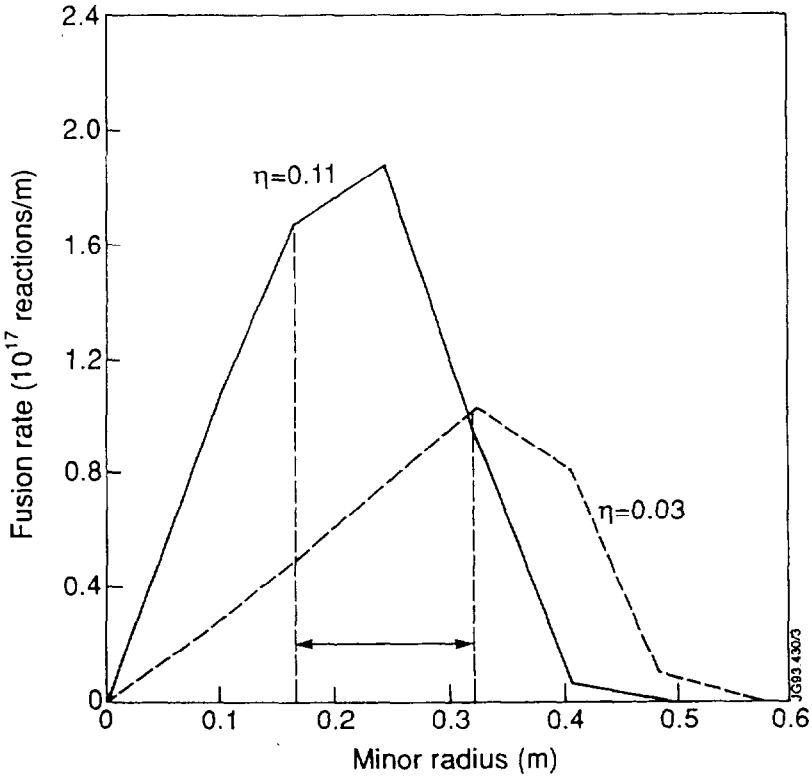

Figure 5.12 Fusion rate for simultion B at η=0.11,0.03. To η=0.11 corresponds the peak of the fusion yield, to η=0.03 its lowest value.

Note that the decrease of η of more than a factor of three from the peak of the fusion yield to its lowest vallue cannot explain alone why P_{fus} itself decreases much less rapidly (from 0.17 MW to 0.10 MW, that is less than of a factor of two). To understand this, the volume effect due to the plasma geometry must be taken into account. In Fig.5.12 the fusion rate is plotted at 10 MW of ICRF with η=0.11,0.03: note that the radius corresponding to the optimum fusion yield moves outwards when η drops. As a consequence, the decrease in P_{fus} due to the decreased η is compensated by the bigger plasma volume occupied by the region of optimum yield. The two opposite effects thus produce a less than linear scaling of P_{fus} with the minority concentration, all other parameters being kept constant.

It can then be concluded that there is no big difference between the two models as far as the *magnitude* of P_{fus} is concerned. However the fast ion energy

content is strongly influenced by orbit effects and is very sensitive to variations in the minority concentration. On this respect the two models are critically different.

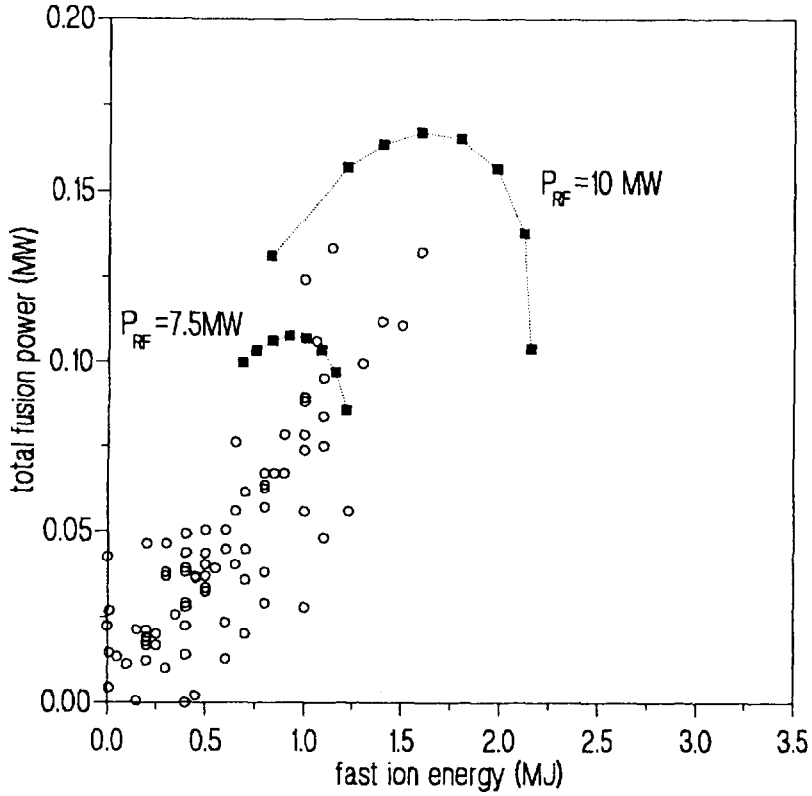

Figure 5.13 Experimental and numerical fusion yield. The numerical curves are the same of Fig.5.7.

5.3.3 Comparison with the experiment

The most serious consequence of the present model is that, given a set of experimental parameters, the fusion power output that can be obtained is higher than previously estimated. Therefore if the two orbit P_{fus} curves of Fig.5.7 are plotted together with the experimental data points of the total fusion output, as in Fig.5.13, it is clear that, if the model is correct, for various reasons the experiment did not fulfill its potentialities. In order to check if this is the case, three discharges have been simulated using the measured plasma parameters. In two cases (JPN 23399 and 23438) the NBI system has been used to provide a central source of helium. In the third case (JPN 23489, where 133 kW of fusion power have been produced) only gas puffing has been used. Their central electron temperature varies from 10 to 12 keV, the RF coupled power from 9 to 13 MW, and the central electron density from 2.2 to 2.75×10^{19} m^{-3} (in Table 5.2 the plasma parameters and the results of the simulations are listed for the three discharges). Fig.5.14 shows the time evolution of the main

parameters for two of them. Note that discharge 23438 (Fig.5.14a) has a modulation in the RF power waveform, so that from the temporal response of electron density and

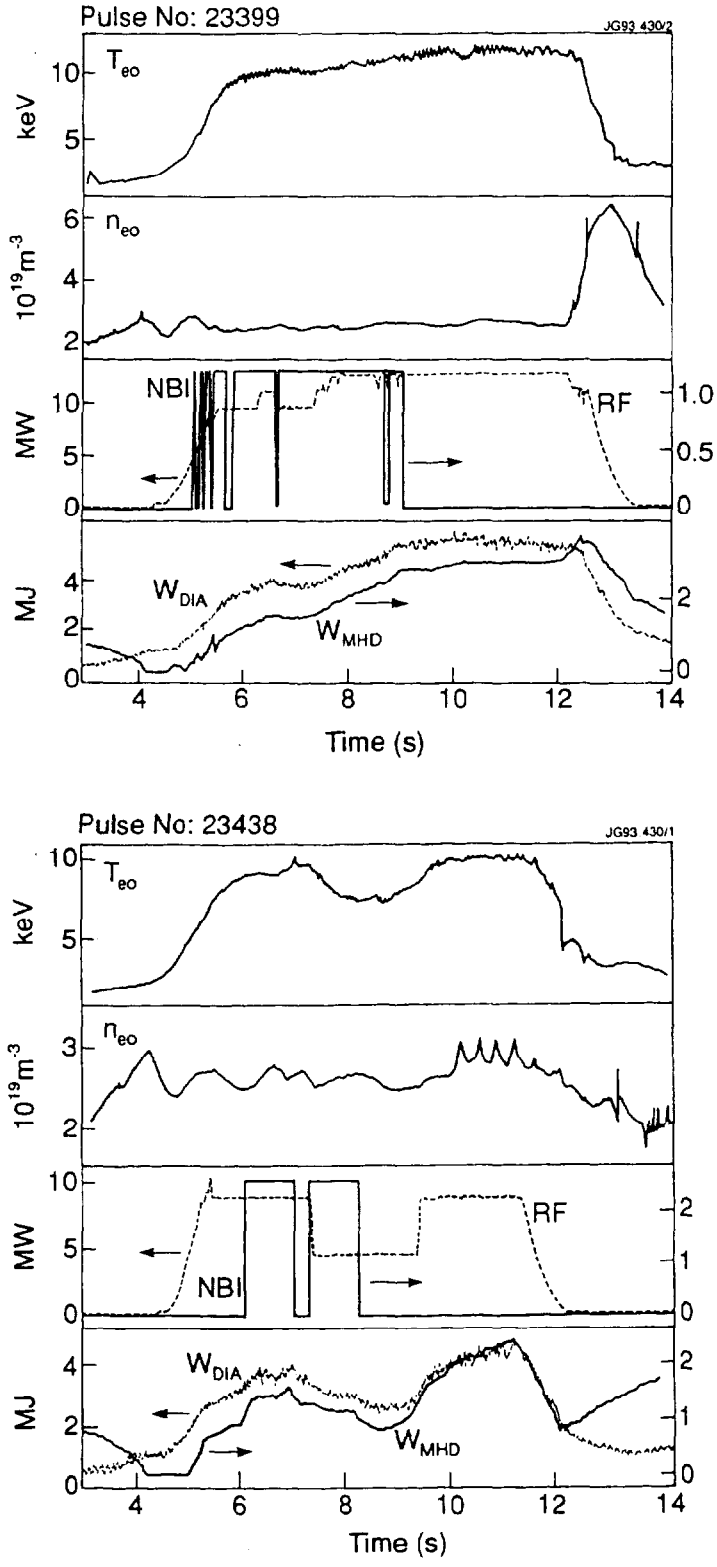

Figure 5.14 Time evolution of the main plasma parameters for discharges 23399 and 23438.

temperature at different radial positions the fraction of direct electron heating can be estimated (see Chapter 3 for details on this technique). In Fig.5.14b is instead shown the time evolution of discharge #23399, which in many respects is far from being ideal. About two seconds before the time-slice considered here (t_0=10 s), the NBI system injected ^{3}He neutrals for about 4 seconds (instead of 2 seconds, as in Fig.5.14a) thus delivering on average twice as many minority ions as in the other NBI fuelled discharges and resulting in a faily high ^{3}He concentration ($\eta \cong 0.13$). However a serious impurity influx (mainly of carbon) increased the effective ionic charge ($Z_{eff} \cong 4.3$ for the time-slice considered), and culminated in a carbon bloom around 11-12 s. MHD activity before the carbon bloom is also present. This discharge has been nevertheless included in the analysis to estimate the extent of the yield reduction due to the instabilities present in the plasma.

After having estimated the fast ion energy content W_c, the total fusion power output P_{fus} has been calculated for these discharges by fixing the plasma parameters to their experimental values and letting the ^{3}He concentration vary. In order to reproduce the experiment as much as possible, for discharge JPN 23399 the effective ionic charge has been set to Z_{eff}=4.3 with carbon as main impurity (Z_{imp}=6), while for the other two shots the values Z_{eff}=1.9 (JPN 23438) and Z_{eff}=1.7 (JPN 23489) with Z_{imp}=4 (beryllium) for both discharges have been chosen. The results, reported in Fig.5.15, agree fairly well with the experiment. The values of the minority concentration η indicated in the picture are those correspondent to the values of P_{fus} nearest to the experiment. A cross-check with the experimental η values given by the NPA diagnostic shows reasonable agreement (see Table 5.2). As far as JPN 23399 is concerned, the estimated value of P_{fus}=0.076 MW represents the fusion power that would have been obtained were MHD activity and carbon influx absent.

Table 5.2. Plasma parameters and numerical results

	JPN 23399	JPN 23438	JPN 23489
time-slice t_0 s	10.6	11	9.1
RF power (MW)	12.7	8.7	11.0
central electron density (10^{19} m^{-3})	2.45	2.75	2.21
central electron temperature (keV)	11.38	10.0	9.85
Z_{eff}	4.3	1.9	1.7
main plasma impurity	carbon	beryllium	beryllium
minority concentration (NPA)	0.13	0.04	0.10
minority concentration (PHANTOM)	0.15	0.03	0.11
measured fast ion energy W_f (MJ)	1.23	1.06	1.14
calculated fast ion energy W_c (MJ)	1.26	1.0	1.12
measured total fusion power (MW)	0.056	0.106	0.133
calculated total fusion power (MW)	0.076	0.102	0.132

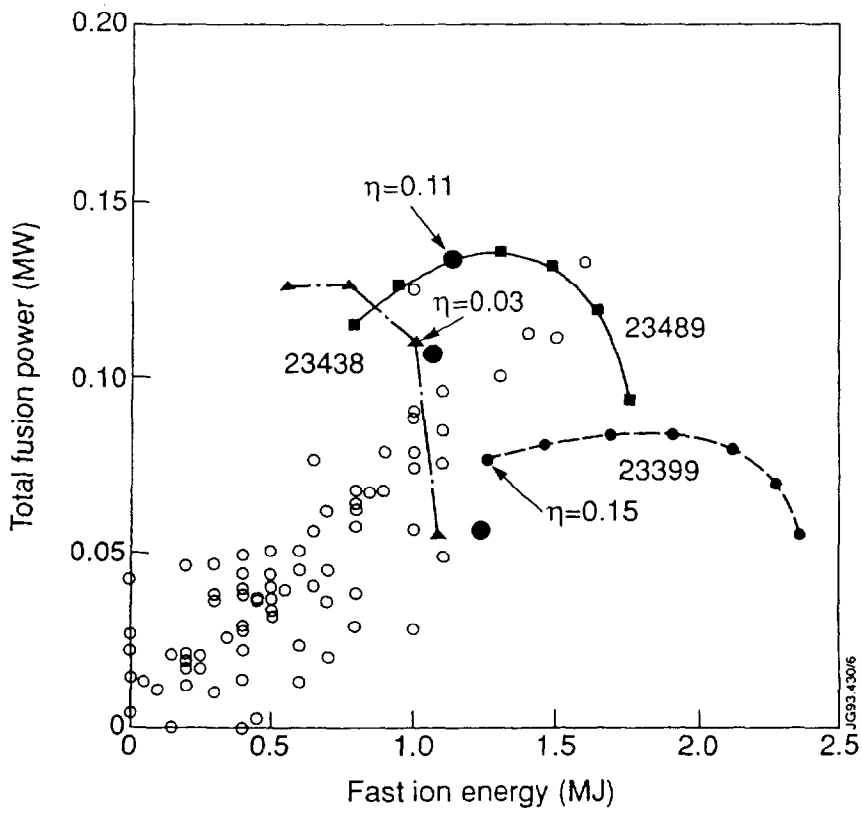

Figure 5.15 Comparison between the results of the simulations and the experiment.

5.4 Applications to ITER

The production of RF induced fusion reactions in a (^{3}He)D plasma on a device such as ITER could be important for a number of reasons. First of all, if sufficient α particles are generated the relevant diagnostics could be calibrated before introducing tritium into the device. Secondly, studies on α particle confinement and the related problem of ash removal on a reactor scale can be directly studied. It is therefore essential to establish the best possible scenarios to be used in the experiments. To this effect, the analysis carried out in the present Chapter offers a versatile tool to optimize the total ^{3}He-D fusion yield.

The main parameters used in the present study are those relative to the EDA (Engineering Design Activity) phase of the ITER Project as reported in Table 5.3. Electron density and temperature, Z_{eff} and RF power are varied accordingly to the different scenarios and are reported in Table 5.4.

The analysis articulates as follows. Firstly the total fusion power is optimized with respect to minority concentration, electron density and temperature and Z_{eff} for a

fixed value of the RF coupled power and of the half-width w of the RF profile. The results from both orbit and zero-orbit models are compared. Then the RF power is increased, and the gain in P_{fus} is calculated for the most favourable scenarios. The variations of P_{fus} with w and the resonance position are also studied. Lastly, the results are summarized in an experimental proposal.

Table 5.3. ITER EDA and CDA* - Main parameters [5.10].

Parameters	EDA	CDA
major radius (m)	7.75	6
minor radius (m)	2.8	2.15
aspect ratio	2.77	2.79
elongation	1.6	1.98
triangularity	0.25	0.38
plasma volume (m^3)	1908	1100
plasma surface (m^2)	1335	800
plasma current (MA)	25	22
safety factor	3	3
toroidal field on axis (T)	6	4.85
maximum toroidal field (T)	12.5	11.2
number of toroidal coils	24	16
maximum poloidal field (T)	13	13.5

***Concept Design Activity**

RF heating is at first applied on-axis with an half-width of w=0.30m for the parameters relative to the seven scenarios of Table 5.4. The optimum fusion yields thus obtained with and without orbit effects are compared in Table 5.5. As expected the two models do not give results significantly different, due to the very high densities involved. At P_{RF}=50 MW about 5 MW of fusion power can be produced, although with a low central electron density. If both n_{e0} and P_{RF} are increased (scenario 7), fusion power in excess of 10 MW can be produced at minority concentrations high enough to guarantee sufficient wave damping.

Table 5.4. Parameters for ITER Scenarios

scenario	P_{RF} (MW)	T_{e0} (keV)	n_{e0} (10^{20} m^{-3})	Z_{eff}
1	50	19	1.38	1.45
2	50	21	1.38	1.45
3	50	21	2.77	1.54
4	50	30	0.9	1.45
5	80	30	0.9	1.45
6	80	30	1.38	1.45
7	100	30	1.38	1.45

When RF heating is applied off-axis, or the half-width w of the RF power density profile is increased, the fusion yield decreases. In both cases this is due to the decreased power density coupled to the minority ions.

Table 5.5. Results of simulations

scenario	η	P_{fus} orbit (MW)	P_{fus} zero-orb. (MW)
1	0.015	3.42	3.45
2	0.015	3.78	3.79
3	0.004	3.77	3.79
4	0.05	5.33	5.29
5	0.08	8.23	8.15
6	0.04	8.73	8.71
7	0.05	10.77	10.75

The results of all the simulations are summarized in Fig.5.17, where the optimized P_{fus} is plotted against $P_{RF}T_{e0}^{3/2}$: the fusion yield scales linearly with this product even at such high RF power, in good agreement with the proof given in Appendix B. The scatter in the data is determined by the different densities used and (in one case) to the different Z_{eff}.

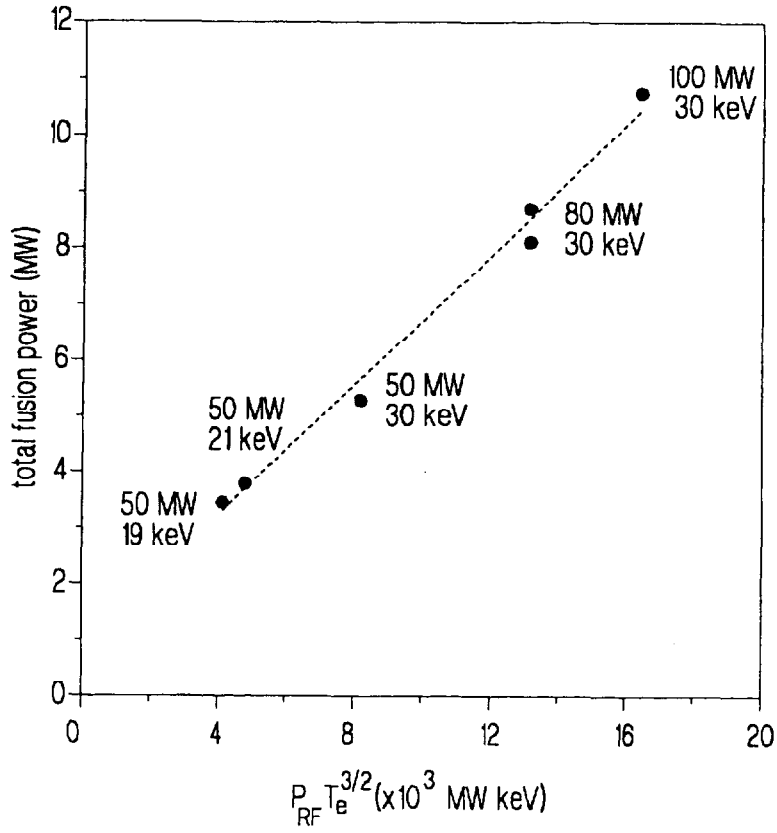

Figure 5.16 Summary of fusion yield simulations for ITER.

It can thus be concluded that it is possible to produce fusion power of order of 10 MW in a (^{3}He)D ITER plasma with densities around 10^{20} m^{-3} and temperatures of 30 keV with RF power of 80 MW, provided that an adequate wave damping can be

achieved (with minority fractions around 3-8%), and that the power is deposited within 30 cm of the plasma centre.

5.5 Summary and conclusions

In this Chapter the orbit model has been applied to estimate the fusion yield in ICRF heated (^{3}He)D plasmas. The analysis has been carried out on the basis of a series of experiments made at the end of the 1990 experimental campaign on JET. The conclusions that can be drawn from the analysis are the following.

Firstly, the calculations carried out without orbit effects and using a completely anisotropic distribution function of the minority ions have been shown to underestimate the fusion yield by about 20%.

Secondly, the introduction of orbit effects does not alter significantly the magnitude of the fusion yield. However, the calculation of the fast ion energy is greatly influenced by orbits, and extremely sensitive to variations in the minority concentration. As a result, while at high minority density the two models coincide, at low η they are critically different.

The analysis has been extended to include the simulation of three discharges in steady-state conditions. The results agree fairly well with the experiment, even when a discharge in far from ideal conditions (presence of MHD activity, followed by a carbon bloom) is considered.

Lastly, the production of fusion power in a (^{3}He)D plasma has been extrapolated for a reactor scale device like ITER. Experimental parameters have been determined such that fusion power in excess of 9 MW can be produced.

5.6 References

1. J. Jacquinot, G. Sadler and the JET Team, Fus. Tech. **21** (1992), 2254.

2. T.H. Stix, Nucl. Fusion **15** (1975), 737.

3. J. Jacquinot and Y. Lapierre, Proc. 2nd Joint Grenoble-Varenna Int. Symp., Como, Italy (1980), Vol. I, p. 541.

4. The JET Team (presented by J. Jacquinot), JET Report P(91)20.

5. M. Bureš et *al.*, Plasma Phys. and Controlled Fus. **33** (1991), 937.

6. G. Sadler et *al.*, Fusion Tech. **18** (1990), 556.

7. G. Sadler, private communication.

8. D. Anderson, L.-G. Eriksson and M. Lisak, Plasma Phys. and Controlled Fusion **29**(7) (1987), 891.

9. L.-O. Pekkari et *al.*, Nucl. Fusion **23** (1983), 781.

10. P.H. Rebut, report presented at the 2nd Meeting of the Technological Advisory Committee TAC 2 (1993).

6.0 Orbit Effects and Heat Transport

In the present Chapter the effect that minority ion orbits have on the heat transport properties of a two-component plasma during ICRF heating experiments on JET is investigated.

The Chapter is divided into three main Sections. In the first one the method used to derive the heat diffusion coefficient χ is presented. In the second Section it is shown that orbit-induced modification of the electron power deposition profile in a (H)D plasma has important consequences on the values that χ assumes in the plasma centre [6.01].

Lastly the third Section deals with the problem of the saturation of the central electron temperature at large values of the RF coupled power per particle P_{RF} / n_{e0} obtained during high power ICRF heating experiments on JET [6.02,6.03]. The analysis is carried out on the same series of (^{3}He)D high fusion yield discharges already considered in Chapter 5. The heat diffusivity profile is derived for a representative subgroup of discharges. It is shown that, within error bars, they all share the same transport properties. An average diffusivity $\overline{\chi}$ is then estimated, and theoretical curves of $T_e(0)$ as a function of P_{RF} / n_{e0} are calculated for different minority concentrations and a fixed electron density profile. At first $\overline{\chi}$ is taken to be independent of temperature, so that the role of large orbits of ^{3}He ions can be singled out. After that, dependence of χ on $T_e(0)$ is determined to be linear, a new temperature dependent $\overline{\chi}$ is estimated and the results of a new series of simulations are compared with both the previous results and with the experiment.

6.1 Heat Transport in JET Plasmas

During the 1991-92 campaign a number of experiments were made on JET to understand better the transport properties of L-mode plasmas. One of them, using

on/off-axis ICRF heating following pellet injection [6.04,6.05] aimed at establishing whether or not the heat flux Q can be described by a diffusion equation of the type,

$$Q = -\chi(T,\nabla T) n \nabla T - Q_{pinch} \,, \tag{6.1}$$

and investigating the behaviour of Eq.(6.1) for a wide range of $n\nabla T$ values. Pellet injection was used to study the effect of positive and negative values of $-n\nabla T$ in one pulse while at the same time suppressing any unwanted orbit effects.

Three types of discharges were used: on-axis, off-axis ICRF heating and a combination of both of them, with equal amounts of RF power coupled to the plasma. The response of the electron temperature profile is evident in Fig.6.1, where $T_e(r)$ for both on-axis and off-axis ICRF is compared at three different times [6.06]. In the outer plasma region they are very similar (as they should), while in the central region $T_e(r)$ for the off-axis case remains markedly hollow for a long period of time, and only after two-three seconds from the beginning of the RF heating (t=3.8s in the figure) it begins to show a slight peakedness in the centre [6.06].

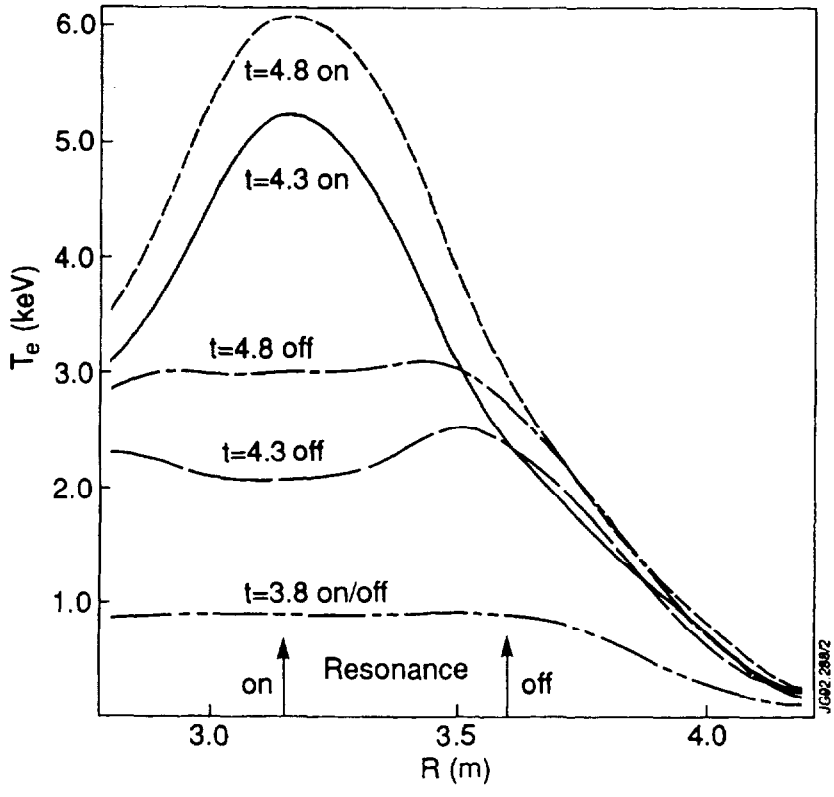

Figure 6.1 JET transport experiment. Electron temperature profile at three different times for the on-axis, off-axis and mixed ICRF heated discharges of [6.06] (courtesy of J.G. Cordey).

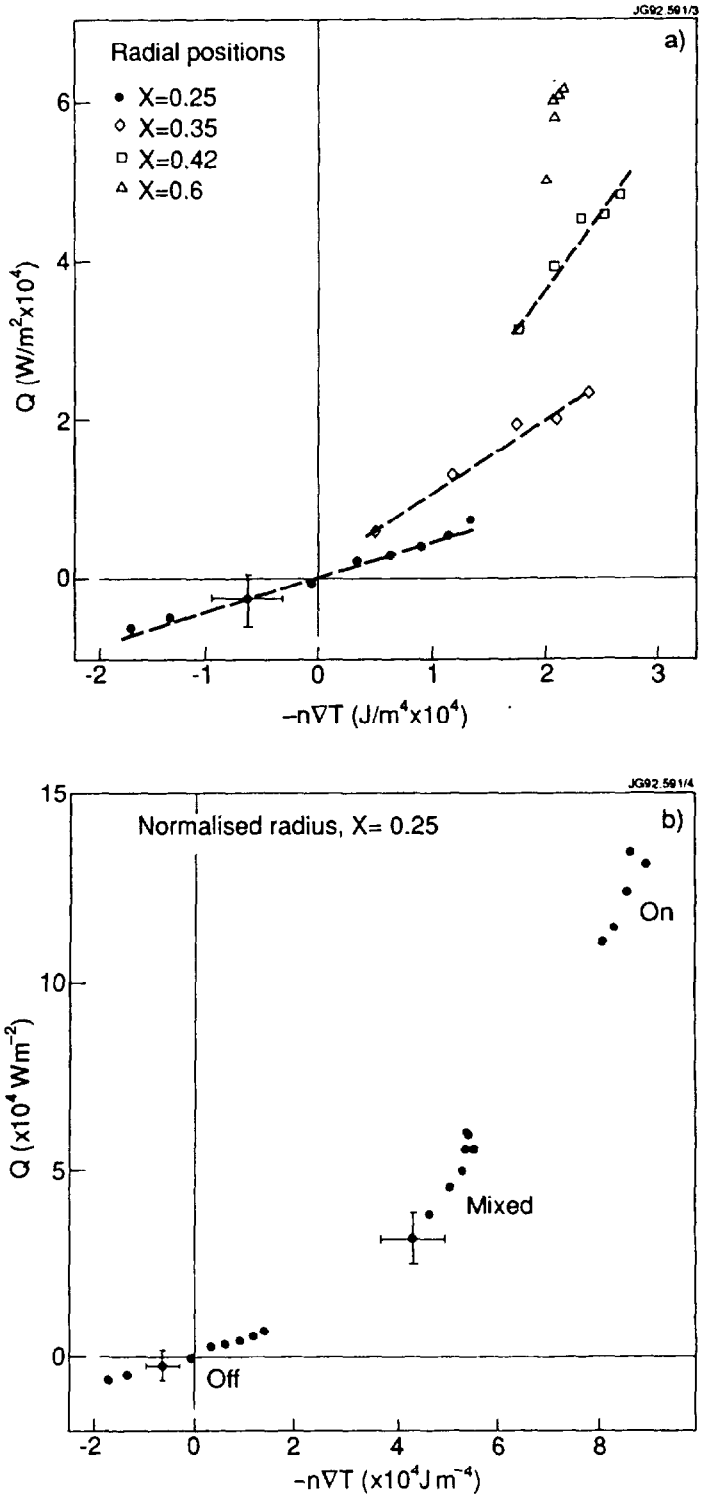

Figure 6.2 Heat flux vs. $-n\nabla T_e$ for the JET transport experiments.

a) The total heat flux Q is plotted against $-n\nabla T_e$ for the off-axis ICRF discharge at different values of the flux surface radius ρ.

b) The total heat flux Q is plotted against $-n\nabla T_e$ for the on-axis, off-axis and mixed ICRF heating discharges at ρ=0.25 (courtesy of J.G. Cordey).

The results of the experiment are summarised in Fig.6.2, where Q is plotted against $-n\nabla T$ at different radii. Fig.6.2a shows that within experimental uncertainties the heat flux in the plasma centre for the case of off-axis heating is approximately zero when $-n\nabla T$ is zero, consistent with the hypothesis of a negligible heat pinch term. Note also that the slope of the curve is steeper at higher radii, meaning that χ increases with radius. Fig.6.2b instead shows the increase of Q as a function of $-n\nabla T$ at a fixed normalised radius nearest to the centre (ρ=0.25). From Fig.6.2b it is clear that Q increases roughly parabolically with $n\nabla T$, suggesting that χ increases linearly with $|\nabla T|$ (the density does not vary appreciably). Dependence of χ on T as well is not ruled out, although in [6.06] it is argued that in this case χ should be a strong function of temperature.

On the basis of these results, in the analysis that follows the heat pinch term in Eq.(6.1) will be neglected.

6.1.1 The heat diffusivity coefficient

Experiments in which the heat flux Q is plotted for different $n\nabla T$ values have been described in the previous Section. A complementary approach, adopted in this and the next Sections, assumes that, given the profiles of the measured quantities like density and temperature, the heat diffusivity χ can be estimated by deriving the heat flux $Q(\rho)$ from the RF heating profile.

The orbit model of Chapter 4 has been derived assuming flux surface averaged quantities in cylindrical geometry. Therefore the heat diffusivity can be derived from the flux surface averaged diffusion equation in cylindrical co-ordinates,

$$e\rho n_e(\rho)\chi_{eff}(\rho)\frac{dT_e}{d\rho} = -Q(\rho)\ , \tag{6.2}$$

where $\rho = r/a_0$, n_e and T_e are the electron density and temperature profiles, respectively, while,

$$\begin{aligned} Q(\rho) &= Q_{RF}(\rho) + Q_{\Omega}(\rho) - Q_{rad}(\rho) \\ &= \int_0^{\rho} d\rho' \rho' [P_{RF}(\rho') + P_{\Omega}(\rho') - P_{rad}(\rho')]\ , \end{aligned} \tag{6.3}$$

is the local heat flux, measured in Wm^{-2}. In Eq.(6.3) P_{RF} is the RF power coupled to the plasma, while P_{Ω} and P_{rad} are the ohmic heating profile and the profile of the power lost through radiation, respectively. An *effective* heat diffusivity is used in Eq.(6.2), defined as,

$$\chi_{eff}(\rho) = -\frac{Q(\rho)}{2n_e \nabla T_e} \,. \tag{6.4}$$

Eq.(6.2) and Def.(6.4) hold assuming that $T_e \cong T_i$ locally, so that $\nabla T_e \cong \nabla T_i$ and the equipartition heat flux Q_{ei} can be neglected [6.7].

The calculation of the heat flux $Q(\rho)$ is a key feature in the present analysis, and must be dealt with care in order to distinguish the real contribution of large orbits to χ_{eff}. The power deposition profiles used in Eq.(6.3) are derived from various sources. Particularly important is the RF term, which can be written as,

$$P_{RF}(\rho) = P_{ce}(\rho) + P_{ci}(\rho) + P_{de}(\rho) + P_{II}(\rho) \,, \tag{6.5}$$

where P_{ce}, P_{ci} are the profiles of the power transferred through collisions from the minority ions to electrons and background ions. The term P_{de} instead refers to the power damped on the electrons through a combination of mode conversion, TTMP and ELD (collectively called direct electron heating, see also Chapter 3). Lastly, P_{II} is the power absorbed by the background ions through second harmonic heating.

Only the first term in Eq.(6.5) can be significantly influenced by large orbits, and is therefore calculated using the orbit model. The second term, P_{ci}, can be calculated using either the orbit or the zero-orbit model with no substantial difference. For comparison purposes, however, P_{ce} and P_{ci} will be calculated using also a zero-orbit (Stix) model. The contribution to plasma heating from P_{de} and P_{II} must be obtained independently. For this reason use is made here of the code PION-T [6.08]. This code uses the proper solution of the dispersion relation of the fast wave in a two-component plasma to solve the time-dependent pitch-angle averaged Fokker-Planck equation and calculate all the terms in Eq.(6.5) as a function of time and flux surface radius. This code works in toroidal geometry, so that the plasma elongation must be taken into account when using these profiles. Also, PION-T does *not* include orbit effects. As an alternative, when second harmonic heating can be neglected, a narrow Gaussian profile (w=0.26-0.30 m) can be used to good effect to model the contribution of direct electron heating.

The ohmic contribution to the heat flux $Q_\Omega = E_\phi J_\phi$ is calculated by assuming $\nabla \times \boldsymbol{E} = 0$, $J_\phi \cong E_\phi / \eta$, with η neoclassical resistivity, and $E_\phi = V_o / 2\pi R$, with V_0 loop voltage at the plasma edge and $R = R_0 + r$ [6.09]. A consistency check is routinely carried out to make sure that integration over the plasma volume gives the measured total dissipated power.

The profile of the power lost through radiative processes should in principle be obtained by Abel inversion of bolometer data. In practice it is difficult to obtain a reliable profile using this method, and usually a standard radial profile is preferred to describe the power losses through radiation under "normal" circumstances [6.10]. By "normal" one means a steady-state plasma with a tolerable level of impurities and $Z_{eff} \cong 2$.

To summarise, the contributions to $P_{RF}(\rho)$ which will be used in the next Sections are,

P_{ce}, P_{ci}	PHANTOM code (orbits)
	Stix code (no orbits)
	PION-T code (no orbits)
P_{de}	PION-T code
	Gaussian profile
P_{II}	PION-T code (when required)

6.2 Local transport with on/off-axis ICRF heating

Comparison of on/off-axis ICRF heated discharges provides a useful way to measure the response of local transport to changes in the power deposition profile. To this effect two 2 MA limiter (H)D discharges have been analysed [6.11],

- JPN 24665 (2.8 T) - ICRF resonance on the magnetic axis;
- JPN 25651 (2.5 T) - ICRF resonance on the inboard q=1 surface (ΔR=-0.38 m), with +90° phased antennas.

For both cases density, input power, effective ionic charge Z_{eff} and minority concentration are very similar. As usual the analysis is applied to steady-state, sawtooth-free phases of the discharge. At the time-slice considered, the electron temperature profile is peaked even in the off-axis case (see Fig.6.3 and Table 6.1 for the values).

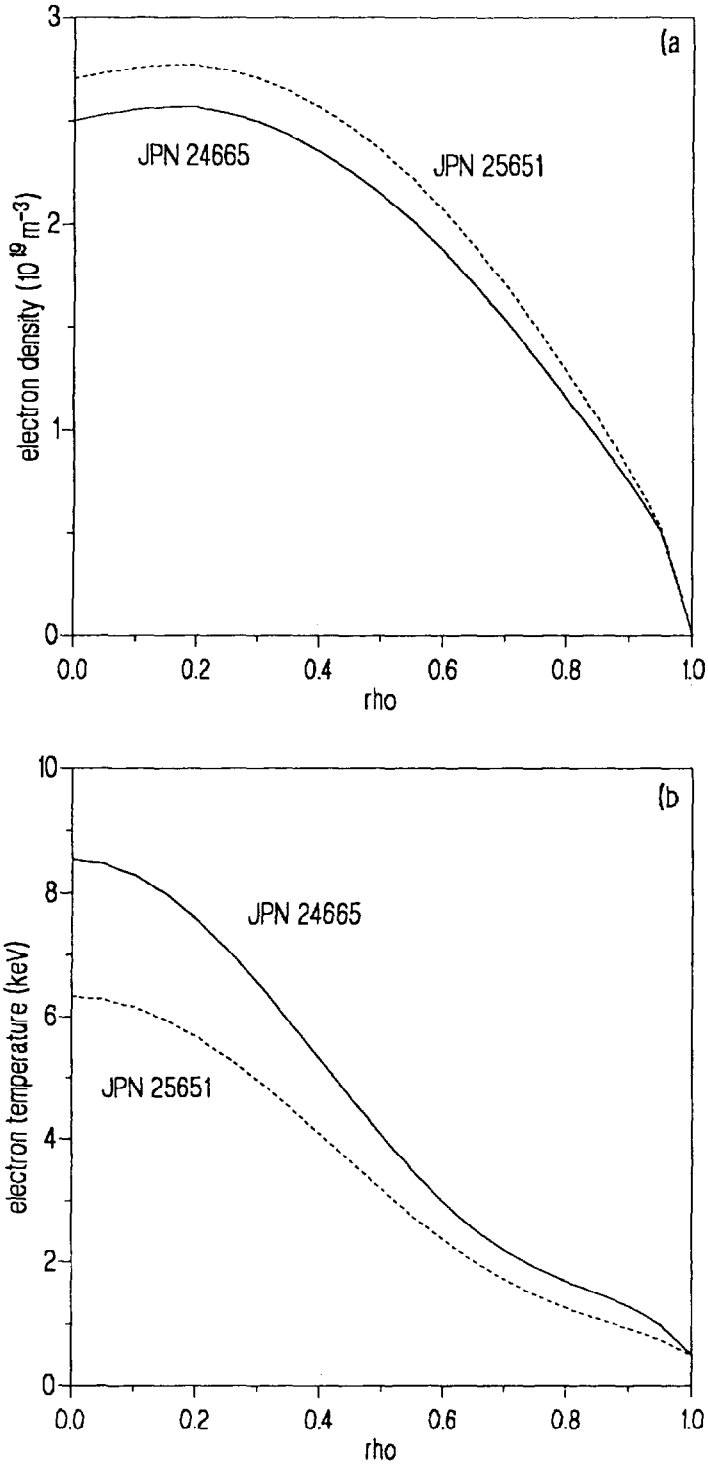

Figure 6.3 Experimental curves for on\off-axis ICRF discharges 24665 and 25651.
a) electron density profiles;
b) electron temperature profiles.

Table 6.1 Plasma parameters

	JPN 24665	JPN 25651
central electron temperature (keV)	8.5	6.7
central electron density (10^{19} m^{-3})	2.52	2.7
RF power (MW)	5.12	4.7
distance from resonance (m)	0	-0.38
minority fraction	0.07	0.05
$\chi_{eff}(0)$ (orbit model)	0.706	0.2563

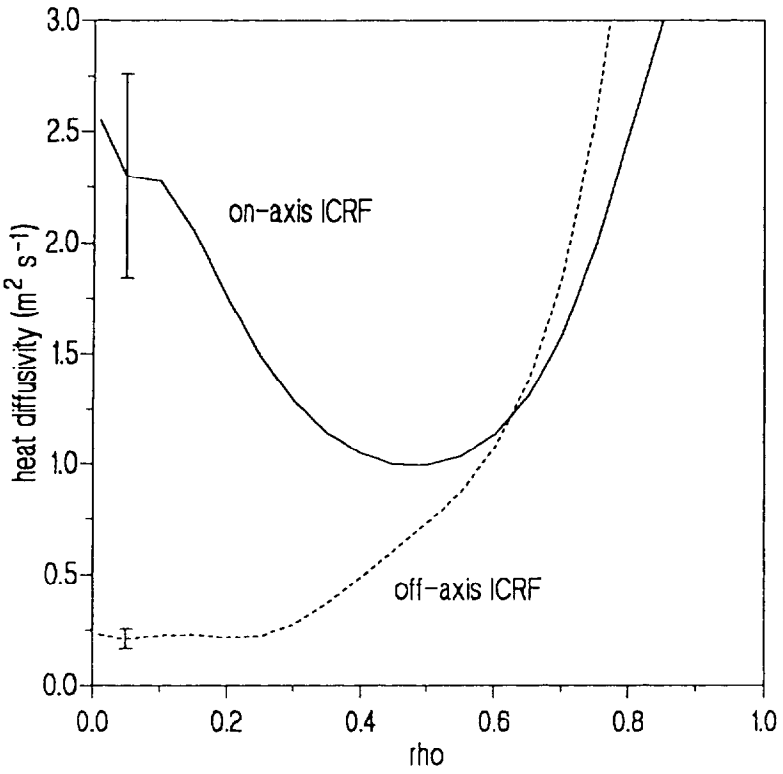

Figure 6.4 **Zero-orbit effective heat diffusivity.** χ_{eff} has been deduced with non orbit-corrected heating profiles from on-axis (JPN 24665, continuous curve) and off-axis ICRF (JPN 25651, dashed curve) [6.01].

An independent transport code (FALCON) [6.10] used the power deposition profiles calculated by PION-T to estimate χ_{eff} for the two cases. The results, shown in Fig.6.4, indicate that the local effective diffusivity in the centre for the on-axis case is one order of magnitude higher than for the off-axis discharge. Moreover, the fast ion energy predicted by PION-T gives results too high by a factor of two for the on-axis

case [6.11]. Broadening of the heating profile seems to be consistent with the measurement of the fast ion energy content [6.12].

The orbit model provides a straightforward solution to this apparent discrepancy. With a minority fraction $\eta = n_H / n_{e0}$ of 7% as measured with the Neutral Particle Analyser, the orbit fast ion energy for the on-axis discharge 24665 is estimated to be 1 MJ, compared with the measured value of 1.3±0.26 MJ. With this input the electron and ion power deposition profiles are then calculated, and the results used to estimate χ_{eff}.

In order to compare most effectively the results, the same flux surface averaged electron density and temperature profiles of [6.11] have been used. Care has been taken to input the same profiles for ohmic, second harmonic and direct electron heating. This way any effects due to orbit broadening of the electron heating profile P_{ce} can be identified unambiguously.

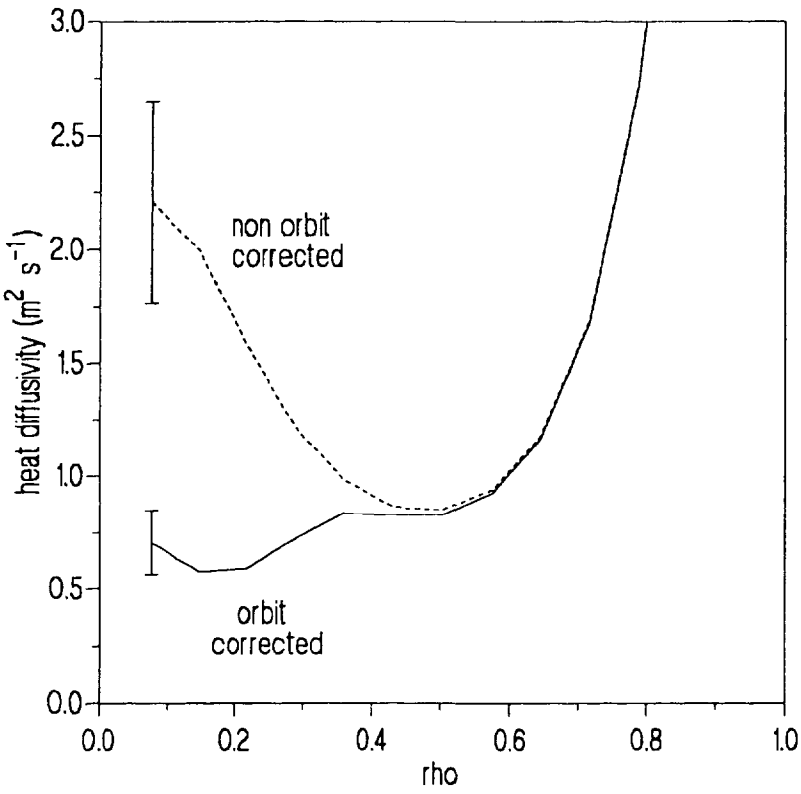

Figure 6.5 Effective heat diffusivity for the on-axis ICRF discharge 24665. The χ_{eff} profile has been calculate using the diffusion equation in cylindrical co-ordinates Eq.(6.4). Both non-orbit corrected (dashed curve) and orbit corrected (continuous curve) heating profiles have been used [6.01].

The results are shown in Fig.6.5. First the χ_{eff} profile of [6.11] has been successfully recreated using in Eq.(6.5) the collisional heating profiles given by both PION-T and the zero-orbit (Stix) model, thus providing a reliable - and independent - baseline. Use of the orbit P_{ce} gives entirely different results: as it can be seen in Fig.6.5, the orbit χ_{eff} in the centre is lower than the zero-orbit one by a factor of four. The value of 0.7 m^2/s is now twice that given by the off-axis heating discharge, instead of a factor of ten [6.01].

It is worth noting that cases similar to that described above have been recently observed in DIII-D with both on/off-axis NBI [6.13] and ECH [6.14]. In particular, in [6.13] two otherwise identical H-mode NBI heated discharges are characterised by an effective heat diffusivity which, in the on-axis case, is roughly a factor of ten higher than during off-axis heating, suggesting that χ_{eff} is sensitive to changes in the heating profile. The results of the present analysis support this interpretation.

This feature has profound consequences on the transport properties of auxiliary heated plasmas, implying that broadening of the heating profile can be partially responsible for the saturation of the central electron temperature at high values of the RF power per particle.

6.3 The electron temperature saturation

Early experiments using central ICRF heating on JET showed a linear increase of the electron temperature T_e with the coupled RF power per particle, P_{RF} / n_{e0} [6.15]. When however a wider range of P_{RF} / n_{e0} values was made available, it became clear that $T_e(0)$ grew only up to a certain point, beyond which it saturated. This effect, reported by different authors [6.02,6.03], is present using both H and ^{3}He minorities.

In this last Section the role of large minority ion orbits in the T_e saturation is investigated. The same series of high fusion yield (^{3}He)D discharges already discussed in Chapter 5 are considered, and use is made of the technique introduced in Section 6.1.1 to determine their transport properties. Two possibilities exist: the T_e saturation coulb be due to orbit effects alone or, in addition, a contribution could arise from a dependence of χ on T_e itself. The effect of large orbits is determined by estimating an average heat diffusivity $\overline{\chi}$ and using it to reconstruct the original T_{e0} curve with both the orbit model (through the PHANTOM code) and the zero-orbit Stix calculations. In this instance $\overline{\chi}$ is assumed independent of T_e, in order to single

out the orbit contribution. It is found that the data tend to saturate more strongly than this calculation predicts. The next step therefore consists in the analysis of a group of discharges, all belonging to the same experimental session,

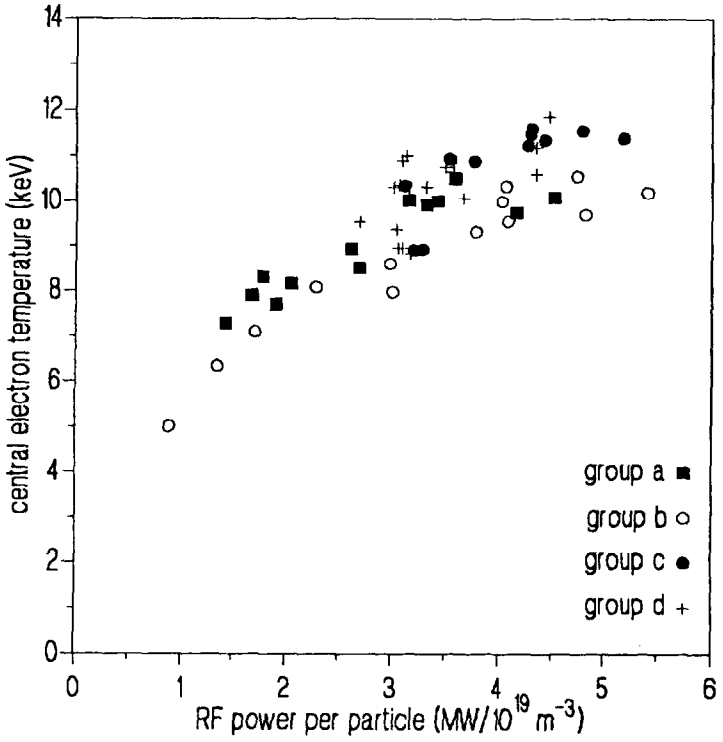

Figure 6.6 The T_{e0} saturation.

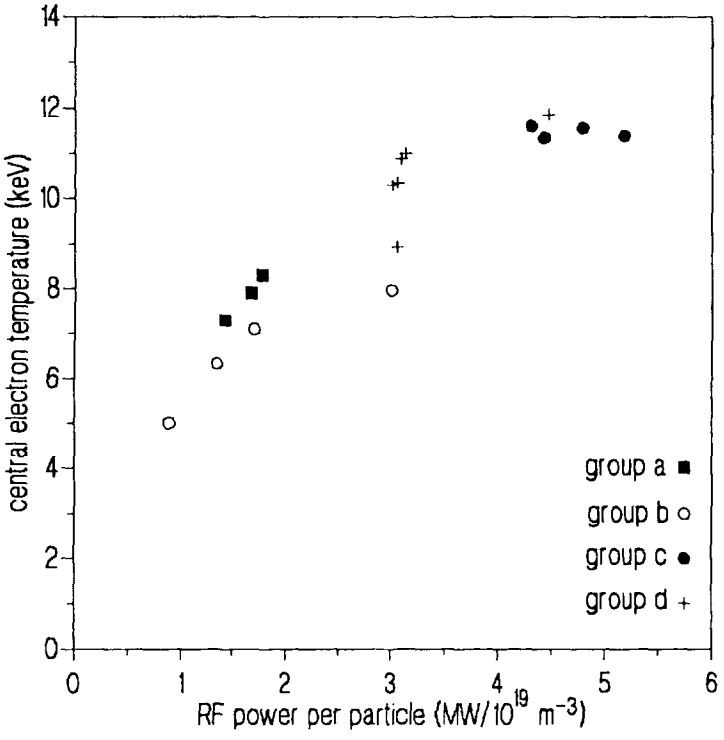

Figure 6.7 A sample of the data of Fig.6.6.

in order to determine a possible dependence of χ_{eff} on T_e itself. A new T_e dependent $\overline{\chi}$ is then estimated, and used to extrapolate the T_{e0} at high values of P_{RF} / n_{e0}.

6.3.1 Transport analysis

For the present analysis a series of (^{3}He)D double-null monster sawtooth discharges with plasma current I_p=3.5 MA, toroidal magnetic field B_ϕ=3.3 T and central ICRF heating have been considered, the properties of which are summarised in Section 5.1. The data-points have been selected during the monster phases of the discharge and in steady-state conditions of RF power, electron density and temperature, and stored energy, as well as at least one second after the NBI system (used for fuelling and diagnostic purposes) has been switched off. The time-slices thus selected belong to one of four experimental sessions, labelled for convenience groups a,b,c,d. The result of the selection procedure is shown in Fig.6.6, where the central electron temperature T_{e0} is plotted against P_{RF} / n_{e0} for the four groups. Fig.6.6 clearly

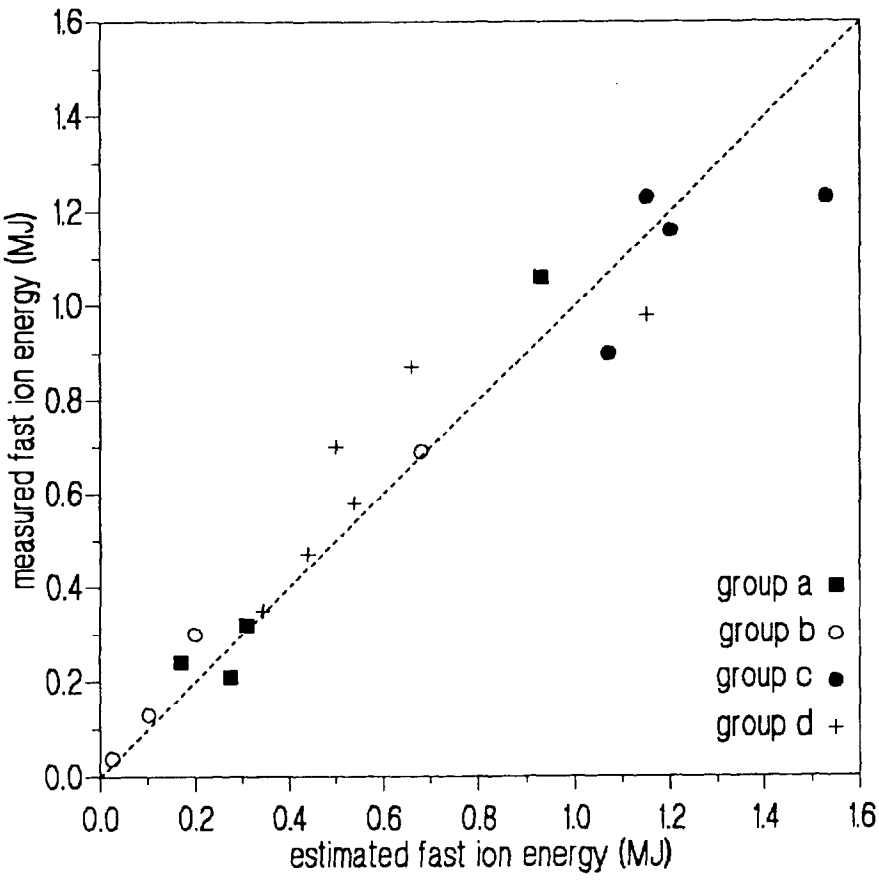

Figure 6.8 Fast ion energy. For the sample datapoints of Fig.6.7 the minority concentration is cross-checked by estimating the fast ion energy content and comparing it with its experimental counterpart.

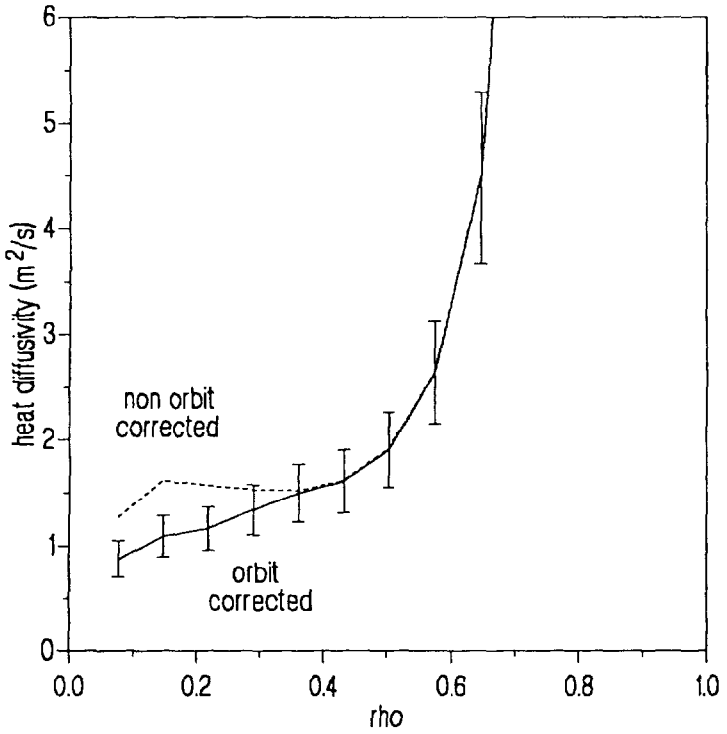

Figure 6.9 **Effective heat diffusivity profiles** for one on-axis ICRF heated discharge of the data-points of Fig.6.7 and calculated with and without orbit effects.

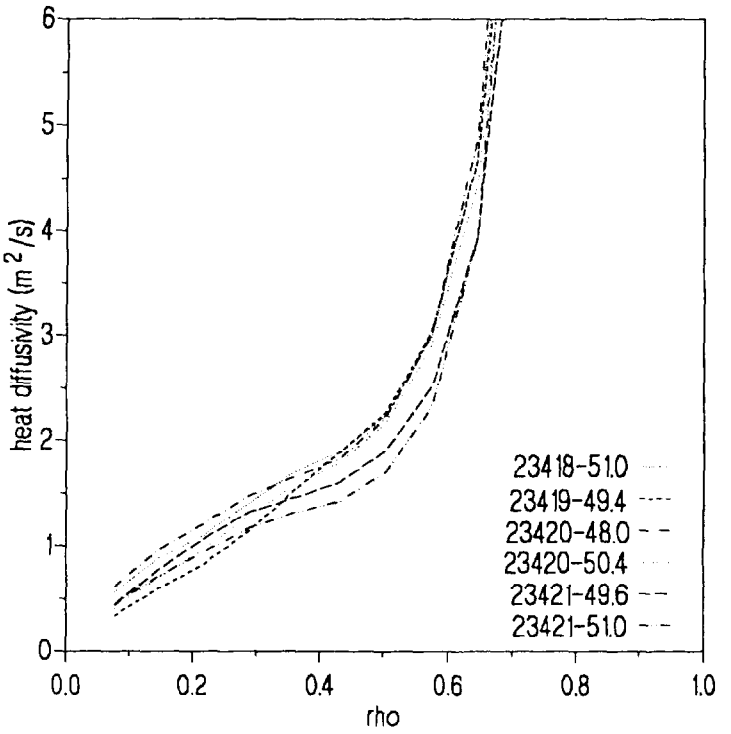

Figure 6.10 Effective heat diffusivity profiles for the discharges of group d.

shows the departure of T_{e0} from the linear scaling with P_{RF} / n_{e0}. Representative data-points from all the groups have been further selected from the database to represent the low, medium and high power cases, as shown in Fig.6.7. On these data the transport analysis will be focussed.

For all the data-points of Fig.6.7 the following procedure has been adopted. First the minority concentration $\eta = n_{He} / n_{e0}$ is determined from the particle flux measurements of the Neutral Particle Analyser and corrected to take into account impurity contamination (mainly beryllium) if necessary. Then, η is cross-checked by calculating the orbit fast ion energy W_c and comparing it with the experimental fast ion energy content, W_f as in Fig.6.8. Using the experimental profiles of density and temperature, together with other information like the amount of RF power damped on the ^{3}He ions (about 80% of the total coupled power, see Chapter 3), the collisional power deposition profiles are calculated using the orbit code PHANTOM or the zero-orbit model, as required.

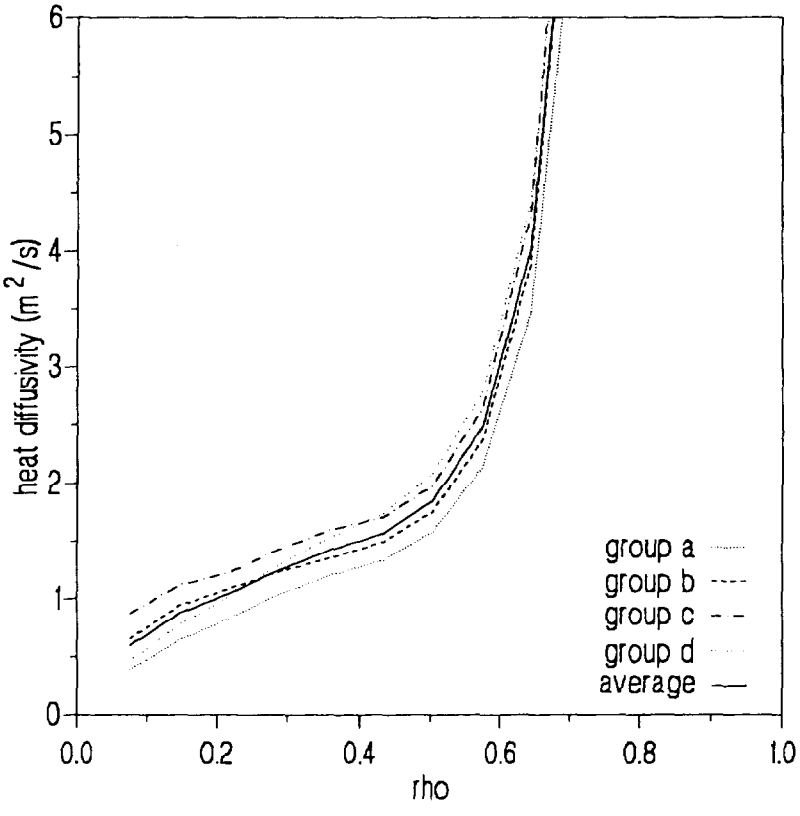

Figure 6.11 Average heat diffusivity for groups a,b,c,d.

The power deposition profiles thus obtained are now used in Eq.(6.4) to calculate the effective heat diffusivity, χ_{eff}. In Fig.6.9 two such profiles are compared,

calculated with and without orbit effects. Note that exclusion of orbit effects leads to overestimate χ_{eff} in the plasma core by about 40%. The difference in the centre between the two χ_{eff} profiles is not so big as in the case presented in Section 6.2, due to the fact that in this series of discharges the minority concentration is fairly high.

The profiles of the heat diffusivity obtained for the sample data-points of group d are shown in Fig.6.10. An overall heat diffusivity is then calculated for each group of discharges and an average χ profile, $\overline{\chi}$, is then deduced. Such $\overline{\chi}$ is shown in Fig.6.11 along with the average heat diffusivities for the four groups.

Using $\overline{\chi}$ it is now possible to calculate the central electron temperature. If orbit effects are the only cause responsible for the T_{e0} saturation, such a calculation should naturally reproduce the experimental data. If not, it is a clear indication that something else also contributes to the nonlinear scaling of T_{e0} with P_{RF} / n_{e0}. For this purpose, now Eq.(6.2) is solved for $T_e(\rho)$. A self-consistent method to estimate T_e is the following:

1. keep $\overline{\chi}$, n_e, P_{RF}, η constant;
2. calculate orbit heating profiles to estimate $Q(\rho)$;
3. solve Eq.(6.2) for T_e;
4. use the latest $T_e(\rho)$ to calculate the new (corrected) heating profiles;
5. go back to step 2.

The iteration continues until two successive temperature profiles do not differ by more than 5%.

With this method T_{e0} as a function of P_{RF} / n_{e0} has been calculated for increasing P_{RF} / n_{e0}, three different minority concentrations and a fixed electron density profile, with $n_{e0}=2.5\times10^{19}$ m^{-3}. The results are shown in Fig.6.12. The theoretical curves do not show as strong a saturation as the experimental data do. The role that minority ion orbits have is seen most clearly in Fig.6.13, where $T_e(0)$ is calculated with and without orbits as a function of P_{RF} / n_{e0} for η=0.09. While at low P_{RF} / n_{e0} there is little or no difference between the two models (due to the low power per particle available), they diverge more and more when the RF power is raised. It can then be concluded that if $\overline{\chi}$ does not depend explicitely on the temperature, the zero-orbit model predicts a linear increase of T_{e0} with the RF power per particle, while

large orbits affect the central electron temperature through the broadening of the electron heating profile.

Even though orbit effects have been proved to be an important contribution to the curvature of the T_{e0} curve, it is evident that they cannot be the only cause responsible for the temperature saturation. In fact when P_{RF} / n_{e0} is raised the orbit model still predicts an increase of T_{e0} higher than the data would suggest. Therefore in the next Section a further analysis is carried out to determine the dependence of χ_{eff} on the temperature, and explain the temperature saturation as the combined effect of large minority ion orbits and degradation of confinement (due to the application of auxiliary heating).

6.3.2 The $T_e(0)$ saturation explained

In the last Section large minority ion orbits have been identified to be partially responsible for the saturation of the central electron temperature at large values of the RF power per particle. This last Section shows that scaling of the heat diffusivity with the electron temperature itself (and possibly with ∇T_e as well) is also responsible for the observed temperature saturation.

To this end consider the series of data-points labelled group b in Fig.6.6. They are most suitable for the present analysis because they all belong to the same experimental session and because their P_{RF} / n_{e0} values extend over all the available range, from 0.9 to 5.5 MW/10^{19}m^{-3}, with electron temperatures ranging from 5 keV to 10.5 keV. To each of these discharges transport analysis is applied, and their χ_{eff} profiles are derived. In order to smooth out any misleading fluctuations of $\chi_{eff}(0)$, an average effective diffusivity coefficient in the plasma centre is defined as the arithmetic average between the first two χ_{eff} values, at a distance $\delta\rho = 0.071$ from each other. This central diffusivity $< \chi_{eff}(0) >$ is plotted against T_{e0} as in Fig.6.14a. The result indicates that $< \chi_{eff}(0) >$ clearly depends on the electron temperature but, due to the scatter in the data, it is impossible to decide immediately whether such a dependence is linear or not. The data have thus been least-square fitted to the following relations,

$$< \chi_{eff}(0) >= k_1 T_{e0}, \tag{6.6}$$

$$< \chi_{eff}(0) >= k_2 T_{e0}^{3/2} . \tag{6.7}$$

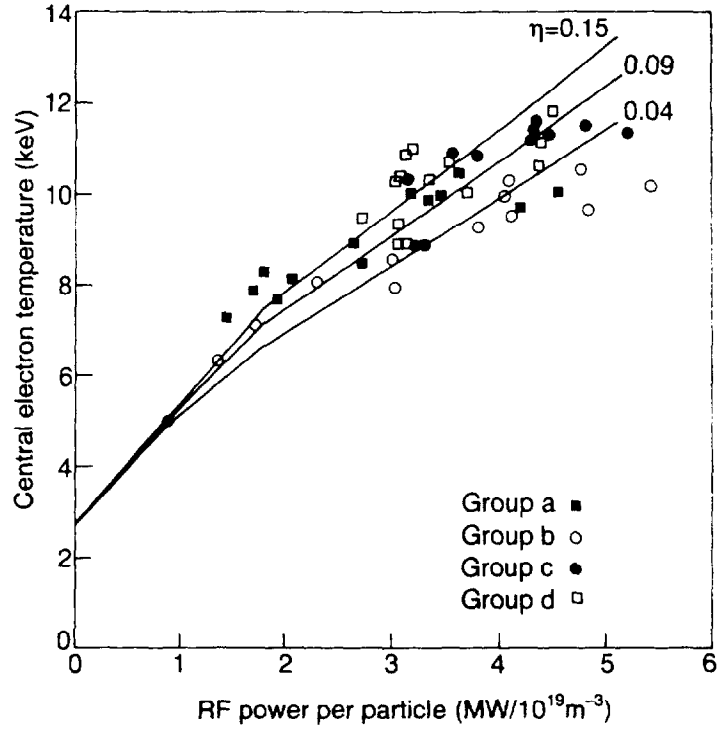

Figure 6.12 T_{e0} calculated with a T_e-independent heat diffusivity. The calculation has been carried out for three different minority concentrations, a fixed electron density profile and orbit-modified heating profiles.

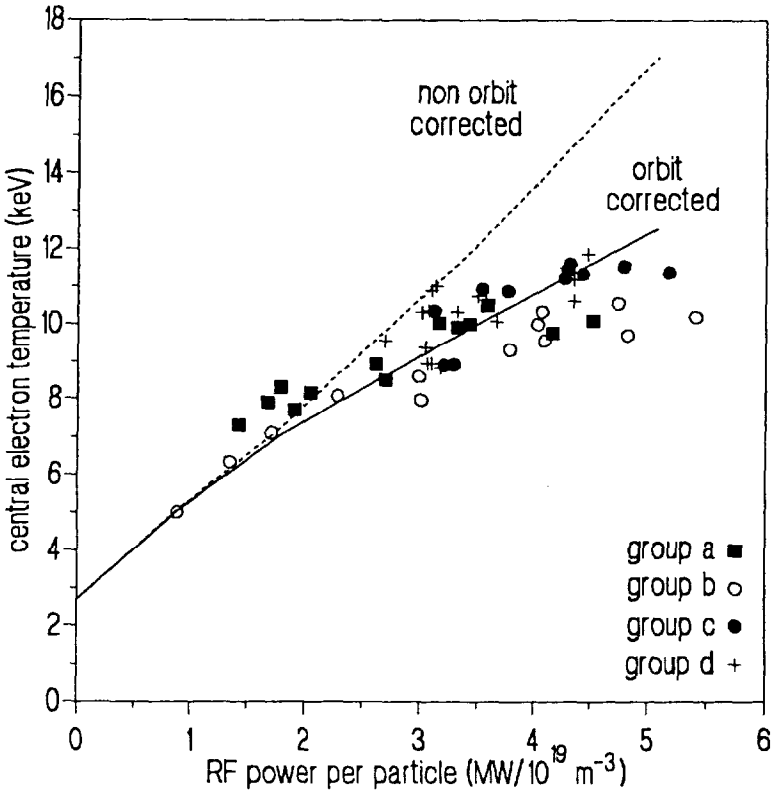

Figure 6.13 Orbit and zero-orbit (Stix) T_{e0} calculated with the T_e-independent heat diffusivity.

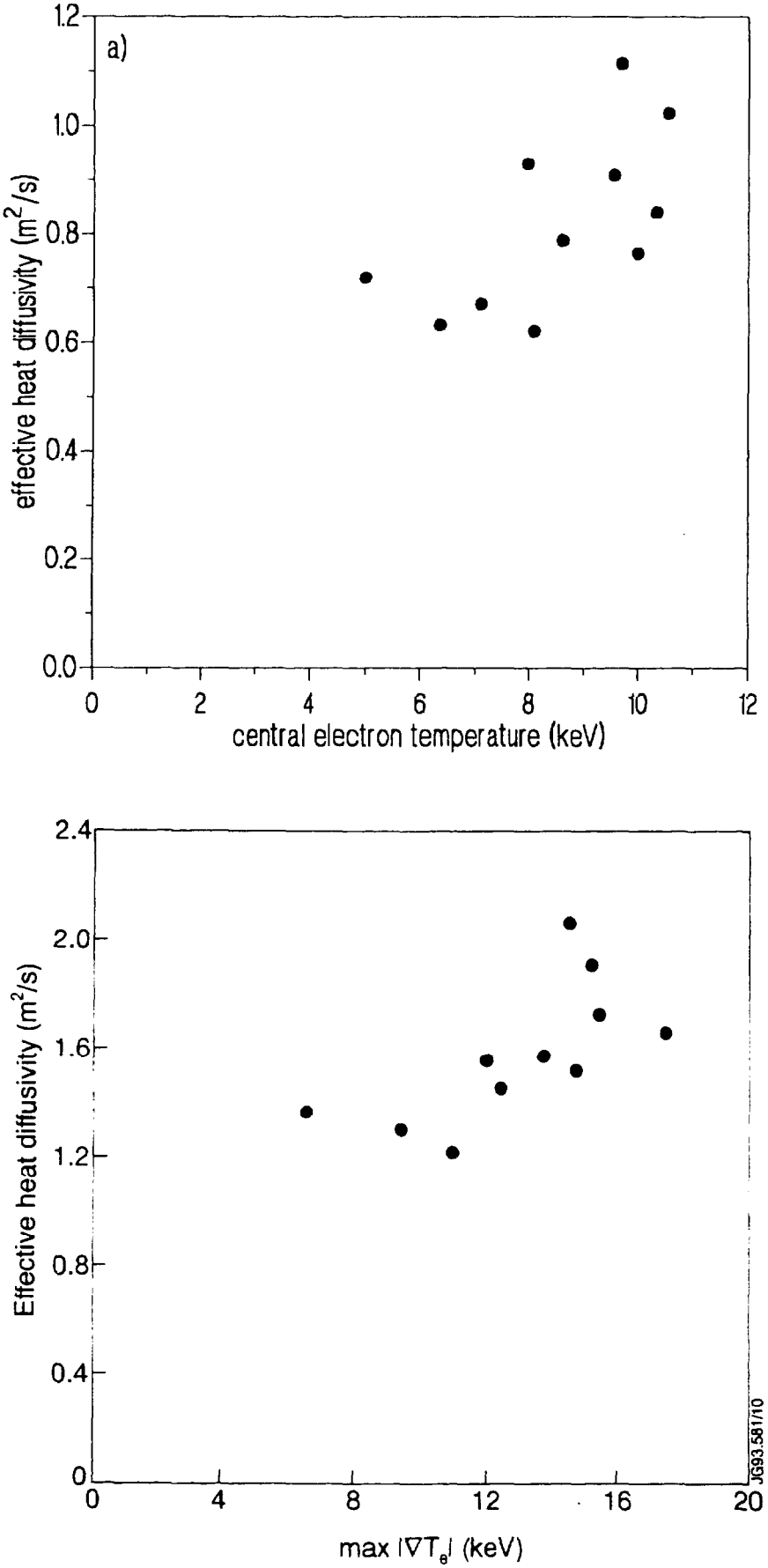

Figure 6.14 Linear increase of $<\chi_{eff}(0)>$ with T_e and max$|\nabla T_e|$.

Note that in this case a proper scaling analysis to determine whether the dependence of χ_{eff} on T_{e0} is of the Bohm or gyroBohm type cannot be carried out, because variations in the electron density introduce a further element of uncertainty. A χ^2-test of the two fittings shows that the linear dependence of χ_{eff} on the temperature converges, with $\chi^2_{lin} = 0.888$, while the nonlinear dependence ("gyroBohm-like") does not hold ($\chi^2_{nonlin} = 1.469$). A possible dependence of $< \chi_{eff}(0) >$ on $|\nabla T_e|$ in the plasma centre has also been sought after, but no definite proof could be obtained due to the difficulty to determine the gradient close to ρ=0. However if the maximum value of $|\nabla T_e|$ is considered, corresponding to ρ=0.36, then the effective heat diffusivity at that radius shows a definite linear increase with $\max|\nabla T_e|$ (see Fig.6.14b).

The conclusion that can be drawn is therefore the following: the effective heat diffusivity is temperature dependent, and it follows a linear scaling law of the type,

$$\chi_{eff} = \Delta\chi \, T_{e0} \,, \tag{6.8}$$

with fitting parameter $\Delta\chi = 9.52 \times 10^{-5}$ m^2 / s·eV. This is consistent with the results reported in [6.06] and discussed in Section 6.1.

With this evidence, a new $\overline{\chi}$ has been derived for the purpose of extrapolating to high RF powers per particle, namely,

$$\overline{\chi}(\rho, T_{e0}) = \overline{\chi}_{old}(\rho) + \Delta\chi \, (T_{e0} - T_e^*) \,, \tag{6.9}$$

where $\overline{\chi}_{old}(\rho)$ is the average temperature independent heat diffusivity derived in Section 6.3.1, while T_e^*=8.54 keV is the temperature correspondent to $\overline{\chi}_{old}(0)$ as deduced from Eq.(6.8). Eq.(6.9) can now be used to derive the new theoretical T_{e0}, solution of the integral equation,

$$T_{e0} - T_{e1} - \int_0^1 \frac{d\rho Q(\rho)}{2e\rho n_e(\rho)} [\overline{\chi}_{old}(\rho) + \Delta\chi(T_{e0} - T_e^*)]^{-1} = 0 \,, \tag{6.10}$$

where T_{e1} is the temperature at the plasma edge (ρ=1). Following the same steps described in Section 6.3.1 and using Eq.(6.10), a new orbit T_{e0} curve is obtained, function of P_{RF} / n_{e0}, as reported in Fig.6.15. As expected this model gives an excellent representation of the experimental data and can therefore be used with confidence to extrapolate to high RF power per particle. An example is given in Fig.6.15. In the case of P_{RF} / n_{e0}=7.2 MW/10^{19} m^{-3}, the central electron temperature

has reached a value of 12.3 keV, corresponding to a total fast ion energy of 3.1 MJ (far higher than any value of W_f considered so far). It is in this case interesting to calculate how much power would be required to obtain the same temperature if orbit effects were not present, i.e. if the tail temperature were somehow kept low enough or if the only heating mechanism were direct electron heating: 13 MW, compared with the 18 MW necessary to reach the same temperature in the presence of orbit effects. This means that in this case in the presence of finite orbit effects almost one third of the RF coupled power is lost from the plasma centre, contributing to heat the outer plasma regions. Here, due to the higher diffusivity, the resulting heat flux is rapidly channelled towards the edge.

It is difficult to remedy to such a situation from an experimental point of view. Complete suppression of orbits is in fact either impossible, or causes the onset of other, undesirable heating mechanisms. If in fact one tries to decrease the tail temperature by increasing the minority concentration and favour TTMP, heating of the background ions rapidly dominates, thus increasing the ion temperature instead.

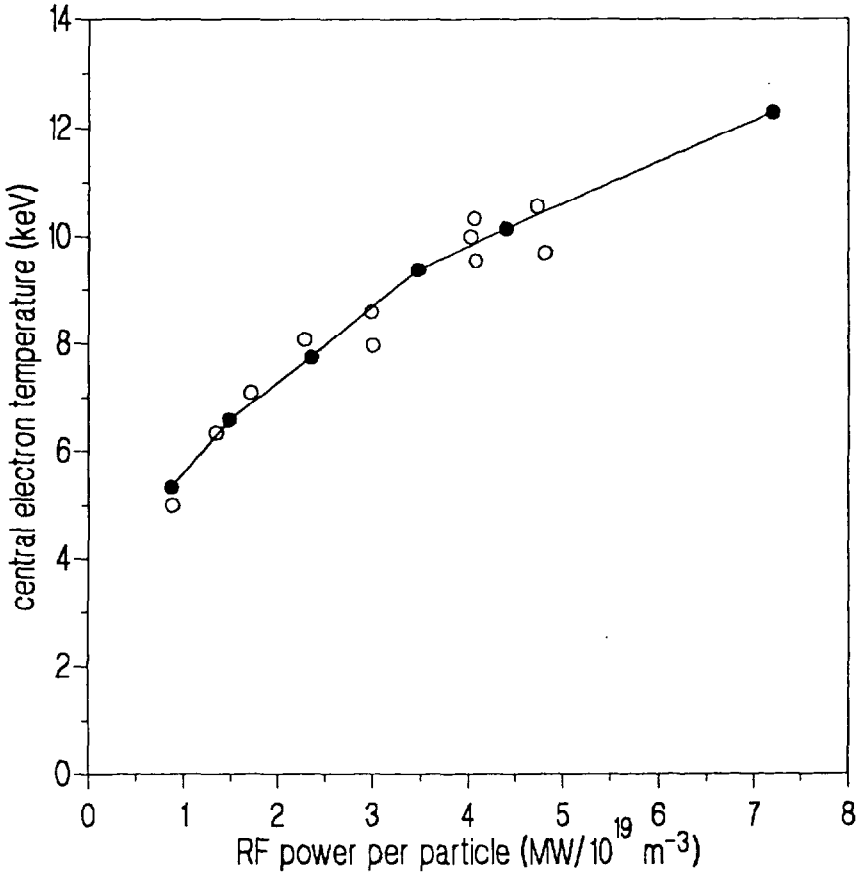

Figure 6.15 Extrapolation of T_{e0} to high RF power per particle using a T_e-dependent heat diffusivity calculated using orbit heating profiles.

A solution to this problem is offered by the following JET scenario. Consider a (^{3}He)H plasma, with parameters such that the ^{3}He cyclotron resonance lies in the plasma centre. Characteristic of such a plasma is that the cut-off of the hybrid layer (see Chapter 2) is localised roughly half-way between the resonance and the RF antennae, on the low field side. The launched fast wave is therefore reflected at the cut-off before being absorbed, and cavity modes are formed. If the Lower Hybrid launcher is used to produce initially a sufficiently high central electron temperature and thus increase the plasma β, then the fast wave can be absorbed through TTMP in the plasma centre without heating the minority ions. Such a scenario is here proposed as a high T_e experiment for the next JET experimental campaign.

6.4 Summary and conclusions

In the present Chapter the effects that large orbits of minority ions have on the energy transport in a two-component plasma have been investigated. At first a (H)D plasma has been considered. Analysis shows that orbits of H ions cannot be neglected in determining the heat diffusivity in the centre. Orbit-modified electron heating profiles have been proved to reduce the difference between the χ_{eff} profiles obtained from on/off-axis ICRF heated discharges and deduced from zero-orbit models [6.01].

When ^{3}He minority is considered, large orbits do not affect so deeply the evaluation of the heat diffusivity in the centre as in the H minority case, although there still is a difference in the $\chi_{eff}(0)$ values calculated with and without orbits. The existence of a suitable database allowed to apply the transport analysis developed in this Chapter to investigate the role of orbits in the saturation of the central electron temperature at high values of P_{RF}/n_{e0} for a (^{3}He)D plasma. All the discharges considered belong to the same experiment, so it came as no real surprise that they resulted to share the same heat transport properties. An average diffusivity has thus been derived, at first independent of T_e, with which it has been possible to check whether the curvature of the T_{e0} curve is due exlusively to orbits or not. With the zero orbit Stix model the central electron temperature is found to scale linearly with P_{RF}/n_{e0}, whereas when orbits are considered there is a saturation, but somewhat less than in the experiment. Thus the results indicate that orbits alone cannot fully explain the T_{e0} saturation. Analysis of central values of $\chi_{eff}(0)$ show a clear increase with increasing central electron temperature, with a linear dependence giving the best fit. On the basis of the analysis just summarized, it can be concluded that the temperature saturation is caused by a combination of both local and non-local effects, namely the

degradation of confinement with increased RF power and the presence of large orbits of minority ions (the importance of which increases with increasing RF power). In steady-state conditions, when no instability processes are present (like sawteeth, or MHD activity in general), these effects are sufficient to explain why the central electron temperature does not scale linearly with P_{RF} / n_{e0}.

Extrapolation of the present model to high RF power per particle shows that orbit effects are responsible for the loss of a considerable fraction of the coupled RF power from the plasma centre. An experimental proposal has therefore been put forward to combine ICRF heating and LH and raise T_{e0} while at the same time avoid orbit effects.

6.5 References

1. E. Righi et *al.*, Proc. EPS Topical Conference on Radiofrequency Heating and Current Drive of Fusion Devices, Brussels, Belgium (1992).

2. P.J. Lomas et *al.*, Proc. 17th EPS Conference on Controlled Fusion and Plasma Physics, Amsterdam, NL (1990).

3. J.G. Cordey et *al.*, Proc. 18th EPS Conference on Controlled Fusion and Plasma Physics, Berlin, FRG (1991)

4. B. Balet et *al.*, Nucl. Fusion **32** (1992), 1261.

5. B. Balet et *al.*, Proc. 19th EPS Conference on Controlled Fusion and Plasma Physics, Innsbruck, Austria (1992).

6. The JET Team (presented by J.G. Cordey), Proc. 14th IAEA Conference on Plasma Physics and Controlled Fusion Research, Wuerzburg, Germany (1992).

7. J.P. Christiansen, J.G. Cordey and D.G. Muir, Nucl. Fusion **29** (1989), 1505.

8. L.-G. Eriksson et *al.*, Nucl. Fusion **29** (1989), 87.

9. J.P. Christiansen, J.D. Callen, J.G. Cordey and K. Thomsen, Nucl. Fusion **28** (1988), 817.

10. H. Hemnen et *al.*, JET Report JET-R(90)06.

11. F. Tibone, private communication.

12. J.G. Cordey, private communication.

13. D.P. Schissel et *al.*, Nucl. Fusion **32** (1992), 689.

14. C.C. Petty et *al.*, Proc. 18th EPS Conference on Controlled Fusion and Plasma Physics, Berlin, FRG (1991).

15. M. Bureš et al., Plasma Phys. and Controlled Fusion **31** (1989), 1843.

7.0 Interaction of ^{3}He ions with plasma impurities during ICRF heating

7.1 Introduction

The presence of impurities in any laboratory plasma is unavoidable, due for instance to the interaction of the plasma with the solid walls of the vacuum vessel, sputtering on the RF antennae caused by acceleration of ions in the rectified electric field near the antenna conductors, and so on. Impurities however can cause heavy energy losses through bremsstrahlung at wavelengths rarely reabsorbed by the plasma, with an intensity of the radiated energy proportional to Z_{imp}^2 [7.01]. Energy losses of this type pose a serious problem to ignition.

The only viable solution is to reduce as much as possible the electronic charge of the materials of the first wall. For this reason in JET to the stainless steel vacuum vessel tiles have been applied made at first of graphite (releasing ^{12}C impurities) and more recently of beryllium [7.02]. The problem of impurity release during ICRF heating has also been solved by using Faraday screens made of beryllium rather than nickel [7.03] (see also Chapter 2).

Of the main impurities present in a typical JET plasma during ICRF heating, ^{9}Be is probably the most interesting and troublesome in a (^{3}He)D plasma. High energy ^{3}He ions, accelerated by the fast wave electric field, undergo highly exothermic nuclear reactions with ^{9}Be nuclei, thus emitting γ photons which in some cases can mask completely the spectrum resulting from ^{3}He-D fusion reactions (see Section 7.2, and also Chapter 5).

During the last JET experimental campaign measurements of the γ emissivity have been made using detectors along both the horizontal and vertical lines of sight. Tomographic inversion has been used to generate the distribution of γ emission in the

poloidal cross-section. Contour plots of γ emission on the poloidal plane, expressed as false colour images, have been obtained during both on-axis and off-axis ICRF heating. These pictures bear the unmistakable shape of orbits of ^{3}He ions trapped in the toroidal magnetic field.

In the present Chapter it is shown that such images can be simulated by merging information obtained from the fast ion distribution and from nuclear reactions producing the observed γ's. Thus after an introductory Section, where the necessary data on γ production are derived (Section 7.2), the two main tools used to simulate the γ-ray emission are introduced (Section 7.3). The first one is a bounce-averaged Fokker-Planck code which calculates the minority ion distribution as a function of the parallel and perpendicular velocity $(v_{\parallel}, v_{\perp})$, of minor radius r and of pitch-angle θ. Use of the complete solution of the Fokker-Planck equation is in this case necessary in order to take into account correctly the spread in pitch-angle, which obviously cannot be obtained from the solution of the pitch-angle averaged Fokker-Planck equation described in Chapter 4. Finite orbit effects are then included by using an orbit code which, on the basis of information from the ^{3}He distribution function and of the relevant excitation curves, produces false-colour pictures of the particle orbits by solving the complete orbit equation. The results of the simulations are then compared with the tomographies, and conclusions are drawn in Section 7.4.

7.2 Production of γ photons during ^{3}He-^{9}Be reactions

High energy ^{3}He ions accelerated during ICRF heating can undergo nuclear reactions with ^{9}Be impurities, namely,

$$^9\mathrm{Be} + {}^3\mathrm{He} \rightarrow {}^{11}\mathrm{B} + \mathrm{p} + \gamma \qquad Q = 10\ \mathrm{MeV} \tag{7.1}$$

$$^9\mathrm{Be} + {}^3\mathrm{He} \rightarrow {}^{10}\mathrm{B} + \mathrm{d} + \gamma \qquad Q = 1.09\ \mathrm{MeV} \tag{7.2}$$

$$^9\mathrm{Be} + {}^3\mathrm{He} \rightarrow {}^{11}\mathrm{C} + \mathrm{n} + \gamma \qquad Q = 7.59\ \mathrm{MeV} \tag{7.3}$$

all quite exothermic, as indicated by the positive values that the reaction energy Q assumes. The γ photons are produced when the residual nucleus is formed in an excited state, and subsequently decays to one of the lower excited states, or the ground state.

Of the reactions listed above, the most important one is that given by Eq.(7.1) ($^{9}Be(^{3}He,p)^{11}B$ in the formalism of nuclear physics), for several reasons. Firstly, because Eq.(7.3) is the isobaric reaction of Eq.(7.1), so that the energy levels and γ emission are pratically identical to those of Eq.(7.1). $^{9}Be(^{3}He,p)^{11}B$ can therefore be considered to represent both reactions without loss of generality. Secondly, the reaction energy produced by Eq.(7.1) is about one order of magnitude greater than that produced by Eq.(7.3). For these reasons, in what follows only reaction (7.1) will be discussed in detail and considered in the present analysis.

The $^{9}Be(^{3}He,p)^{11}B$ reaction has been extensively studied when nuclear physicists were attempting to understand the mechanisms by which nuclear reactions proceed. By measuring as a function of the energy of the bombarding ions the variations in quantities like the angular distribution of the emitted particles, the differential cross-sections and the presence of resonances in the reaction yield, they were trying to decide whether the compound nucleus model or the inelastic scattering theory (or direct process model) [7.04] was more adequate to describe the processes in reactions involving (n,d), (p,d), (d,p), and (d,t) [7.05,7.06,7.07,7.08,7.09].

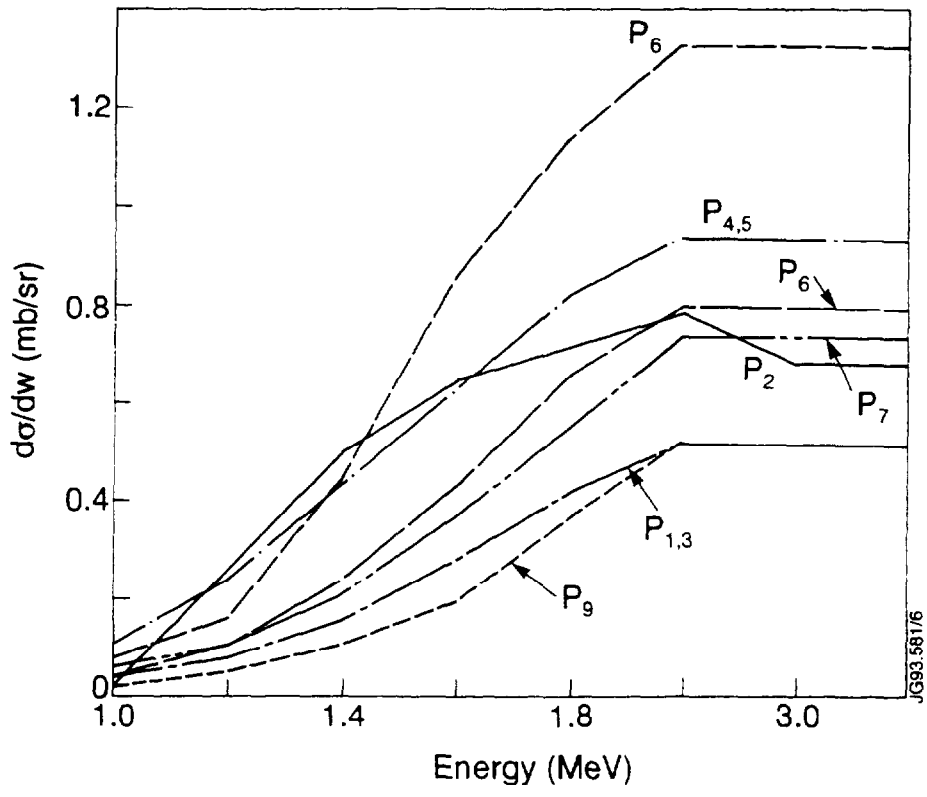

Figure 7.1 ^{11}B excitation curves at 90°. The energy levels from the first to the ninth are shown.

Reactions in which a proton is emitted from the bombardment of light nuclei with ^{3}He particles in the MeV range of energies has been regarded by many authors [7.05,7.06,7.07,7.08,7.09] as a severe test of the direct process model. In fact such a model requires either the simultaneous capture of two particles by the target nucleus or a two-step process in which just one particle is captured by the target nucleus, followed by the capture of the second particle by the nucleus thus formed. If the direct process is responsible for any of these reactions, then its contribution to the reaction relative to that of the compound nucleus can vary considerably for different reactions depending on the structure of the target and residual nuclei [7.05]. For these reasons reactions have been investigated for different target nuclei, different energies of the ^{3}He ions and for as many energy levels of the residual nuclei as possible.

Table 7.1 Main properties of ^{11}B excited states [7.10]

state	E_i (MeV)	τ_m(sec) or Γ_γ (eV)	E_f (MeV)	branch (%)
P_1	2.12	0.122 eV	0	100
P_2	4.44	0.54 eV	0	100
			2.12	<0.5
P_3	5.02	1.73 eV	0	85±2
			2.12	15±2
			4.44	<0.3
P_4	6.74	$<3\times10^{-13}$	0	70±2
			2.12	<3
			4.44	30±2
			5.02	<1
P_5	6.79	$<5\times10^{-14}$	0	71±5
			2.12	29±5
			4.44	<8
			5.02	<8
P_6	7.30	1.0 eV	0	87±2
			2.12	<1
			4.44	5.5±1
			5.02	7.5±1
P_7	7.99	$<5\times10^{-13}$	0	47±2
		$<5\times10^{-14}$	2.12	53±2
			4.44	<1
			5.02	<1
P_8	8.57	2.0 eV	0	56±2
			2.12	30±2
			4.44	5±1
			5.02	9±1
P_9	8.93	4.0 eV	0	95±1
			2.12	<1
			4.44	4.5±0.5
			5.02	<1
			6.74	<1
			6.79	<1

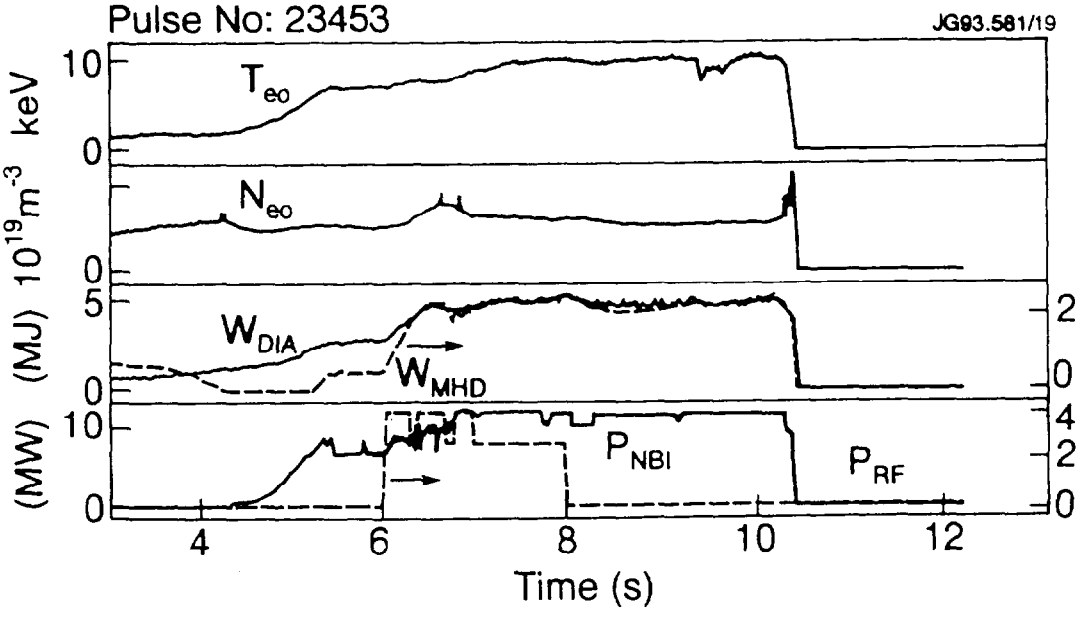

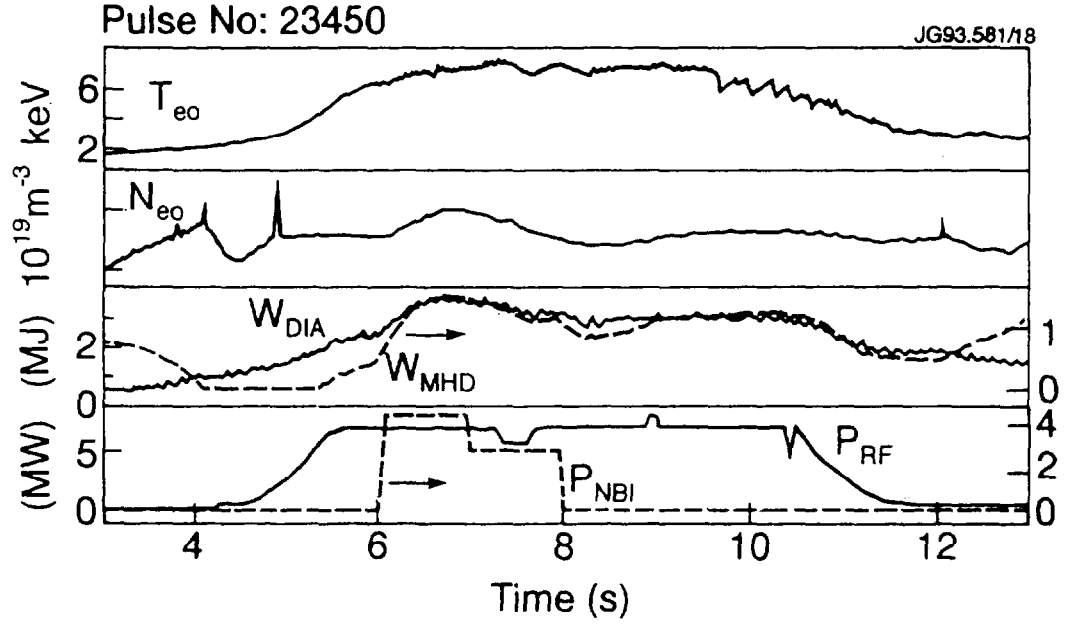

Figure 7.2 Time evolution of the main plasma parameters for discharges JPN 23453 (Fig.7.2a) and JPN 23450 (Fig.7.2b).

One of the most extensive studies of the $^{9}Be(^{3}He,p)^{11}B$ reaction is due to W.R. Coker et *al.* [7.09], where measurements in the laboratory frame of reference of the differential cross-sections at 90° for protons leaving ^{11}B in its excited states for ^{3}He energies from 1 to 3 MeV have been measured. For some of the excited states the angular distributions of the excitation curves are also given. In [7.09] energy levels from the second to the ninth have been considered.

Information about the ground and first excited states of ^{11}B can be obtained from E.A. Wolicki et *al.* [7.07] at 90° and energies of the ^{3}He particles between 2 and 5 MeV, and for the second and third excites states at energies greater than 3 MeV. In the latter cases saturation of the differential cross-section $d\sigma / d\omega$ at high energies suggests that above 3 MeV $d\sigma / d\omega$ can be considered to be constant without any loss of generality. Also, since the ^{11}B nucleus in its ground state obviously does not produce γ's, only excited states from the first upwards will be considered in the present analysis. A summary of the main properties of the excited states of ^{11}B is presented in Table 7.1, while their excitation curves at 90° are reported in Fig.7.1 for energies of the ^{3}He particles between 1 and 3.5 MeV. Unfortunately no data have been found about the first excited state P_1 for energies between 1 and 2 MeV. However from [7.07] it can be inferred that for energies above 2 MeV the differential cross-section for P_1 is very similar to that for P_3, the third excited state. In absence of these data, it will therefore be assumed that the excitation curves for the first and third excited states coincide.

The γ photons thus produced are measured by means of the neutron profile monitor [7.11] (see also Chapter 5).This diagnostic consists of two cameras made of heavy concrete each comprising a set of fan shaped collimated lines of sight. Although intended to measure neutron emission profiles, the detectors used (NE213 liquid organic scintillators) are also sensitive to γ rays. Neutrons and γ events are separated using pulse shape discrimination electronics, so that the instrument can also be used to obtain γ-ray emission profiles. The signals are then fed into a tomography program, originally developed for analysis of soft-X ray emission [7.12] and suitably interfaced to use γ-ray data. The data presented in this Chapter are the first attempt to obtain a tomographic reconstruction of γ-ray emission. At this preliminary stage an estimate of the order of magnitude of the uncertainty in the measurement of the γ emissivity is rather difficult, and error bars cannot therefore be derived. The main source of uncertainty comes from the fact that in order to increase the γ-ray efficiency of the instrument the electronic acceptance window has been wide opened [7.13].

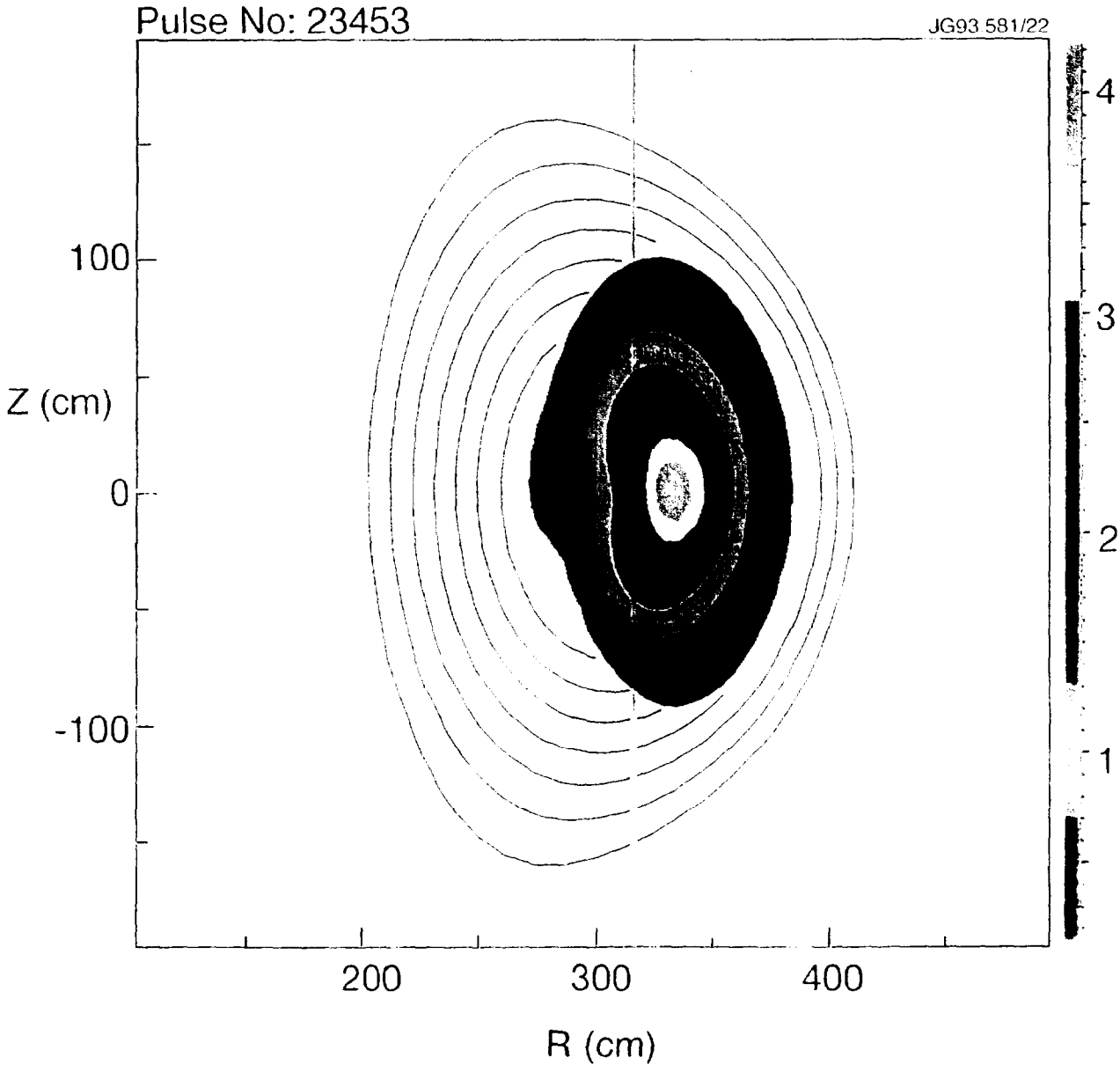

Figure 7.3a False colour tomography of γ emissivity for JPN 23453.

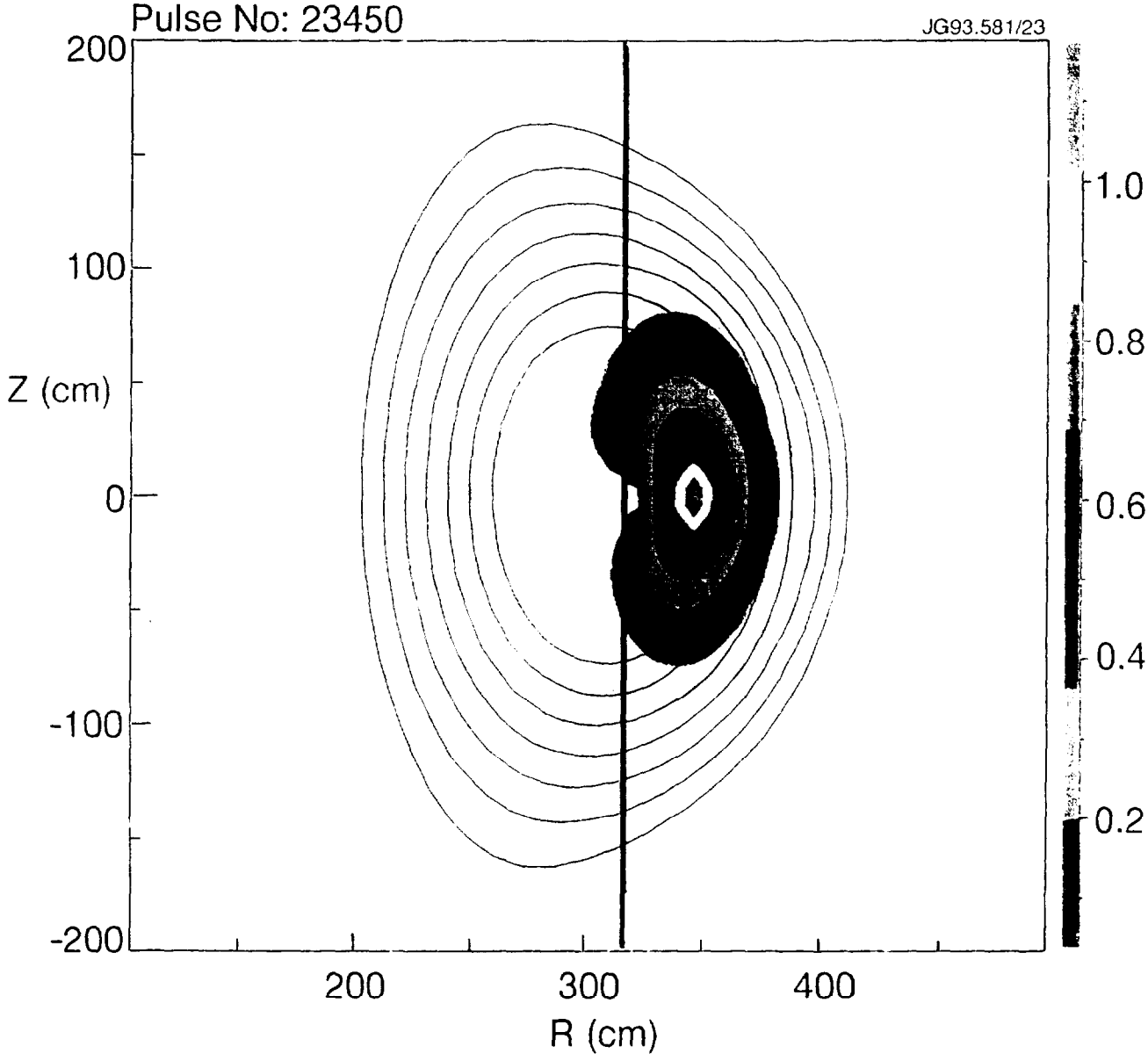

Figure 7.3b False colour tomography of γ emission for JPN 23450.

Table 7.2. Main Plasma Parameters

	JPN 23450	JPN 23453
time-slice t_0 (sec)	49.0	49.0
plasma current (MA)	3.5	3.5
magnetic field on-axis (T)	3	3
$T_e(0)$ (keV)	7.3	7.4
$n_e(0)$ (10^{19} m^{-3})	2.8	3
P_{RF} (MW)	7.9 (off-axis)	11.7 (on-axis)
magnetic axis position (m)	3.10	3.12
off-set from resonance (m)	0.29	0.06
fast ion energy (MJ)	0.2	1
Z_{eff}	1.5	1.6
minority fraction*	0.045	0.13

***from PHANTOM estimate of the fast ion energy**

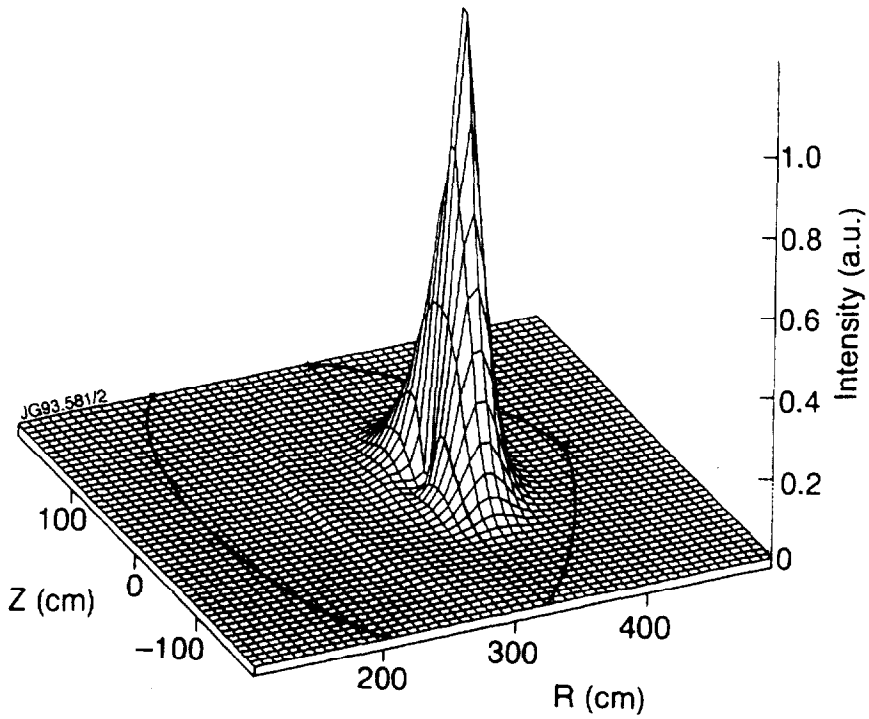

Figure 7.4 3D tomographic inversion of γ emissivity for JPN 23450.

In the present analysis the γ-ray emission from two ICRF heated discharges have been considered, one with the RF resonance on-axis (JPN 23453), and one off-axis (JPN 23450). The evolution of the main experimental parameters for these discharges is shown in Fig.7.2, while the time-slices chosen for analysis and the corresponding plasma parameters are reported in Table 7.2. The correspondent false colour images for γ emission are shown in Fig.7.3 [7.14,7.15], while the 3D tomography of γ

intensity in the poloidal plane is reported in Fig.7.4 for the off-axis discharge JPN 23450 [7.16].

Note that the γ ray detectors have essentially no energy resolution. It is therefore sensible to consider a "total" differential cross-section, sum of all the excitation curves from the states of ^{11}B, which gives an estimate of the relative probability for a γ photon to be emitted from any of its excited states in the energy interval of interest. Such cross-section in shown in Fig.7.5.

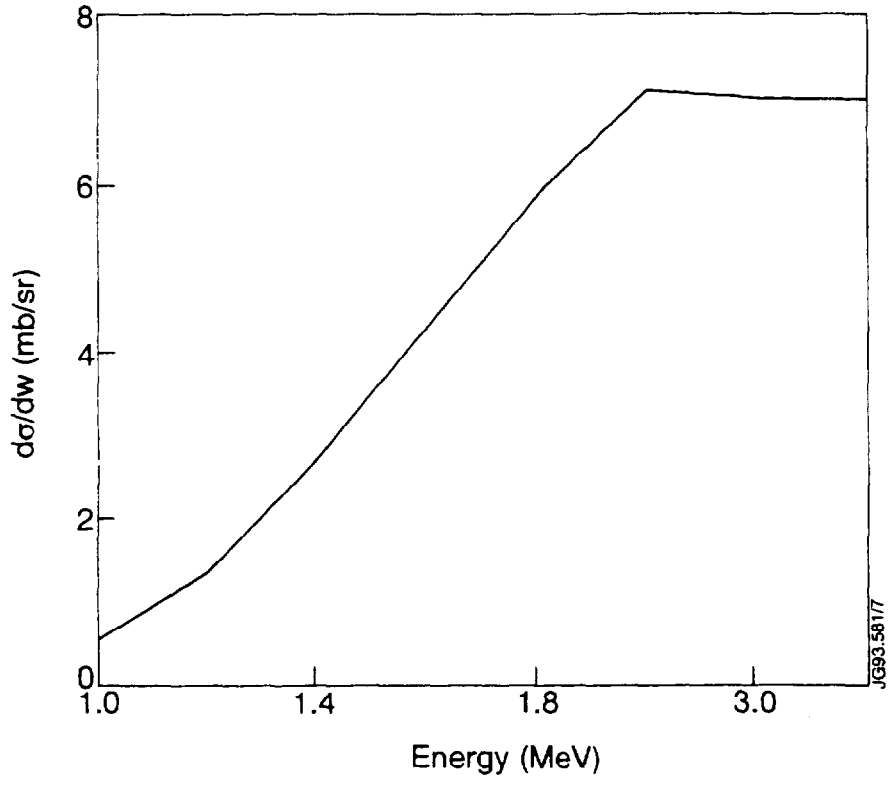

Figure 7.5 **"Total" differential cross-section for ^{11}B.** $(d\sigma/d\omega)_{tot}$represents the relative probability for a γ photon to be emitted from any of ^{11}B excited states in the energy interval of interest.

7.3 Simulation of γ-ray emission

In the present Section it is shown that the γ-ray emission previously discussed can be reproduced numerically both qualitatively (in the form of false colour pictures reproducing Fig.7.3), and quantitatively by closely reproducing the profile of the γ emissivity along the vertical line of sight.

A number of different pieces of information are necessary in order to describe correctly the interaction of ^{3}He ions with ^{9}Be impurities and the γ production:

- the distribution of ^{3}He ions in velocity space ($v_{\parallel}, v_{\perp}$) AND in pitch-angle θ as a function of minor radius;
- the orbit paths of the fast ^{3}He ions;
- the distribution of ^{9}Be ions;
- data on the excitation curves for γ production.

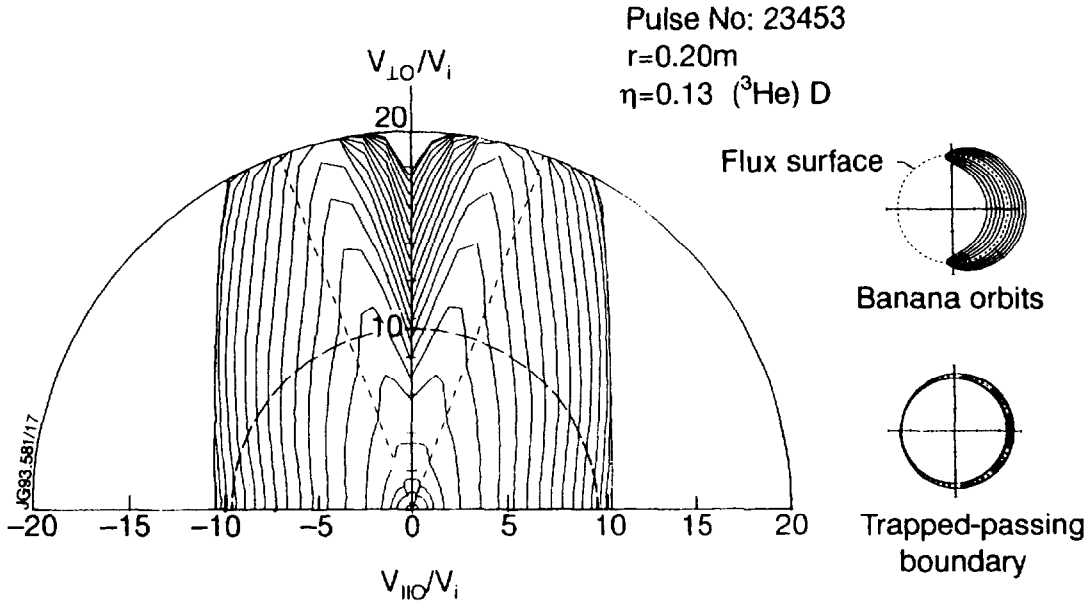

Figure 7.6 Minority ion distribution function in ($v_{\parallel}$,$v_{\perp}$) space. The distribution has been calculated for JPN 23453 (on-axis ICRF) ar r=0.20m. The parallel and perpendicular velocities are normalized to the thermal velocity of the background ions, v_i.

The γ production has been already discussed in Section 7.2. In the present analysis a uniform distribution of ^{9}Be atoms in the plasma will be considered, with a concentration of the order of 1% of the electron density, consistent with the measured values of Z_{eff} (see Table 7.2). Such an approximation is justified by the fact that the discharges considered present a few sawteeth, which contribute to mix ion species in different parts of the plasma.

The distribution of ^{3}He ions cannot be calculated in the present instance from the pitch-angle averaged Fokker-Planck equation introduced in Chapter 4, or with the "effective pitch-angle" distribution used in Chapter 5. The reason for this is that to the γ production contribute both trapped and passing fast ions which, for equal launch coordinates on the midplane (z=0) and energy, have different pitch-angles. To calculate $f(E,r,\theta)$ therefore use has been made of the solution of the steady-state bounce-averaged Fokker-Planck equation provided by a 2D code in cylindrical geometry which takes into account a steady Ohmic electric field, and includes a quasi-linear ICRF diffusion operator [7.17]. An example of such distribution at r=0.20 m (about 10 cm away from the resonance) is shown in Fig.7.6 for discharge 23453. In the picture the parallel and perpendicular velocities of the resonant particles on the midplane are normalized to the thermal velocity of the background ions, v_i. The distribution f is represented as a contour plot of constant f, while the dashed lines mark the boundary between trapped and passing particles. Particles with equal energy lie on a circumference centred in the origin: for instance, E=1 MeV corresponds in the figure to the dashed circle with $v_{\perp 0}/v_i = 9.5$. At any particular radius of the E=*const* circumference to a certain value of f corresponds a pitch-angle $\theta = v_{\perp 0}/v_{\parallel 0}$. Note that the ridge visible in Fig.7.6 is due to the presence of trapped particles moving along banana orbits, the peak of the ridge corresponding to ^{3}He ions with their turning points touching the RF resonance. The bounce-averaged Fokker-Planck code by definition does not include finite orbit widths of the resonant particles. However the model can still describe correctly different types of particles depending on energy, pitch angle and on where the RF resonance is positioned. Trapped particles (with values of the distribution along the ridge) and particles with energy and pitch-angle on the trapped-passing boundary are also schematically shown in Fig.7.6. In order to include the contribution of trapped particles, the values of the pitch-angle used in the present analysis are therefore those corresponding to the peak of the ridge. A spread in pitch-angle of $\pm 5°$ is also considered in order to include trapped ions with their turning points not on the RF resonance and passing particles. The latter are localized between the magnetic axis and the RF resonance ($0 \leq r \lesssim 0.20$ m) in the case of off-axis ICRF, and the outermost flux surfaces ($r \gtrsim 0.40$ m) for on-axis ICRF. The value of 5° has been estimated from the width of the ridge in pitch-angle.

The intensity of γ-ray emission can be calculated as,

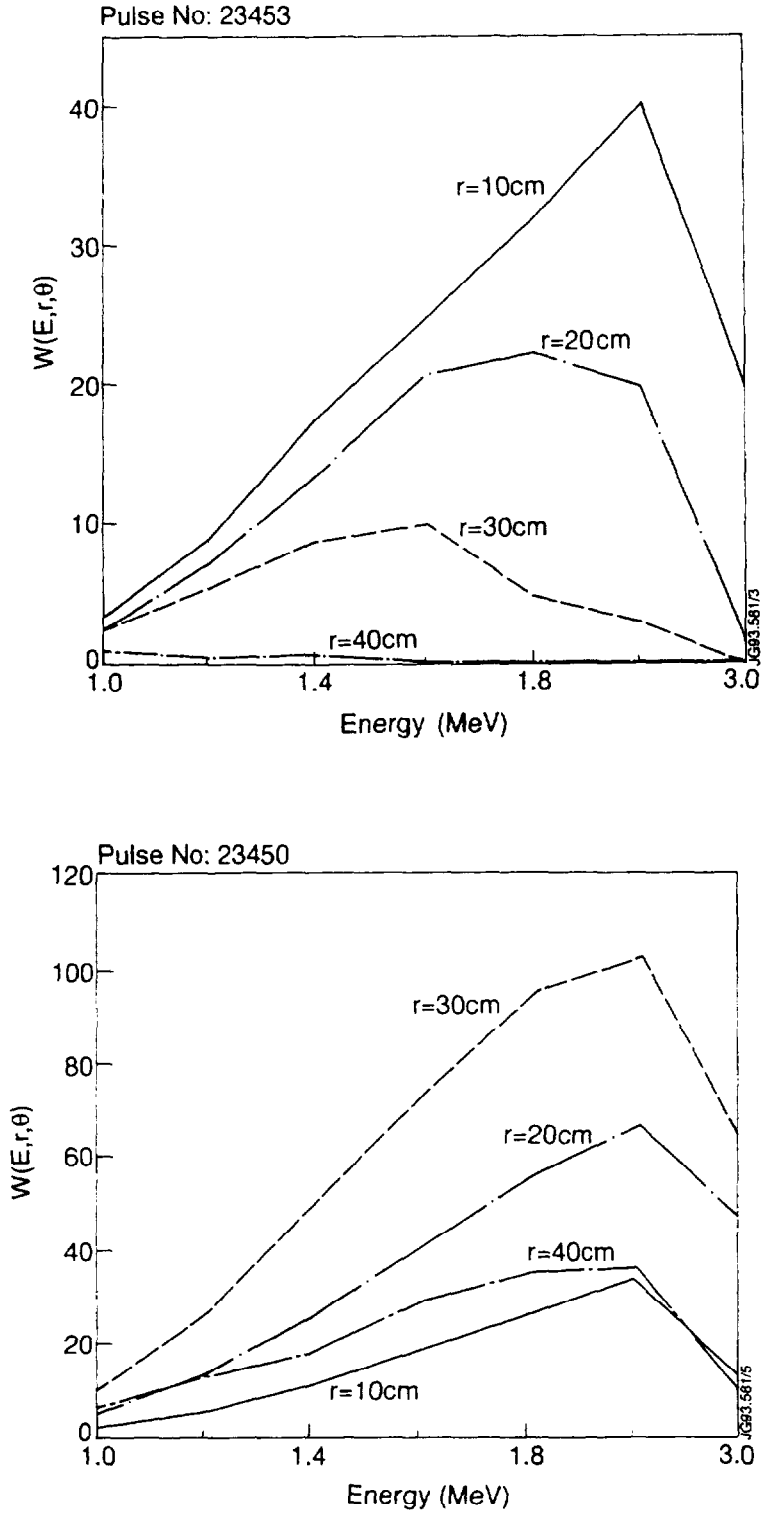

Figure 7.7 Weight functions for the values of the pitch-angle θ on the distribution ridge. As usual, Figs.7.7a-b refer to JPN 23453 and JPN 23450, respectively.

$$I_\gamma \propto \int d^3r \int dE \sqrt{E} f(E,r,\theta) \left(\frac{d\sigma}{d\omega}\right)_{tot} \left(\frac{\Delta t}{T}\right)_{T\to\infty}$$
$$\int_0^{a_0} dr r \int_0^{\pi} d\theta \int_0^{\infty} dE \sqrt{E} f(E,r,\theta) \left(\frac{d\sigma}{d\omega}\right)_{tot} \left(\frac{\Delta t}{T}\right)_{T\to\infty} \quad (7.4)$$

where $(d\sigma/d\omega)_{tot}$ is the excitation curve shown in Fig.7.5 and obtained by summing the contributions from all excited states of ^{11}B (see Section 7.2), while $(\Delta t/T)_{T\to\infty}$ represents the time spent by one fast ion at any point along its orbit path. This last quantity is provided for by the program ORBIT, which calculates the full particle orbits (that is, including Larmor radius effects) in the tokamak magnetic field and can calculate the time spent by one or more such particles in different points of the poloidal plane [7.18]. No correction of the launching coordinates from cylindrical to

toroidal geometry is in this case necessary, since initial conditions are given on the midplane. For the present analysis the program has been substantially modified for multiple particle launch, and new software has been developed for storage of the data, processing and transfer to a suitable graphic support. Input parameters are the shot number and time-slice (for magnetic reconstruction retrieved from the JET database), launching coordinates (position on the poloidal plane), initial pitch-angle and energy. If coupled to information about the distribution of fast minority ions and on the γ excitation rates, this program effectively calculates the intensity of γ emission for a distribution of particles launched in the midplane, with the same energy, different pitch-angles and increasing minor radius according to the weight function,

$$w(E,r,\theta) = r\sqrt{E} f(E,r,\theta) \left(\frac{d\sigma}{d\omega}\right)_{tot}. \quad (7.5)$$

An example of weight function for the values of θ on the ridge and increasing energy at different radii is shown in Fig.7.7 for both discharges analyzed. Note that in both cases the $w(E,r,\theta)$ peaks around 1.5-2 MeV, with the highest values of w corresponding to the radius nearest to the resonance (r=0.10 m for the on-axis discharge of Fig.7.7a, r=0.30 m for the off-axis case of Fig.7.7b). This latter characteristic is due to the fact that the Fokker-Planck code used to derive the distribution function assumes that the RF wave is peaked on the midplane at a radius correspondent to the RF resonance, where as a consequence the strongest tail is produced. On the basis of these results, we have chosen to plot the particle orbits at

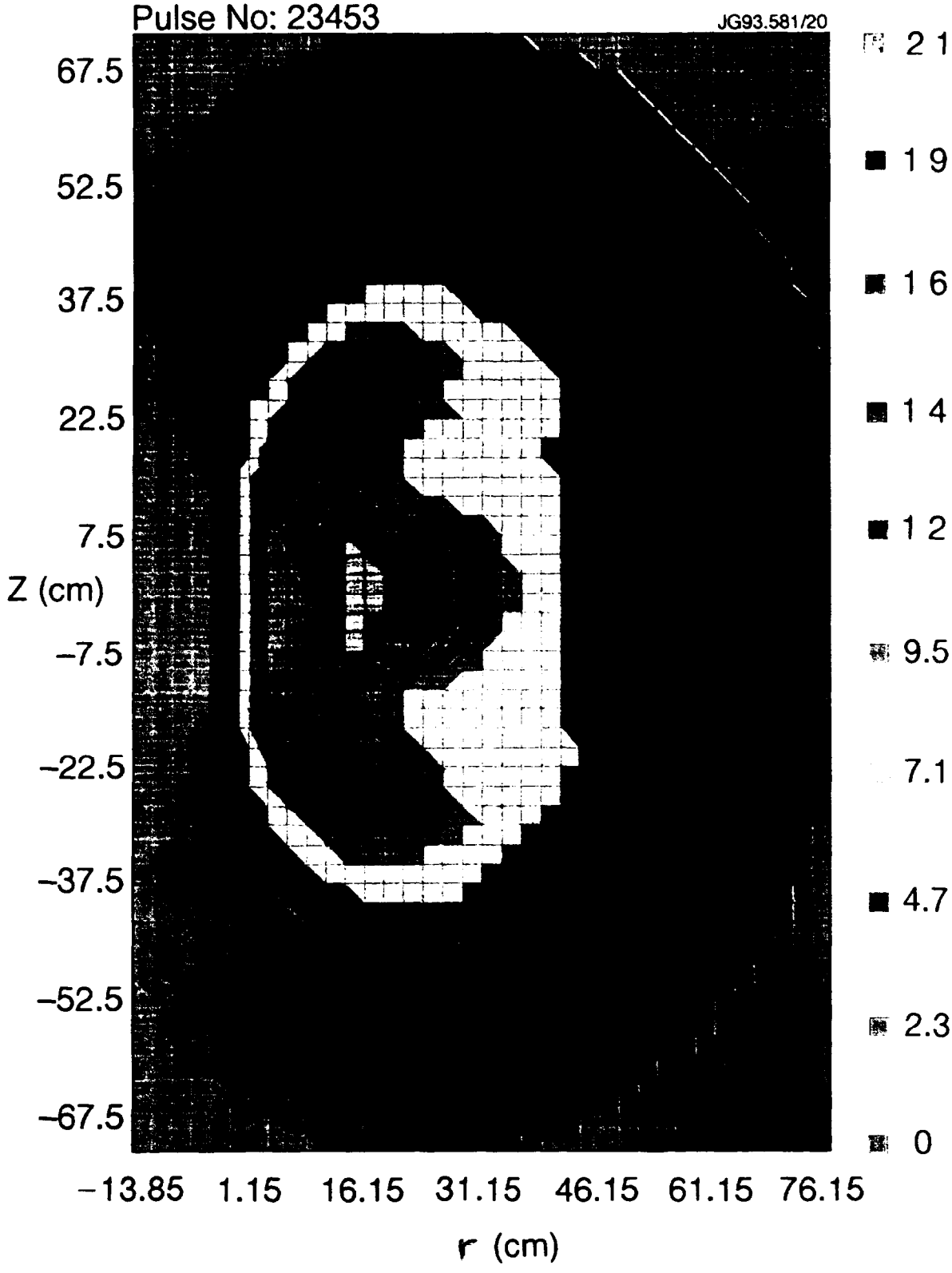

Figure 7.8a False colour image of the simulation of γ emissivity for JPN 23453.

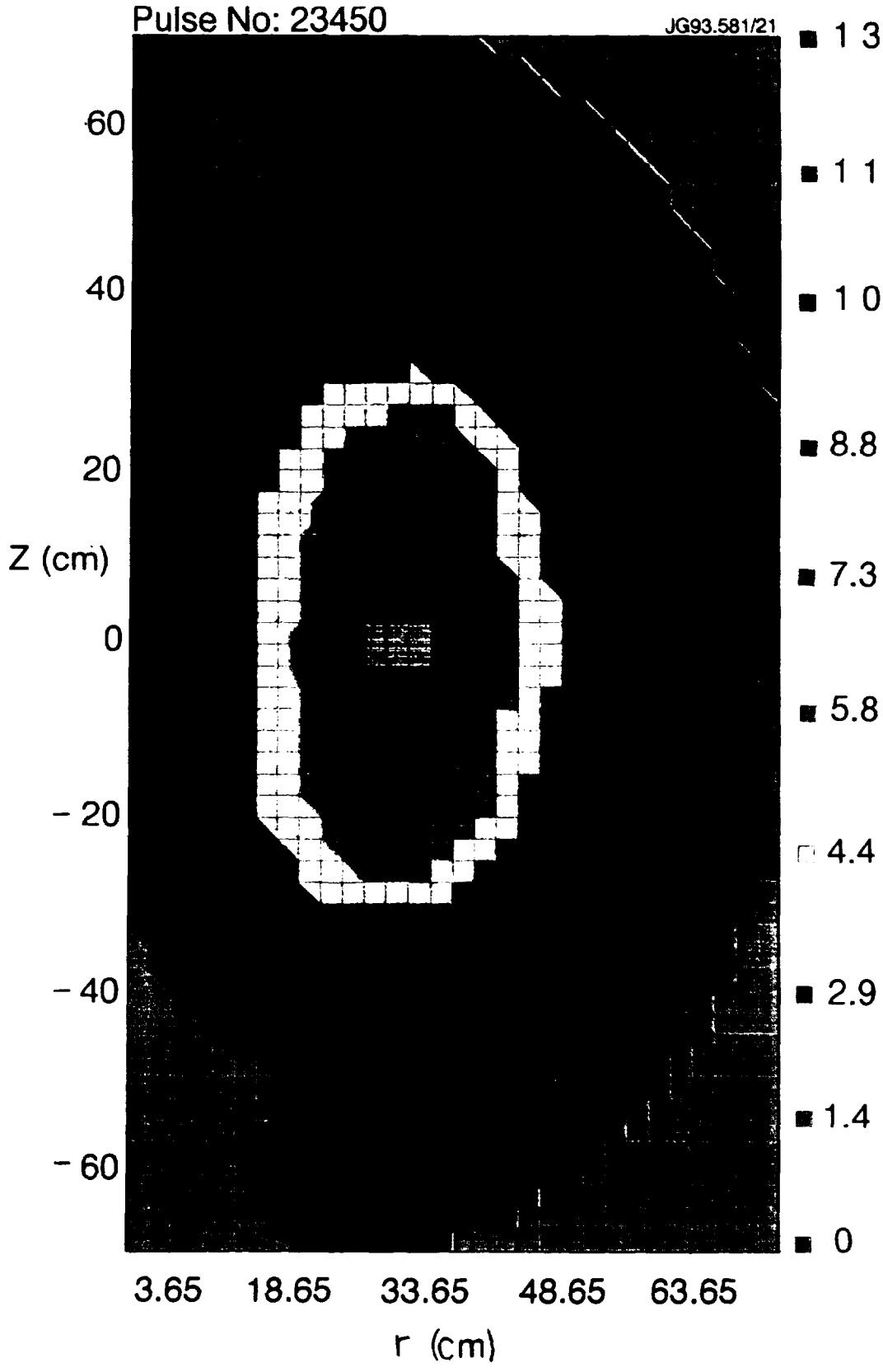

Figure 7.8b False colour image of the simulation of γ emissivity for JPN 23450.

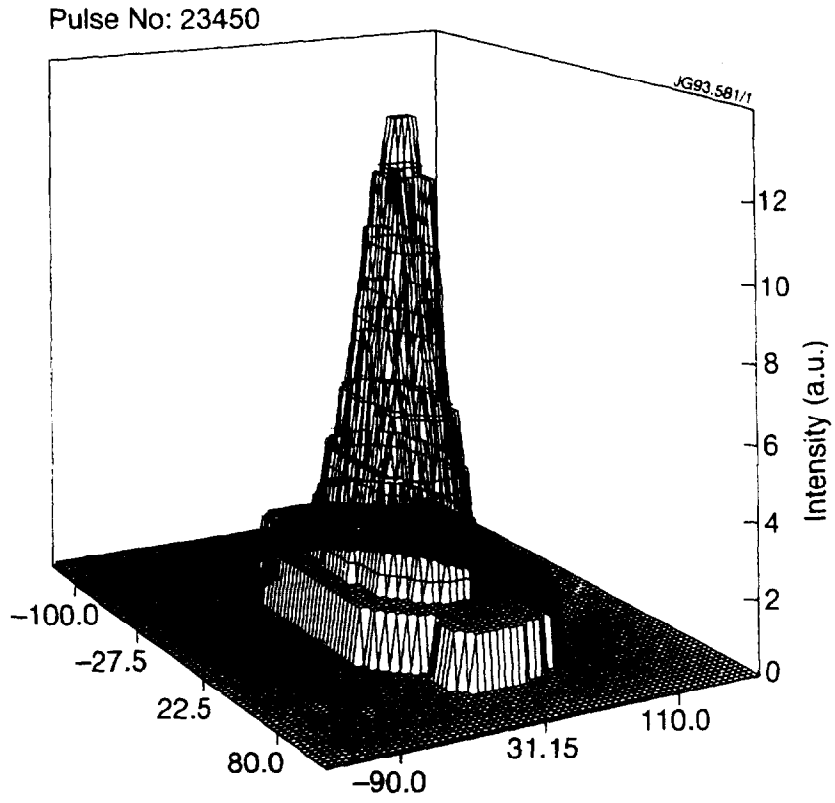

Figure 7.9 3D numerical reconstruction of γ emissivity for JPN 23450.

the energies E=1,2,3 MeV. For each energy the result has been stored in a dataset as a grid of binary data (each dataset used contained 1Mbyte of data), which have subsequently been summed up and processed. The results of these calculations are shown in Fig.7.8 in the form of false colour images. Both on-axis (Fig.7.8a) and off-axis (Fig.7.8b) cases are reported. Fig.7.8 shows that all the qualitative features of the γ-ray emission are present (compare with Fig.7.4). The differences between measurements and calculations in the lowest intensity areas of the pictures (black in Fig.7.4, green in Fig.7.8) are not relevant, due to high noise levels present during the measurements and to the fact that low energy trapped particles with launching coordinates $r \geq 50$cm have a weight function too small (approaching zero) to be of any use in the present simulation.

Figs.7.8a-b are qualitatively different, both in localization of the peak and shape of the orbits. Such difference can be explained by considering the distribution functions of the ^{3}He ions in the two cases. In the off-axis case (Fig.7.8b), trapped particles are in fact localized either on the RF resonance ($r \cong 0.30$ m) or nearby, with a non-negligible presence of passing particles between the magnetic axis and the resonance layer and in the outermost part of the poloidal plane. On the other hand in

the on-axis case (Fig.7.8a) trapped particles dominate from the resonance position near the plasma centre up to about r=0.30 m. In Fig.7.8b D-shaped orbits are evident.

From a quantitative point of view, it is convenient to compare the intensity of measured and calculated γ emission as a function of z (the vertical chord in the poloidal plane) at a radius corresponding to the peak emissivity. The data have been obtained from a major section of Fig.7.4 and from the corresponding 3D numerical reconstruction of the γ intensity, shown in Fig.7.9. The result, shown in Fig.7.10, where the two curves have been normalized to the same number of γ counts, clearly indicates that the γ intensity is well reproduced by the calculation.

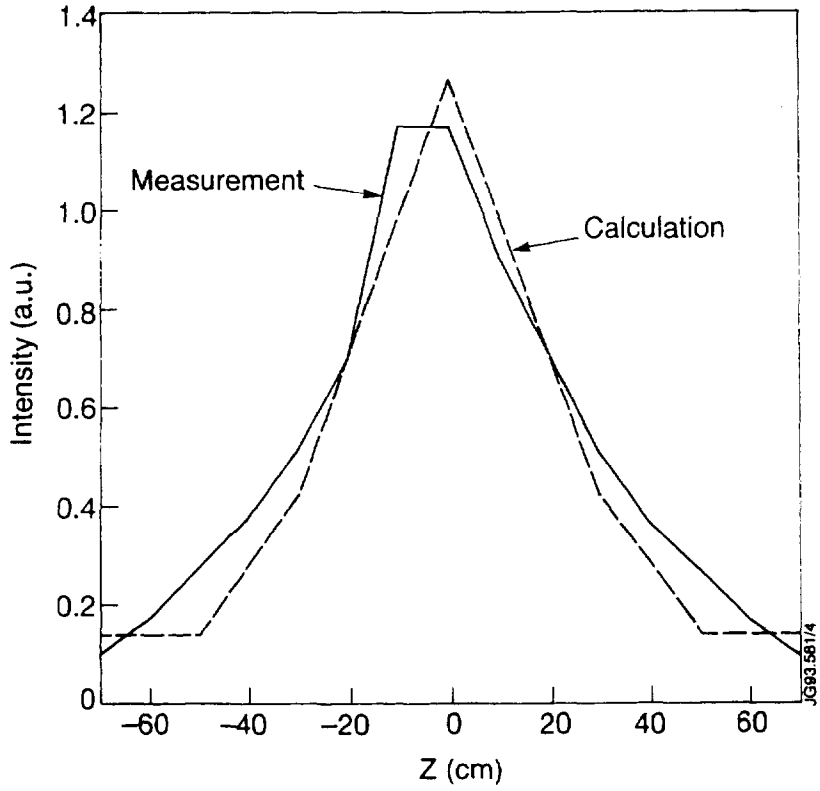

Figure 7.10 Comparison of calculated and measured γ intensity at the radius corresponding to the peak emissivity. Both curves have been normalized to the same total number of γ counts.

7.4 Summary and conclusions

In the present Chapter the emission of γ photons produced during nuclear reactions of high energy ^{3}He ions with ^{9}Be impurities in ICRF heated plasmas has been studied, and measurements of intensity of γ emission on the poloidal plane, in the form of both 2D and 3D tomographies, have been considered.

It has been shown that such γ emission can be successfully simulated numerically by combining information about the ^{3}He distribution on the midplane in $(v_{\parallel}, v_{\perp}, r, \theta)$ space and the relevant nuclear reactions producing the γ's with the proper orbit paths that the fast ions follow in the plasma. Results agree with experiment both qualitatively and quantitativelyin the estimate of the measured intensity of γ emission.

Clearly many assumptions have been made to derive the results presented here. The main approximation introduced is the use of a distribution function derived from a zero-banana width code as a source of particles launched on the midplane for the orbit solver, while the re-distribution of the minority ions is derived by following orbits. An alternative method, although based on the same approximations, could use particle launch along a vertical chord at the resonance position. In this case the initial pitch-angles, calculated at present on the midplane, would need to be transformed into the corresponding θ values along the vertical RF resonance by means of the orbit equation, and the initial conditions on the vertical chord would need to be corrected to include the elongation. A long term solution would of course be the development of a Monte Carlo code.

The numerical technique developed in the present Chapter is full of potentialities to be explored. In the case considered here the γ emissivity has been calculated from physical principles. However the same technique can be applied to the experimental data themselves to derive not only the distribution of the fast ^{3}He ions, but also the profile of the RF power coupled to the minority ions. Compare in fact the expressions of the intensity of γ emission given by Eq.(7.4) with that of the electron power deposition profile given by Eq.(4.30-1): the dominant terms in the kernels of the two integrals are, respectively,

$$K_{\gamma} = f(E)\left(\frac{d\sigma}{d\omega}\right)_{tot}\left(\frac{\Delta t}{T}\right)_{T\to\infty},$$

$$K_{P} = f(E)\frac{E}{\tau_b}\left(\frac{\Delta t}{T}\right)_{T\to\infty}.$$

Given the measured γ emissivity, for each flux surface it is then possible to derive K_{γ} and, consequently, K_P (K_{γ} is equal to K_P when $(d\sigma/d\omega)_{tot}$ is replaced by E/τ_b). Integration along each flux surface finally provides the power deposition

profile. This way for perhaps the first time the RF power deposition profile would be measured.

The present technique could also be used as a diagnostic tool to identify the so called Toroidal Alfven Eigenmode (TAE) modes. In fact in absence of any instabilities, the intensity of the emitted γ's is described by Figs.7.8-7.9. Ions on the trapped/passing boundary are thought to be most susceptible to TAE modes since a small change in pitch-angle at the turning point can provoke a huge change in the orbits. The presence of TAE modes would provoke bursts of ^{3}He ions to be ejected from the plasma centre, thus replacing the peaked structure of Fig.7.9 with a flat profile lacking the trace of the orbit paths, so characteristic of Fig.7.3.

7.5 References

1. T.J.M. Boyd and J.J. Sanderson, *Plasma Dynamics*, Thomas Nelson & Son Ltd, London, 1969.

2. M Keilhacker and the JET Team, JET Report JET-P(89)83

3. M. Bureš et *al.*, Plasma Phys. and Controlled Fusion **33** (1991), 937.

4. D.F. Jackson, *Nuclear Reactions*, Methuen & Co. Ltd, London, 1970.

5. H.D. Holmgren, M.L. Bullock and W.E. Kunz, Phys. Rev. **104** (1956), 1446.

6. S. Hinds and R. Middleton, Proc. Phys. Soc. **A74** (1959), 196.

7. E.A. Wolicki et *al.*, Phys. Rev. **116** (1959), 1585.

8. S. Hinds and R. Middleton, Proc. Phys. Soc. **A75** (1960), 754.

9. W.R. Coker et *al.*, Nucl. Phys. **A91** (1967), 97.

10. F. Ajzenberg-Selove and T. Lauritsen, Nucl. Phys. **A336** (1980), 1-154.

11. J.M. Adams et *al.*, Nucl. Instr. and Methods in Physics Research **A329** (1993), 277.

12. R.S. Granetz and P. Smeulders, Nucl. Fusion **28** (1988), 457.

13. G. Sadler, private communication.

14. O.N. Jarvis, JET Report JET-P(93)30.

15. P.J.A. Howarth, private communication (1993).

16. JET Joint Undertaking Progress Report (1992).

17. M.R. O'Brien, M. Cox and D.F.H. Start, Nucl. Fusion **26** (1986), 1625.

18. G. Sadler and P. Van Belle, private communication (1993).

19. G. Sadler, private communication (1993).

8.0 Conclusions

The work presented in this thesis concerned the role that large orbits of resonant minority ions have during high power ICRF heating experiments on JET.

A model, based on the solution of the steady-state pitch-angle averaged Fokker-Planck equation, has been developed by the author to calculate the electron and ion power deposition profiles and the fast ion energy content. The present model differs from its predecessors in that:

- the minority ion-electron collision frequency is energy-dependent, thus reflecting the changes in collisionality that the fast ions experience while travelling along one trapped orbit;
- the minority ion distribution function differs from the old solution of the Fokker-planck equation at high energies (the 'tail' of the distribution), where the number of fast ions in the energy interval of interest has been so far overestimated;
- the collisional power transferred to the electrons is substantially modified and broadened, since the power is now transferred preferentially in zones of higher collisionality;
- the fast ion energy content is systematically lower than that calculated with the zero-orbit models, where the number of high energy fast ions is always overestimated. The new estimate of W_f agrees with experiment within error bars.

A modification of the orbit model has been rendered necessary when energy intervals had to be considered where pitch-angle scattering was not negligible (Chapter 5). In this case a distribution, function of energy and of an 'effective' pitch-angle, has been used. It has been shown however that, as far as the heating profiles are concerned, there is no significant difference in the use of either distribution (Appendix C).

A numerical code (PHANTOM) has been developed from the orbit model. A number of problems relevant to ICRF hating have then been considered, where the orbit model was thought to contribute to their solution.

1. ^{3}He-D fusion yield.

   The zero-orbit model used so far to calculate the fusion yield makes use of the anisotropic distribution function $f(E_\perp)$ of the minority ions instead of the isotropic one, $f(E)$. The author has shown that this leads to underestimate P_{fus} of about 20%, and that $f(E)$ is the correct distribution to use. The introduction of orbit effects, however, does not alter significantly the magnitude of the maximum fusion yield.However they do affect the minority concentration at which this maximum occurs and the corresponding value of the fast ion energy content. The production of fusion power in a(^{3}He)D plasma has then been extrapolated for a reactor scale device like ITER.

2. Heat transport and T_{e0} saturation.

   A simple model to calculate the heat diffusivity profile in cylindrical geometry has been coupled to the PHANTOM code. It has thus been shown that orbit-induced modification of the electron power deposition profile has important consequences in the values that are derived for the effective heat diffusivity in the plasma centre. In particular, orbit-modified electron heating profiles have been proved to reduce the difference between the χ_{eff} profiles obtained in a (H)D plasma from on/off-axis ICRF discharges, amounting to one order of magnitude if calculated with the zero-orbit model.

   The role of orbits in the saturation of the central electron temperature at high values of the RF power per particle has then been investigated. The T_{e0} saturation has been successfully explained as the combined effect of large orbits of minority ions (the importance of which increases with increasing RF power) and of linear scaling of χ_{eff} with the temperature itself. An experiment has been proposed to raise T_{e0} while avoiding minorty heating altogether, the only way to make sure that orbit effects are not present.

3. γ emissivity.

   The emission of photons in the γ energy range produced during nuclear reaction of beryllium impurities with high energy ^{3}He ions during ICRF heating has been studied. Measurements of the intensity of γ emission on the poloidal plane, in the form of 2D and 3D tomographies, have been considered.

It has been shown that such γ emissivity can be successfully simulated numerically by combining information about the ^{3}He distribution on the midplane in $(v_{\parallel}, v_{\perp}, \theta)$ space and the relevant nuclear reactions producing the γ's with the proper orbit paths that the fast ions follow in the plasma. Results agree with experiment both qualitatively and quantitatively, predicting the measured intensity of γ emission.

A number of developments are likely to spring from the work presented in this thesis. Orbit effects are now recognized to be important in local transport issues. They will be routinely taken into account in the estimates of the heat diffusivity once the main code for ICRF heating in JET is modified accordingly (the author has supplied the subroutine that orbit-averages the collision coefficients), and the power deposition profiles made available for further analysis. The fully optimized fusion yield is not affected by large orbits, but the right procedure for its estimate is now standard. The simulation of γ emissivity, lastly, is full of potentialities, especially as a diagnostic for the power deposition profiles and for fast particle losses due to Toroidal Alfven Eigenmode excitation or due to ripple in the toroidal magnetic field, and it is hoped that in the near future it can become a reality.

Appendix A Legenda

In the present Appendix the most frequently used symbols are listed for reference. The SI unit system is systematically used. Electron and ion temperatures are measured in eV, unless stated otherwise in the text.

To indicate the composition of a two-component plasma, the symbol of the minority ion species is written within parentheses on the left of that of the background ion species. Thus, (^{3}He)D refers to a deuterium plasma with ^{3}He minority.

ε_0	permittivity of free space
μ_0	permeability of free space
k_B	Boltzmann constant
m_p	mass of the proton
-e	electronic charge
R_0	plasma major radius (at the mid-plane)
a_0	plasma minor radius (at the mid-plane)
ε_{ij}	components of the plasma dielectric tensor
Z_i, Z	atomic number of the background and minority ions
m	minority ion mass
m_α, α=e,i	mass of the species α (electrons and background ions)
Ω_α, α=e,i	ion cyclotron frequency of the species α
$\omega_{p\alpha}$, α=e,i	plasma frequency of the species α
$v_{th\alpha}$, α=e,i	thermal velocity of the species α

n_α, α=e,i	number density of the species α
$\mathbf{B}=Be_z$	external magnetic field, defining the direction of the z axis
ω	wave frequency
E_x, E_y, E_z	cartesian components of the wave electric field
$E_\pm=E_x \pm iE_y$	left and right handed circularly polarized components of the wave electric field
$n_\parallel$, $n_\perp$	components of the refractive index parallel and perpendicular to the magnetic field
$v_\parallel$, $v_\perp$	components of the particle velocity parallel and perpendicular to the magnetic field
$k_\parallel$, $k_\perp$	components of the wavevector parallel and perpendicular to the magnetic field
$u_\parallel$, $u_\perp$	components of the particle velocity parallel and perpendicular to the test particle velocity

Appendix B. Scaling Law for Optimum Fusion Yield

In the present Appendix it is explicitely shown how the optimum total fusion power P_{fus} discussed in Chapter 5 scales with the macroscopic parameters which characterize a discharge. To this effect, consider the asymptotic expression of the tail temperature for energies greatly above E_c (see Chapter 4),

$$T_t = k\frac{PT_e^{3/2}}{Vn_{\min}n_e}, \tag{B.1}$$

where,

$$P = P_{RF}e^{-r^2w^2}, \quad V = 2\pi^2 R_0 w^2,$$

and k is a constant factor once the ion species are fixed. For a fixed flux surface radius the expression for the tail temperature given by Eq.(B.1) is constant, since it depends only on the radial profiles of density and temperature. From Eq.(B.1) the minority density can be derived,

$$n_{\min} = k\frac{PT_e^{3/2}}{Vn_eT_t},$$

and substituted into the expression for the total fusion power,

$$P_{fus} = 4\pi^2 R_0 \varepsilon 18.3\times 10^6 \int_0^{a_0} drr\, n_D(r) n_{\min}(r) \int_0^{\infty} dE\sqrt{E} f(E;r) <\sigma v>(E)\ . \tag{B.2}$$

The result reads,

$$P_{fus} = \frac{2\varepsilon k}{w^2} 18.5\times 10^6 P_{RF} \int_0^{a_0} drr \frac{n_D(r)}{n_e(r)} e^{-r^2/w^2} T_e^{3/2}(r) \int_0^{\infty} dE\sqrt{E} f(E;r) \frac{<\sigma v>}{T_t}\ . \tag{B.3}$$

We are interested in the expression for the optimum total fusion power, which is obtained for a tail temperature equal to the energy corresponding to the peak of the reaction rate $<\sigma v>$:

$$T_t \cong E \cong \bar{E} \ ,$$

and relative radius $r \cong \bar{r}$. The distribution function can therefore be approximated by,

$$f(E;r) \cong \delta(E-\bar{E})\delta(r-\bar{r}) \ . \tag{B.4}$$

Furthermore, it can be assumed without loss of generality that the deuterium density is proportional to the electron density, that is,

$$n_D(r)/n_e(r) = b = const \ , \quad \forall r \ .$$

The optimum fusion yield can therefore be written as,

$$P_{fus}^{opt} = \frac{2\varepsilon}{w^2} k\bar{r}b 18.5\times 10^6 e^{-\bar{r}^2/w^2} P_{RF} T_e^{3/2}(\bar{r}) \frac{<\sigma v>(T_t)}{T_t} \ , \tag{B.5}$$

where the ratio $<\sigma v>/T_t$ is now fixed. From Eq.(B.5) it then follow that,

$$P_{fus}^{opt} \propto P_{RF} T_e^{3/2}(\bar{r}) \propto \eta^{opt} \ . \tag{B.6}$$

In particular, if T_e can be written as $T_e = T_{e0}(1-r^2)^{\alpha}$, then Eq.(B.6) reads,

$$P_{fus}^{opt} \propto P_{RF} T_{e0}^{3/2} \ . \tag{B.7}$$

Appendix C The role of the pitch-angle in the calculation of the heating profiles

In Chapter 5 a new distribution function, different from that introduced in Chapter 4 and dependent on both the energy E and the effective pitch-angle μ^2_{eff}, has been introduced because pitch-angle scattering is not negligible any more in the calculation of the fusion yield. Consider in fact the kernel of the integral used to estimate the reactivity (see Eq.(5.11)): $K(E) \propto \sqrt{E} < \sigma v > f_a(E)$ is a function peaked

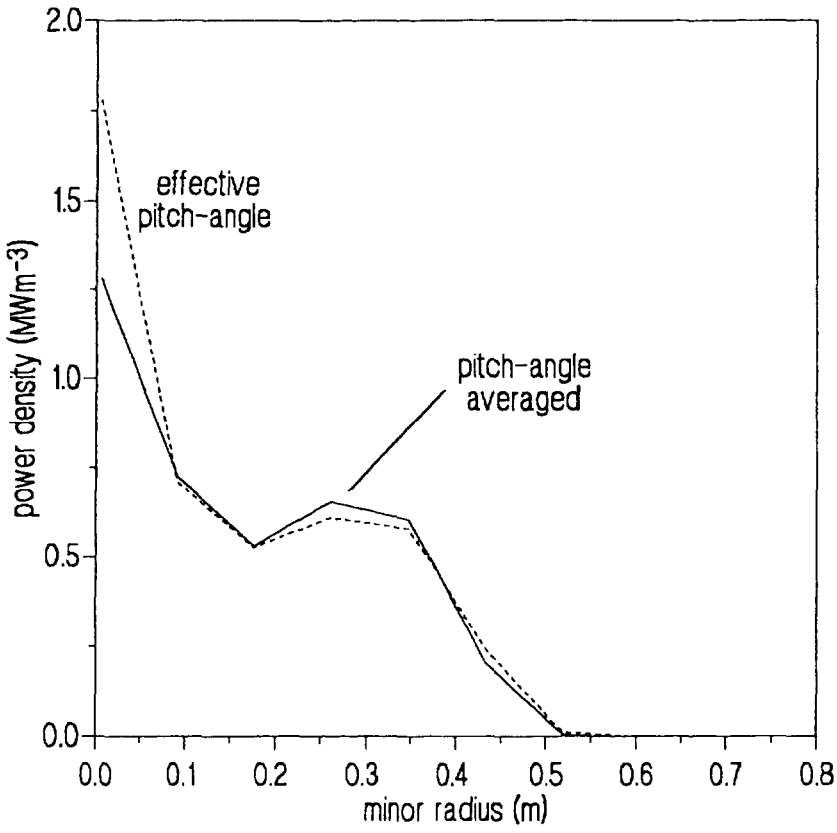

Figure C.1 Electron heating profiles calculated with and without pitch-angle dependence. $P_e(r)$ has been calculated using the isotropic distribution function $f_a(E)$ defined in Chapter 4 (continuous line) and the effective pitch-angle dependent distribution $f_a(E,\mu^2_{eff})$ introduced in Chapter 5 to calculate the fusion yield (dashed curve).

where the reaction rate $<\sigma v>$ reaches its maximum, around 800 keV. As a consequence the calculation of the reactivity and the fusion yield is strongly weighted in that energy range, where pitch-angle scattering cannot yet be considered negligible.

On the contrary the kernel of the integral used to calculate the electron and ion power deposition profiles are functions monotonically increasing with energy (see for example Eqs.(4.30)) and for this reason pitch-angle effects can be safely neglected. Consequently either distribution can be used in the expression of the collision operators with no appreciable differences. To further check this point, a copy of the PHANTOM code has been modified to calculate the electron heating profile using $f_a(E,\mu^2_{eff})$. The result is shown in Fig.C.1, where the new heating profile is compared with that calculated with $f_a(E)$: as it can be seen, there is no significant difference.